Finite Element Analysis on Vibration Behavior and Fatigue Cracking Prediction of a Francis Type Hydraulic Turbine

by

Sze Bun Chan

B.A.Sc (Mechanical Engineering), The University of British Columbia, 1997

A Thesis submitted in partial fulfillment of the requirement for the Degree of Master of Applied Science

in

THE FACULTY OF GRADUATE STUDIES

(Department of Mechanical Engineering)

We accept this thesis as conforming to the required standard

THE UNIVERSITY OF BRITISH COLUMBIA

September 1999

In presenting this thesis in partial fulfilment of the requirements for an advanced degree at the University of British Columbia, I agree that the Library shall make it freely available for reference and study. I further agree that permission for extensive copying of this thesis for scholarly purposes may be granted by the head of my department or by his or her representatives. It is understood that copying or publication of this thesis for financial gain shall not be allowed without my written permission.

Department of *Mechanical Engineering*

The University of British Columbia
Vancouver, Canada

Date *Sept 29, 1999*

Abstract

GMS turbine cracking problem was investigated using finite element analysis. Analysis results confirmed that fatigue cracking could occur due to resonance induced by pressure variation as turbine blades pass wicket gates. Analyses also showed that fatigue life could be extremely low due to extremely high cycles experienced by the turbine.

Installation of blade stiffeners and thickness modifications could change the natural frequency of the turbine. However, the modifications could cause efficiency reduction, cavitation behavior change or structural weakness. Therefore no feasible modifications were suggested.

Table of Content

List of Figures

List of Tables

List of Appendices

1 Technical Background and Research Approach

1.1 Introduction

BC Hydro and Power Authority (BC Hydro) is the major power supplier in the Province of British Columbia, Canada. It has been experiencing a severe fatigue cracking problem with five Francis-type turbine runners. These turbine runners (Units 1 to 5) were installed in Gordon M. Shrum (GMS) Power Generating Station from September 1968 to May 1969 [1]. Mitsubishi Heavy Industries Limited (MHI), Takasago, Japan, manufactured all five of these problem turbines. Five more turbine units were installed from 1971 to 1980. However, no severe cracking problem has occurred in the latter runners.[1]

The fatigue cracks were found on the blades of all five turbines during regular inspections since 1972. Both the MHI and BC Hydro had done extensive inspections and tests on finding the source of the fatigue cracks. However, no conclusive results can be drawn.

It is postulated that the fatigue cracks could be induced by resonance of the turbine under normal operating condition. With sophisticated aids of powerful computers and finite element programs, it is thought possible to answer the above question. It would be the interest of BC Hydro if such research could lead to turbine modifications to eliminate or reduce the occurrence of fatigue cracking on the turbine runners.

---

[1] Tokyo Shibaura Electric (Toshiba) Co., Ltd., Tokyo, Japan, manufactured turbines unit 6-8. Fuji Electric Co. Ltd., Tokyo, Japan, manufactured turbines unit 9-10.

1.2 Technical Background

1.2.1 Technical Data

As mentioned previously, Mitsubishi Heavy Industries Ltd., Japan manufactured the first five turbine runners. They are vertical shaft Francis wheel type runners of diameter of 5.3 m (17.5 ft). Each runner is connected to a generator above by a hollow vertical shaft. The turbine runners drive 235 MW generators at a speed of 150 RPM (2.5 cycles/second). Referring to Figure 1, for general layout of the turbine, each runner was cast as one-piece casting. The base material is ASTM A27 steel, with yield strength of 220 MPa (32 ksi) and ultimate tensile strength of 448 MPa (65 ksi). This material is considered to be similar to ASTM A55 [3] or AISI 1020 low carbon steel.

Each turbine consists of 17 blades. These blades are held between a circular disc on top, known as the crown, and a circular ring at the outer diameter of the turbine, known as the band. The turbine runner is connected to the generator through a vertical shaft connecting to the inner rim of the crown. The turbine runners are powered by head pressure of 165 m (540 ft). Water flows into the turbine compartment through a spiral case. Water is redirected by 24 stay vanes, followed by 24 wicket gates. Water enters the runner through passages between the blades and discharges vertically downward at the center of the runner.

On each blade, stainless steel overlay was welded on the suction side of the blade to prevent cavitation. The turbines were stress-relieved at various stages of manufacture by heating in an oven at an elevated temperature.

2

1.2.2 Crack Locations and Cracking Pattern

Fatigue cracks are mainly located at two locations (Refer to Figure 2): (1) trailing edge of the suction side of the blade where the blade meets the crown, so called location [A]; (2) leading edge of the suction of the blade where the blade meets the band, so called location [C]. In the most severe case, 55 cm (22 inches) through thickness crack was found on the blade at the crown discharge end [7]. In most cases, cracking at location [A] is much more extensive than that at [C]. One turbine runner has had a total of 28 cracks [2]. There has been no specific pattern on cracking, however, some turbines have more serious cracking problem than others do and some blades on some turbines appear to crack more than others on the same turbine.

1.3 Previous Work

1.3.1 Fracture Surface Analysis

In June 1973, BC Hydro had examined some fracture surface samples. It is reported that the trailing edge cracks appeared to originate on the suction side of the blade where the stainless steel overlay terminated and blended into the parent mild steel casting [2]. It was suggested that there might have been some fabrication problems. The report stated that the manufacturer applied the harder stainless steel E301 in the first pass, and high alloy E308 stainless steel in the second pass. Later metallurgical study confirmed that Vickers hardness value of 440 was found in the casting/overlay interface, compared to Vickers value of the parent material at 170 H_v and that of the stainless steel close to the surface at 230 H_v. Refer to Figure 3 for a hardness distribution on the blade. The wrong order of application of stainless steel caused excess dilution and induced a more brittle constitutes at the interface [3].

In July of the same year, MHI analyzed some of the initial crack samples. They found that cracks originated around defects in the transition zone between the factory applied stainless steel overlay and the mild steel parent material. Vickers hardness value in the neighboring material of the crack initiation point was about 500-600 [2]. This hardness value is abnormally high compared to the general maximum value of 400. The manufacturer report confirmed the BC Hydro findings.

The manufacturer suggested 'perfect welding' repairing procedures to remove the heat-induced cracks. It involved removal of crack and partially filling the void first with a mild steel electrode (7018) and then applying a "butter" layer of electrode E309 before the finish electrode E301 [2]. However, the cracking continued to re-occur even after applying the 'perfect welding' procedures. This suggested that the cracking problem is not solely material related in nature and that other factors may be involved.

1.3.2 Residual Stress Measurements

Residual stress measurements were performed on the turbine runner units 2 and 3. Eight measurements were taken on parent mild steel material where no stainless steel overlay was applied (Refer to Figure 2). The residual stress is measured using the center hole technique [4-5]. The highest tensile residual stress value was found to be at the yield point. Cracking blades have higher average residual stress than that of the non-cracking blades. However, some of the non-cracking blades measured residual stress value near the yield point. Moreover, both suction side and pressure side of the blade measured high residual stresses [6]. Table 1 summarizes residual stress values obtained from testing. It is, therefore, non-conclusive that high residual stress alone can initiate and propagate the fatigue cracks.

The existence of brittle layer and high residual stress constitute the possibility of crack initiation. However, high operational stress and vibration sources seem to be also necessary for the observed fatigue crack to propagate. Thus, measurements of operational stresses and natural frequencies were also carried out.

1.3.3 Operational Stress Measurements

In 1973, MHI performed tests to measure the stress on the model runner under similar operational condition [7]. The model was set to rotate at 1062 RPM to simulate power produced at 165 m (540 ft) head pressure. Strain gages were attached to the critical locations of the model runner, including locations [A] and [C]. Using dimensional analysis, the equivalent stress on the actual turbine can be determined (Appendix A discusses the derivation of the dimensional analysis and the related operating parameters are listed under Table 2).

MHI model test showed that the operational stress of the model runner is highest at locations [A] and [C]. The stress levels at [A] and [C] were 9.8 MPa (1.4 ksi) and 66.9 MPa (9.1 ksi), respectively. Stress fluctuation is about 10.3 MPa (1.5 ksi). The measured stresses seemed to be too low to cause the fatigue crack propagation.

It is important to note, however, that the MHI model test found that operational stress at [C] is almost 7 times higher than that at [A]. This result does not agree with, and actually contradicts with the fact that cracking is more severe at [A] than at [C]. Later in this thesis, we will discuss the reason why MHI test was unable to predict highest stress level at [A], and why it cannot detect resonance of the turbine runner.

BC Hydro also performed operational stress measurement using strain gages attached on the runner in 1975. The measurement was taken within 2 hours of start-up

while the turbine wheel was running at maximum loading. Test results reported mean operating stress ranging from 31.7 MPa to 91.6 MPa (4.6 ksi to 13.3 ksi) and fluctuating stress ranging from 2.8 MPa to 10.3 MPa (0.4 ksi to 1.5 ksi) [3]. Comparing BC Hydro and MHI results, it is noted that the fluctuating stress is very close whereas the mean stress found by BC Hydro is significantly higher than that obtained by MHI. Comparison is summarized in Table 3.

1.3.4 Natural Frequency Tests

1.3.4.1 Holographic Test on Turbine Model by UBC

In 1975, the model runner was sent to the University of British Columbia (UBC) for dynamic behavior analysis [9]. The study showed that the ratio of natural frequency of the model runner to that of the full size turbine was about 10.1 [9]. The test found the fundamental frequency of the model runner to be 492 Hz and the last detectable frequency to be 3461 Hz. Therefore, the fundamental frequency of the full size turbine should be about 49.2 Hz. On the other hand, the study indicated that sub-harmonic forcing frequencies could induce super-harmonic responses [9]. This idea will be used later to determine the presumed excitation frequencies in the harmonic response analysis of finite element method.

The first six resonant frequencies were recorded by laser holographic interferometry. However, the holographs can only identify band dominant mode shapes. It is very difficult to identify other types of vibrating modes by holographs. For reference, the first six natural frequencies are listed in Table 4(a). The natural frequency shift of the submerged turbine model ranged from 16.4% to 36.2%. The result is also listed in Table 4(b).

1.3.4.2 Actual Turbine Test and Effect of Stress Stiffeners

BC Hydro continued the natural frequency testing on the full size turbine runner. Also, BC Hydro started investigating the effect of installing blade stiffeners on the runner. The blade stiffeners are steel rods of 2.22 cm (7/8 inch) in diameter, 20.3 cm (8 inches) in length. Two stiffeners were installed near the trailing edges of each pair of blades. They were located at 40% and 70% of edge length measuring from the crown. Each stiffener was on one end connected to the trailing edge and on the other end connected to the suction side of the blade. The schematic diagram shown in Figure 49 best represents the arrangement.

The changes in natural frequencies were measured and results are listed in Table 5. The table shows natural frequencies recorded from the blade and from the band, respectively. The discrepancy between the blade and band results might be originated from the curve-fitting computation carried out by the measuring instrument. These numbers were compared with FE results obtained in later sections. Installing stress stiffeners appear to increase the natural frequencies of the turbine from 12.1 to 18.1%. Detailed discussion of the effect of the stiffeners will be given in the section 3.5.1, Turbine Modifications: Installation of Blade Stiffeners.

1.3.5 Dynamic Response Test on Turbine Model by BC Hydro

In early 1999, BC Hydro had conducted harmonic response test on the turbine model. The model was mounted vertically on a steel frame and the experiment was carried out by using an exciter or by hammering. The response of the turbine was measured by two accelerometers mounted at different positions of the turbine. The

spectrum diagram of the turbine was also plotted and is shown in Figure 5. It shows very high response at 1085 Hz and 1789 Hz.

The effect of water damping on natural frequencies was studied by gradually immersing the turbine model into water. The turbine model and the mounting frame were placed in a water tank. Water was filled in the tank stepwise until water fully covered the turbine model. Between each step, spectrum of the turbine was recorded. A spectral map was afterwards created. Figure 6 shows a spectral map of blade 14 that was excited by a vertical random force. The response in the map was taken at the blade close to the band. The bottom of the map shows the spectrum curve with 0% water covering the model, and the top shows the response with 100% water covering the model.

The map shows that lower natural frequencies are relatively unaffected by the water damping, but some experienced higher shift. This means that damping effect is mode dependent. Moreover, higher frequencies tended to shift more and might merge to together. It is also worthwhile to note that some frequencies had very high response as water was covering the model half way. This test provides significant information on the effect of water damping mass at different frequencies.

1.4 Research Approach

1.4.1 Preliminary Plan

Previous work did not reveal high stress fluctuations that may initiate or propagate fatigue cracks on the problem turbines. Due to limitation of numbers of data points taken and duration of experiment, it is very difficult to study the complete vibration behavior of the turbine using the research methods mentioned above. It is therefore proposed to use the finite element method (FEM) for this project to obtain stress-strain data, natural

frequencies, mode shapes, harmonic responses and stress intensity factors (SIF) of the turbine. Moreover, the overall vibration behavior of the component may also be simulated.

In the GMS turbine-cracking problem, the source of stress fluctuation is not known. No particular excitation frequency could be isolated. Considering the fact that overall stress level of the turbine was low and crack propagation rate was high, it was reasonable to suspect that resonance caused high local stress fluctuation and fatigued the turbine blades. Yet, evidences had to be found to support this theory.

In order to evaluate the above hypothesis, the harmonic response of the turbine under certain excitation frequencies has to be found. Since excitation frequencies are not known, a wise guess of the excitation frequencies would be necessary. The correct excitation frequency should reproduce experimental findings typically in the highest stress areas. Two main conditions are the basic criteria for determining the 'correct' excitation frequency; these are: highest stress was located on suction side of the blade and stress level at location [A] was higher than that at location [C]. This analysis will be preceded by calculating the turbine natural frequencies. This should provide a good starting point since it also facilitates checking the FE model against available experimental data.

If resonances were found to be the source of stress fluctuation that led to fatigue, it would be of our interest to compare the FEM predicted crack propagation rate with actual propagation rate. Finally, some turbine modifications should be suggested to reduce or eliminate further fatigue cracking.

1.4.2 Finite Element Method and Computational Tools

Finite element method (FEM) starts with building a finite element (FE) model in the computer. In sophisticated finite element program, FE model can be built using a graphical interface, known as pre-processing program. Boundary conditions and method of analysis can be chosen and applied through this interface. High intensity computation is then performed in the processing program using the data input from the pre-processing phase. Finally, computational results are reviewed by post-processing program.

In this work, a commercially available finite element program, known as ANSYS, is used to produce all finite element results. It provides a single integrated package of pre-processing, processing, and post-processing programs. The program is run using a personal computer (PC) of Pentium II 233 MHz with 192 MB RAM. Also, a spreadsheet was used to produce fatigue crack propagation life prediction. And MathCAD was used to compute fatigue initiation life.

2 Modeling Analysis of Turbine

2.1 Finite Element Model of Turbine

The FE model is built to simulate the geometry and physical properties of the structure or the component. Computational intensity and hardware requirement would increase as a function of the total number of degree of freedom (DOF) in the model. Which is, in turn, function of the number of nodes in the model. Each node may have 6 DOF that typically include translational motion and rotational motion in 3 axes.

Geometrical and material properties of the structure are usually assigned on the element level. In this work, shell and solid elements are used to model the turbine. 4-node elastic shell elements are used in static analysis, modal analysis and harmonic response analysis whereas 20-node 3D solid elements and 8-node plastic shell elements are used in the sub-modeling of the cracking area to calculate stress intensity factor (SIF). The properties of these are summarized in Appendix D.

The basic assumption made in building the finite element model includes: (1) average contour scan of the model runner correctly represents the contour of the full size runner, (2) every blade has the same contour and (3) the crown, blades and band are thin such that they may be modeled using shell element.

The GMS turbine FE model is built based on the blade contour of the manufacturer's turbine model. The 1:14 turbine model was sent to GE Hydro, Ontario, for a contour scan. A total of five (5) blades were scanned. [2] The average of these five scans was used in the FE modeling. Contours of both pressure and suction side of the blade were obtained [10]. Contour measurements were stored in Cartesian coordinate. On each

---

[2] GE Hydro contour scan obtained pressure and suction side contour of blade 5, 6, 7, 11, and 14.

surface scan, the blade was divided from the crown to the band into 16 sections. First section was located at the crown-blade intersection, whereas the sixteenth section was located at band-blade intersection. In each section, 42 data points were obtained. The first point was at the leading edge, whereas the 42nd point was at the trailing edge of the blade. This would create 16 by 42 grids on both sides of the blade. The data points were denser near the leading edge and trailing edge. Figure 4 shows the arrangement of the scanned data points. In order to obtain a reasonable aspect ratio for the elements, only 300 points were taken on each side, i.e., 15 by 20 grids were used instead.

Since the turbine blades were relatively thin compared to the blade width, shell element is appropriate to use. The data points were first scaled to the actual turbine size. Mid points of the corresponding grids on the pressure and suction side were used as corner nodes of the shell elements. The distance between the corresponding grids was taken as corner thickness. The blade elements were generated using a simple program written by the author. The program created all 'real constant' for the blade elements, which stored the corner thickness of each element on the blade. [3] Also this program created data for quadrilateral shell elements for one single blade as shown in Figure 7.

The crown and the band of the turbine were generated using section 1 and section 16's data points, respectively. The data points were joined to create the outline of the crown and the band. The lines were then rotated one seventeenth (1/17) of a circle about the center axis of the runner to obtain meshable areas for the crown and the band. Using the auto-mesh option of ANSYS, the elements of the crown and the band were automatically generated. Since the crown does not end at the trailing edge, an extended

---

[3] Read constant is the terminology used by ANSYS. It contains thickness data for shell element. For other type elements, the real constant contains information, such as moment of inertia about different axes.

crown area was created. The extended area started from the trailing edge of the blade and extended horizontally and radially inward by 48 cm (18.9 in), where the runner joins the shaft. Figure 8 shows the crown mesh, and Figure 9 shows the band mesh.

The above procedure produced one seventeenth of a turbine runner. By copying the above elements 17 times about the center axis of the turbine, the whole runner was then generated. Nodes at identical coordinates were then merged to join different parts of the turbine runner together. The full turbine model consists of 14008 shell elements, 13591 nodes and 80934 degrees of freedom.

2.2 Modal Analysis

2.2.1 Introduction and Basic Equations

Modal analysis is to determine the natural frequencies and mode shapes of a structure. By determining the natural frequencies and mode shapes of the turbine runner, it should give insight to estimate the possible sources of excitation. Modal analysis also provides basis of verifying the accuracy of the FE model by comparing the results to experimental findings. The performed analysis is a linear one assuming constant stiffness and mass effects. Fully fixed displacement boundary condition was applied to the inner rim of the extended crown to simulate the rigid connection to the shaft as shown in Figure 10 and Figure 11. The basic theory and underlying equations of modal analysis is discussed in Appendix B.

2.2.2 Rotation Related Effects on Natural Frequency

Modeling technique in modal analysis assumes that the turbine is stationary in space. No rotation effect was taken into account. In practice, three (3) types of rotation related

13

effects could alter natural frequencies of the runner. In the following, we briefly discuss these factors.

2.2.2.1 Natural Frequency Split

The natural frequency of a stationary model would split into two natural frequencies as the rotational speed of the turbine increases. Typically, this effect could be visualized on the Campbell diagram[4]. The increased natural frequency is called the forward precession and the decreased one is called the backward precession [13]. The rate of change in natural frequency may vary, however, and it is also mode dependent.

To estimate the effect on natural frequency, it was assumed that the change in natural frequency is equal to rotational speed of the turbine. Since the turbine is running at fixed speed of 150 RPM (2.5 cycles/second), we may assume that natural frequency splits into plus or minus 2.5 Hz in actual operation.

2.2.2.2 Spin Softening

The vibration of a rotating body could cause relative circumferential and radial motion. The motion could change the direction of the centrifugal load and therefore may destabilize the structure. Since modal analysis cannot directly account for changes in geometry, the effect could be accounted for by adjustment of the stiffness matrix. This effect is called spin softening [14].

To explain the effect, consider a simple spring-mass system as shown Figure 12. The equilibrium of the spring and centrifugal forces on the mass using small deflection assumption requires:

---

[4] The Campbell diagram plots natural frequency against rotational speed.

$$[K]\{u\} = \omega_s^2[M]\{r\} \qquad (1)$$

where $\quad u = radial\ displacement\ of\ the\ mass\ from\ the\ static\ position$

$\qquad\quad r = radial\ rest\ position\ of\ the\ mass\ with\ respect\ to\ the\ axis\ of\ rotation$

$\qquad\quad \omega_s = angular\ velocity\ of\ rotation$

For large deflection, the following equation may be written:

$$[K]\{u\} = \omega_s^2[M]\{r + u\} \qquad (2)$$

By rearrangement

$$\left([K] - \omega_s^2[M]\right)\{u\} = \omega_s^2[M]\{r\} \qquad (3)$$

Defining:

$$[\overline{K}] = [K] - \omega_s^2[M] \qquad (4)$$

and

$$\{\overline{F}\} = \omega_s^2[M]\{r\} \qquad (5)$$

Equation (3) becomes

$$[\overline{K}]\{u\} = \{\overline{F}\} \qquad (6)$$

Equation (6) shows that small deflection solution may be used for large deflection analysis by proper adjustment of the stiffness matrix and the forcing vector. The eigenvalue equation becomes

$$\left|[\overline{K}] - \omega_s^2[\overline{M}]\right| = 0 \qquad (7)$$

or

15

$$\left| \left([K] - \omega_s^2 [M] \right) - \omega^2 [M] \right| = 0 \tag{8}$$

where ω = *the natural frequencies of the rotating body*

Spin softening is applied to the modal analysis using pre-stressed option in ANSYS. The centrifugal effect on the structure was first determined using static pre-stressed analysis. And the required data are then fed into the modal analysis procedure.

2.2.3 Stress Stiffening

Stress state of a component could stiffen or weaken the structure. This is known as the stress stiffening effect. The effect normally needs to be considered for thin structure with very small bending stiffness. The effect is accounted for by generating an additional stiffness matrix. The matrix could be first produced via static analysis and then incorporated into modal analysis. The stress stiffening effect is incorporated by adding the following matrix to the element stiffness matrix [15].

$$[S_i] = \int [G_i]^T [\tau_i][G_i] dV \tag{9}$$

where $[G_i]$ *is the matrix of shape function derivatives*

   $[\tau_i]$ *is a matrix of the current Cauchy stresses in the element*

Applying the stress-stiffening matrix to the eigenvalue equation (8), the new modified equation is:

$$\left| \left([K] + [S] - \omega_s^2 [M] \right) - \omega^2 [M] \right| = 0 \tag{10}$$

where $[S]$ *is the stress-stiffening matrix*

Equation (10) is solved to obtain natural frequencies and mode shapes of a structure including both stress stiffening and spin softening effect.

2.3 Damping using Added Mass Effect

Dynamic response of submerged structures requires knowledge of effect of the fluid on the structure. In general, the interaction is a complex coupled problem. In the simplest representation, the effect of the fluid on the structure is proportional to only the interface accelerations. It can be included as an added mass component in the dynamic equilibrium equations of the structure. The added mass concept is equivalent to an integral of the total kinetic energy, which the body motion imparts to the surrounding fluid in a potential flow solution [16].

Surface panel singularity distribution method originally presented by Hess and Smith [17] formulates the interaction of fluid and structure in terms of boundary integral. The potential in the fluid is represented using the singularity distributions on the body surface. Different assumptions about the fluid potential inside the body lead to different formulations of the singularity based methods, namely source formulation and dipole formulation methods. Further discussion was given by Vorus and Hylarides [18-19]. Similar equation was given by Rajasankar et al, [20] for ship hull problem and similar analysis was also applied to turboprop by NASA [21].

Empirical evaluation of added mass effect on plate is also available [22]. However, the method was considered to be not suitable to apply to turbine blades.

To briefly explain the theory of the added mass effect, we started by the FE structural equilibrium equations in the form:

$$[M]\{\ddot{u}\} + [C]\{\dot{u}\} + [K]\{u\} = \{F_f(t) + F_s(t)\} \tag{11}$$

where $[M] = structural\ mass\ matrix$

$[C] = damping\ matrix$

[K] = *structural stiffness matrix*

F_f = *fluid force vector*

F_s = *structural and body force vector*

The added mass matrix in the case of source formulation is given in Appendix C.

$$[M_A] = [T]^T [A][H][L]^{-1}[T] \tag{12}$$

where   [T] = *transformation matrix for normal to global directions*

      [H] = *coefficient matrix relating source strength to velocity potential*

      [M_A] = added fluid mass matrix

      [A] = diagonal matrix of panel areas

      [L] = *coefficient matrix relating source strength to normal velocity at*

        panel control points

For dipole formulation:

$$[M_A] = -[T]^T [A][L]^{-1}[H][T] \tag{13}$$

Equations (12) and (13) are considered to be equivalent. Experiments found that the dipole formulation provided, however, better predictions to the response.

The combined structural equation becomes:

$$[M + M_A]\{\ddot{u}\} + [C]\{\dot{u}\} + [K]\{u\} = \{F_s(t)\} \tag{14}$$

where $\{\ddot{u}\}$ = *nodal acceleration vector*

      $\{\dot{u}\}$ = *nodal velocity vector*

      $\{u\}$ = *nodal displacement vector*

      $\{F_f\}$ = *fluid force vector*

      $\{F_s\}$ = *structural and body force vector*

Although equation (12) or (13) could be evaluated and applied to finite element method, it is very difficult to obtain coefficient matrices [H] and [L]. Therefore, this method is not applied to the finite element model. Since it is known that water damping could reduce natural frequencies anywhere from 16 to 36% [9], the damping effect could still be included by shifting natural frequencies down in 16 to 36% range. The detailed discussion on damping would be included in section 3.2.5

2.4 Estimation of Excitation Frequencies

Resonance would be caused by excitation frequencies that are close to natural frequencies of the turbine. In determining the possible excitation frequencies, it was assumed that the excitation is originated from: (1) rotational speed related source and (2) vortex shedding related source.

2.4.1 Rotational Speed Related Excitation

Rotation related source is the most common type of excitation sources. Since there are 24 wicket gates surrounding the turbine runner and the runner has 17 blades, the excitation frequencies could be the product of the rotational speed and the numbers of gates or blades. As stated in reference [9], the sub-harmonics may excite super-harmonics, the multiples of the product of the rotation speed and the gate or blade numbers could be possible excitation frequencies.

The turbine runner is rotating with 150 RPM, (2.5 cycles/second). Computing the multiples of the product of rotational speed and number of blades or wicket gates, the list of possible excitation frequencies up to 180 Hz is given in Table 6. The excitation frequency would be used in the harmonic response analysis. The 'correct' excitation frequency should produce agreeable results with experimental findings.

19

2.4.2 Vortex Shedding as Excitation

Vortex shedding could also be another source of excitation. The phenomenon is observed as the fluid flows over a bluff object and separation begins. The vorticity in the boundary layers causes them to roll into vortex spirals at regular time intervals. This was found to be the cause of blade and stay vane vibration problems on other turbines worldwide [23-26]. The excitation frequency may be obtained by the following equation:

$$f = S\frac{V}{d} \tag{15}$$

where $f = frequency\ of\ vortex$

$S = Strouhal\ number,\ experimentally\ determined$

$V = velocity\ of\ approach$

$d = largest\ projected\ cross-section\ dimension\ on\ approach\ flow$ [23]

It is difficult to determine excitation frequencies using equation (15) for several reasons. The first, there is no definite range for Strouhal number. Experimental data for this number is not available for these turbine blades. The second reason is that it is very difficult to define the velocity of approach because velocity on the blade changes from inlet to outlet and from top to bottom. This change is also evident for the largest projected cross-section of the blade. Without proper excitation amplitude and direction, harmonic response analysis cannot be performed. Therefore, this source of excitation was ignored due to lack of information.

2.5 Harmonic Response Analysis

Harmonic response (HR) analysis produces cyclic response in a structure under sustained cyclic loading. The technique is to determine the steady-state response of a linear structure to sinusoidal loads. It assumes constant stiffness, damping and mass

effects. Therefore, no nonlinearities and transient effect may be included. The basic theory is described as below:

2.5.1 Theory of Harmonic Response Analysis

The general force equation of motion for a structural system is:

$$[M]\{\ddot{u}\} + [C]\{\dot{u}\} + [K]\{u\} = \{F^a\}$$

(16)

where $[M] = structural\ mass\ matrix$

$[C] = structural\ damping\ matrix$

$[K] = structural\ stiffness\ matrix$

$\{\ddot{u}\} = nodal\ acceleration\ vector$

$\{\dot{u}\} = nodal\ velocity\ vector$

$\{u\} = nodal\ displacement\ vector$

$\{F^a\} = applied\ load\ vector$

By applying sinusoidal loads, the applied load vector could be expressed as:

$$\{F^a\} = \{F_c\} = \{F_{max}e^{i\Psi}\}e^{i\Omega t} = (\{F_1\} + i\{F_2\})e^{i\Omega t}$$

(17)

where $\{F_c\} = complex\ load\ vector$

$\Omega = excitation\ frequency\ (radian/second)$

$\Psi = force\ phase\ shift\ (radian)$

$\{F_1\} = real\ component\ of\ applied\ load\ vector$

$\{F_2\} = imaginary\ component\ of\ applied\ load\ vector$

The general solution of the displacement can be expressed similarly:

$$\{u_c\} = \{u_{max}e^{i\Phi}\}e^{i\Omega t} = (\{u_1\} + i\{u_2\})e^{i\Omega t}$$

(18)

21

where $\{u_c\}$ = *complex displacement vector*

Φ = *displacement phase shift (radian)*

$\{u_1\}$ = *real component of displacement vector*

$\{u_2\}$ = *imaginary component of displacement vector*

By substituting equation (18) into equation (16), we have:

$$(-\Omega^2[M] + i\Omega[C] + [K])\{u_c\} = (F_c) \tag{19}$$

Defining a matrix $[K_c]$ as:

$$[K_c] = (-\Omega^2[M] + i\Omega[C] + [K]) \tag{20}$$

The solution for u_c may be obtained by solving:

$$[K_c]\{u_c\} = \{F_c\} \tag{21}$$

Solving equation (21) is known as "Full Solution Method". This method uses the same wavefront solver as for static analysis. However, complex arithmetic is used in the computation. ANSYS also provides a "Reduced Solution Method". Similar to the reduced solution method in modal analysis, the solution is solved using reduced structural matrices. Since the full solution method solves the turbine model in reasonable time (about 1.5 hours) the reduced solution method is not used.

2.5.2 Boundary Conditions for Harmonic Response Analysis

Excitation frequencies listed in Table 6 are related to numbers of wicket gates or blades. Therefore the actual source of excitation was assumed to relate to water pressure variation. CFD model was developed to find the steady state pressure of the turbine [27]. The model used an explicit, time marching Finite Volume scheme and the equations of continuity and momentum were solved directly using the time marching scheme. The

CFD method solved steady state pressure on one passage section between two blades. Wicket gates and other details of the turbines were omitted. The computation assumes the turbine running at full power.

Preliminary harmonic response analysis was to determine which excitation frequency could match the two criteria stated in Section 1.4.1. Therefore, the sinusoidal loading was taken to be 100% of the steady pressure found by CFD method. The results at different possible frequencies were compared to the criteria to isolate the 'correct' excitation frequency. For control purpose, a simple static analysis should be performed using the same boundary condition. If the turbine is suffering from resonance, the stress results on harmonic response analysis should be significantly higher than those obtained from the static analysis.

2.5.3 Displacement Superposition of Static and Harmonic Response Results

In practice, the actual sinusoidal loading would only be a few percent of the steady state pressure. In this work, we, therefore propose to determine the actual stress field of the turbine using the principle of superposition on displacement results.

Assuming the pressure variation of the turbine is about 5% of the steady state pressure. Thus, 95% of the steady state pressure would be applied as static loading on the turbine. Suppose the displacement results are obtained from linear analysis. It follows that the displacements from the 5% harmonic response analysis can be added to that of the 95% static analysis as shown in Figure 13 (This loading case would be referred to as 5%HR loading). The sum of the displacements should be a more realistic estimate of the turbine response at maximum loading. Stress field of the turbine under this composition

23

of loading was then determined by performing a materially nonlinear static analysis using the new displacement results.

By subtracting the harmonic response displacement from the static displacement, the minimum loading situation of the turbine could be found. For comparison purposes the same procedures were carried out at 2.5% harmonic response and 97.5% static analyses (i.e., 2.5%HR loading.). The resultant displacements were used in the fatigue life prediction.

2.6 *Stress Intensity Factor (SIF)*

2.6.1 Introduction

In terms of crack propagation prediction, the direction and the propagation rate have to be found. Since the turbine was subjected to variable loading, the crack propagation direction was yet to be determined. An approach suggested by Sih et al relates the crack propagation direction to minimum strain energy density [28 - 29]. Other researchers suggested maximum strain energy release rate method [30] and the maximum tensile stress theory [31].

Most of these methods have not yet been implemented in commercial finite element program. More importantly, including crack propagation directions requires redefining the geometry with the new crack direction and size and re-meshing the structure at each crack increment. Such analysis may be best solved using a new technique, known as the Arbitrary Lagrangian Eulerian (ALE) finite element method [32]. However, ALE finite element formulation has not been implemented yet in commercial FE codes and it is beyond the scope of this project to investigate this area. In this analysis, and from the knowledge of experimental data, the crack propagation direction at location [A] is

24

presumed to be parallel to the crown. By creating a fine meshed zone in the preset location, re-meshing could be greatly simplified.

After completing the harmonic response analysis, one should be able to predict the fatigue life of the turbine blade. Paris Law requires obtaining stress intensity factor range (SIF range) in order to predict propagation life. In ANSYS, SIF at a crack tip could be determined using linear static analysis. Mode I, II and III stress intensity factors can be calculated using analysis post-processing program.

2.6.2 Theory of Stress Intensity Factor Determination

Assuming Linear Elastic Fracture Mechanics (LEFM) and defining a Cartesian coordinate at the crack tip as shown in Figure 14, the actual displacement around the crack-tip expressed by [33].

The displacement, u, in x direction, parallel to crack extension direction:

$$u = \frac{K_I}{4G}\sqrt{\frac{r}{2\pi}}\left[(2\kappa-1)\cos\frac{\theta}{2}-\cos\frac{3\theta}{2}\right]-\frac{K_{II}}{4G}\sqrt{\frac{r}{2\pi}}\left[(2\kappa+3)\sin\frac{\theta}{2}+\sin\frac{3\theta}{2}\right] \quad (22)$$

The displacement, v, in y direction, perpendicular to crack extension and crack front:

$$v = \frac{K_I}{4G}\sqrt{\frac{r}{2\pi}}\left[(2\kappa-1)\sin\frac{\theta}{2}-\sin\frac{3\theta}{2}\right]-\frac{K_{II}}{4G}\sqrt{\frac{r}{2\pi}}\left[(2\kappa+3)\cos\frac{\theta}{2}+\cos\frac{3\theta}{2}\right] \quad (23)$$

The displacement, w, in z direction, tangent to the crack front:

$$w = \frac{2K_{III}}{G}\sqrt{\frac{r}{2\pi}}\sin\frac{\theta}{2} \quad (24)$$

where

u, v, w = displacement in a local Cartesian coordinate system as shown in

Figure 14.

25

r, θ = coordinates in a local cylindrical coordinate system as shown in

  Figure 14

G = shear modulus

K_I, K_{II}, K_{III} = stress intensity factors relating to fracture mode I, II and III

  respectively.

$$\kappa = \begin{cases} 3 - 4v & \text{in plane strain or axisymmetric} \\ \dfrac{3 - v}{1 + v} & \text{in plane stress} \end{cases}$$

v = Poisson's ratio

By evaluating equation (22) – (24) at $\theta = 180^\circ$:

$$u = \frac{K_{II}}{2G} \sqrt{\frac{r}{2\pi}} (1 + \kappa) \tag{25}$$

$$v = \frac{K_{I}}{2G} \sqrt{\frac{r}{2\pi}} (1 + \kappa) \tag{26}$$

$$w = \frac{2K_{III}}{G} \sqrt{\frac{r}{2\pi}} \tag{27}$$

In case of an edge crack model, the stress intensity factors are expressed as:

$$K_{I} = \sqrt{2\pi} \frac{G}{1 + \kappa} \frac{|\Delta v|}{\sqrt{r}} \tag{28}$$

$$K_{II} = \sqrt{2\pi} \frac{G}{1 + \kappa} \frac{|\Delta u|}{\sqrt{r}} \tag{29}$$

26

$$K_{III} = \sqrt{2\pi} \frac{G}{1+\kappa} \frac{|\Delta w|}{\sqrt{r}}$$

<div align="right">(30)</div>

where Δu, Δv, and Δw *are the motion of one crack face with respect to the other*

Therefore the SIF range at a crack tip can be evaluated by calculating the difference of stress intensity factors found from applying the maximum and minimum loading to a cracked model. The SIF ranges were then applied to the crack propagation equation to obtain predicted propagation life.

2.6.3 Modeling and Boundary Conditions

In order to obtain more accurate results, solid sub-models were used for this analysis. The submodel was built to simulate the crown-trailing-edge corner, labeled as the high stress location [A]. Due to cyclic symmetry of the turbine deformation, one seventeenth of the turbine would be sufficient to represent the turbine behavior. The solid submodel consisted of part of the crown and the blade, and formed a shape of a small T as shown in Figure 15. A very fine meshed band was introduced to the model to facilitate easy crack extension. (Refer to Figure 16).

In order to transfer displacement boundary conditions from the shell elements to the fine meshed solid elements, shell elements were added to the model. The shell elements extended the T-shaped both on the crown and on the blade as shown in Figure 18 and Figure 19. The boundary conditions were transferred to the solid by the interface shell elements on the solid element faces at the shell-solid transition area [34]. At the overlapping areas, the shell elements were set to 2.54mm (0.1 inch) in thickness to minimize the overlapping stiffening effects. The displacement boundary conditions found

from the previous shell element analysis were applied only to the interfacing shell elements.

An edge crack was put in the solid sub-model, one element below the fillet of the blade. The crack direction was pre-determined to be parallel to the crown. This crack was incrementally extended from 2.5 mm (0.098 inch) to 154.7 mm (6.09 inches). In each increment, the crack was extended by one element length 6.44 mm. The extension took a total of 25 steps.

The crack tip was formed by 8-quarter-point, second order wedge elements. This element simulates the singularity of the stress field at the crack tip (Refer to Figure 17). By assuming extended crack would not change the applied boundary conditions, displacements at maximum and minimum loading were applied to the sub-model as the crack extends. The difference of the SIFs from the maximum and minimum loading was the SIF range. The analysis was performed on both sets of loading cases.

2.7 Fatigue Initiation and Propagation Life Prediction

Fatigue process may be divided into two stages crack initiation (crack nucleation), and crack propagation [35]. Fatigue life is usually regarded as the number of cycles a component could last from initiation to propagation stage. However, there has been no general rule defining the transition of crack initiation to propagation. To determine crack initiation and propagation life, three conditions have to be available: (1) a clear definition of transition from crack initiation to propagation, (2) corresponding prediction equation with necessary experimental constants, and (3) detailed stress picture around the crack area.

2.7.1 Definition of Crack Initiation

Crack initiation generally refers to formation of microcracks close to the surface of the component or the formation of a small crack with some pre-defined length. The nucleation site of the microcracks may be located at (1) slip band (2) grain boundaries, or (3) surface inclusion. The microcracks may be formed by slip plane motion, plastic flow of material matrix or debonding at material matrix or inclusion [36-38]. Since there are too many different controlling factors to crack initiation, it is very difficult to conclude with a comprehensive microscopic theory to define the transition and usually a macroscopic approach is used.

Miller et al defined the transition of crack growth rate by the initiation of a crack with length of 0.7 to 0.9 mm [39]. (Refer to Figure 20) Kitagawa defined the crack length at which the experimental data deviates from LEFM predicted stress level as initiation crack length [40]. (Refer to Figure 21) This initiation crack length is about 0.1 to 0.5 mm. Kujawski and Ellyin defined the transition between the initiation and propagation stages to be at a critical microcrack size or reduction of material's fatigue limit [41-42]. However, no typical initiation crack length was given.

The above definitions do not provide a specific initiation equation, and it was not feasible to model a crack of 0.1 to 0.9 mm in a turbine of diameter 5.3 m. Thus a more appropriate definition was used in the analysis.

Socie and Artwohl [43] argued that initiation life should be calculated from strain cycle fatigue specimen. The corresponding range of crack length is approximately 2.5 mm. Although this definition would include some propagation life, it clearly distinguishes initiation and propagation. Therefore, initiation life corresponding to a crack length of up to 2.5 mm may be determined by strain cycle fatigue equation and

propagation life corresponding to a growth of crack length from 2.5 mm can be determined by Paris Law.

The Morrow's strain cycle fatigue equation [36] is an empirical formula and may be expressed as [44]:

$$\frac{\Delta\varepsilon_t}{2} = \frac{\Delta\varepsilon_E}{2} + \frac{\Delta\varepsilon_P}{2} = \frac{\sigma_f{'}}{E}(2N_f)^b + \varepsilon_f{'}(2N_f)^c \tag{31}$$

Where $\Delta\varepsilon_t$ = total strain range

$\Delta\varepsilon_E$ = elastic strain range

$\Delta\varepsilon_P$ = plastic strain range

$\sigma_f{'}$ = fatigue strength coefficient

$\varepsilon_f{'}$ = fatigue ductility coefficient

b = fatigue strength exponent

c = fatigue ductility exponent

E = elastic modulus

N_f = fatigue initiation life

Fatigue initiation life could be obtained, therefore, if the strain distribution at the critical area is known and the fatigue coefficients are given. Since the equation requires both components of plastic and elastic strains, nonlinear static analysis should be performed to obtain the strain distribution. The equivalent strain from the finite element analysis was used as the total strain:

$$\varepsilon_{eq} = \frac{1}{\sqrt{2}(1+\nu)}\left[\left(\varepsilon_x - \varepsilon_y\right)^2 + \left(\varepsilon_y - \varepsilon_z\right)^2 + \left(\varepsilon_z - \varepsilon_x\right)^2 + \frac{3}{2}\left(\gamma_{xy}^2 + \gamma_{yz}^2 + \gamma_{zx}^2\right)\right]^{1/2} \tag{32}$$

Modifications for the mean stress and stress ratio effect were suggested by various a number of researchers. But they have not been found to give significant changes to initiation life [45] and therefore they were not considered in this analysis

2.7.2 Fatigue Propagation Life Prediction

Fatigue propagation life prediction using Paris power law is also empirical in nature. The Paris equation stated that is given by [46]:

$$\frac{da}{dN} = C(\Delta K)^m \tag{33}$$

where a = crack length

N = number of cycles

$\Delta K = K_{max} - K_{min}$ = stress intensity factor range

C, m = material constants

Experiments by Verreman and Espinosa [47] modified the above equation for low carbon mild steel, in the form:

$$\frac{da}{dN} = 6.49 \times 10^{-9} (\Delta K_{eff})^{3.20} \, mm/cycle \tag{34}$$

where ΔK_{eff} = effective stress intensity factor range $(MPa\sqrt{m})$

The effective stress intensity factor range can be expressed as [48-49]:

$$\Delta K_{eff} = U \cdot \Delta K \tag{35}$$

$$U = \frac{S_{max} - S_{open}}{S_{max} - S_{min}} \tag{36}$$

where S_{max} = maximum stress

S_{open} = crack opening stress

S_{min} = minimum stress

31

The factor U in the above equation modifies the stress intensity range to account for crack closure effect. Since no information is available for the crack closure, the factor U was assumed to be unity for the propagation life prediction in this project.

Forman [50] proposed a modified propagation life equation based on Paris Law. The modified equation also takes into account the stress ratio and the instability of the crack growth as the maximum SIF approaches the fracture toughness. Including modification for plastic zone by Willenborg et al [51-52], the modified Forman's equation states:

$$\frac{da}{dN} = \frac{C'(\Delta K_{eff})^n}{(1 - R_{eff})K_c - \Delta K_{eff}} \tag{37}$$

where C', n are material constants (different from Paris Law)

K_c = critical stress intensity factor for fracture

R_{eff} = effective stress ratio

Effective stress ratio is defined as:

$$R_{eff} = \frac{K_{min} - K_{reduced}}{K_{max} - K_{reduced}} \tag{38}$$

$$K_{reduced} = K_{required} - K_{max} \tag{39}$$

where $K_{required}$ = stress intensity factor required to extend the boundary of plastic zone.

It is believed that Forman's equation may provide a more accurate prediction for propagation life. Unfortunately, it was not possible to obtain the material constants needed for the analysis and, therefore, Paris Law was used in this work.

It should be noted that residual stress may change the crack opening stress and stress ratio [53-58] but it is necessary to use Forman's equation to account for these effects.

32

It should be also noted that equation (34) only accounts for mode I cracking. In the analysis for the turbine blades, it was found that mode II and mode III stress intensity factor ranges were relatively small compared to that of mode I and therefore application of equation (34) was justified. Using equation (34) to calculate propagation life requires SIF range that may be calculated from equation (28) - (30).

3 Design Modifications and Analysis Results

3.1 Overview of Design Modifications

Assuming that resonance is the cause of fatigue cracking, modifications should be focused on changing the excitation frequencies or changing natural frequencies of the turbine runner. Due to the fact that head pressure, rotational speed were preset in the generating station design, it is not possible to alter these factors to reduce resonance. The only choice is to alter the natural frequencies of the runner. The modifications of turbine runner can be divided into two main categories: (1) installation of blade stiffeners, (2) modifications of turbine contour and shape. It is noteworthy that any modification of the turbine could affect cavitation behavior and efficiency. Also, these changes may cause resonance on another mode shape. Therefore, careful analysis and study is needed to finalize a modification. To verify the effectiveness of a modification, modal and harmonic response analyses will be performed to assess the changes.

Installing blade stiffeners to the turbine is a simple and inexpensive external modification to the turbine structure. Since stiffeners do not alter the main contour of the turbine blades, it is easier to avoid changes on cavitation behavior and turbine efficiency. However, depending on the position and size of the stiffeners, they can be blocking blade passages and changing water flow pattern. On the other hand, method of installation is of major concern. Since welded-on stiffeners could induce high residual stress, cracks could be initialized from the heat-affected zone. A number of different arrangements have been proposed and simulated. Results are presented in the later part of this chapter.

Another way of changing the natural frequencies of the turbine is by altering the stiffness and inertia of the turbine using thickness modifications. Changing thickness of

the turbine blade would certainly change the flow pattern and cavitation behavior of the turbine. An alternative is to change only the thickness of the crown and the band. By modifying the crown thickness at the top and the band thickness at the outer diameter, the passage size and contour could remain unchanged. Detailed results and discussion of this option will also be given in this chapter.

3.2 Modal Analysis

3.2.1 Mode Shapes and Natural Frequencies

A finite element model for the full turbine (scale 1:1) is constructed and analyzed to obtain the natural frequencies and mode shapes. The first 25 mode shapes and natural frequencies were extracted. It is important to note that each cyclically symmetric mode would have produced another identical mode with the same frequency, but vibrating in a perpendicular plane.

The mode shapes were inspected and the natural frequencies are listed in Table 7 with a description of their corresponding mode shapes. The natural frequencies for the first 25 modes ranged from 43.4 Hz for mode-1 to 188.5 Hz for mode-25. These 25 mode shapes can be briefly categorized into 5 types: (1) polygonal shape (nodal diameter) on the band, (2) band rotating relative to the crown, (3) whole turbine swinging, (4) translational motion of band relative to the crown, and (5) irregular blade motions. Figure 22 – Figure 31 show deformation contour plots for mode-1 to mode-18.

The natural frequencies from modal analysis are compared with experimental results from BC Hydro. The comparison revealed a maximum difference of 11%. The very close agreement of the results indicate that the FE model closely simulates the turbine behavior. Table 8 compares the two results. It is important to note that new modes (not

found by experiment) were found by the FE model. This may be attributed to sensitivity and accuracy of measurements, the experimental set-up and the type of excitation used.

3.2.2 Distribution of Modal Stresses

Relative stress contour plots[5] of the blades for all modes are examined. The highest stress locations in each mode are recorded in Table 9. In the first 18 modes, critical stress areas were located on the suction side of the blade. Only mode-5, the 1st rotational mode at 58.42 Hz, exhibits high stress at the suction side of location [A] and [C] (for labeling refer to Figure 2). Figure 32 shows the relative stress contour plot of mode 5. It therefore, suggested that mode 5 may be the mode and natural frequency that caused fatigue cracking at location [A] and [C]. Results from harmonic response analysis (to be discussed below) would strengthen this argument.

3.2.3 Modal Analysis Simulating Scaled Down Turbine Model

In order to determine the relations of natural frequencies of the scaled-down turbine model (scale 1:14) to the full size turbine, an FE model of the scaled-down turbine model was also created with proper material properties. Basically the original FE model was shrunk down to one fourteenth of the size. The same fully fixed boundary conditions were applied to the inner rim of the extended crown.

The scaled-down model results are tabulated in Table 10. According to the FE results, the natural frequency of the scale-down turbine model is approximately 10.1 times higher than that of the actual full size model. The results are compared with reference [9] and the difference between the two sets of results is less than 7.1%. (Refer

---

[5] Stress level obtained from modal analysis does not represent actual stress level of the component. The stress level only represents relative stress magnitude on the blade.

to Table 10 for details). The 10.1 ratio of natural frequency may explain the reason why the manufacturer failed to predict possible resonance on the turbine. Details will be discussed later.

3.2.4 Effect of Spin Softening and Stress Stiffening to Natural Frequencies

The spin softening effect was included in the FE model and the rotational speed of the turbine was set to 150 RPM (15.71 radian/second). In addition, gravity and water pressure effect were also included using stress stiffening option in ANSYS.

Table 11 presents two sets of results: (1) effect of spinning plus gravity, (2) effect of spinning, gravity and water pressure. Both sets of data showed insignificant changes in natural frequencies with a maximum value of 0.37%. Therefore the effect of gravity, spinning and water pressure on the natural frequencies will be ignored.

It was surprising to find, however, that spin softening effect did not always decrease natural frequencies. It only decreased natural frequencies in rotational and translational mode. This may be attributed to a smaller effect of stress stiffening in these modes. For other mode shapes, natural frequencies were increased. Stiffness of these other mode shapes is highly dependent on the band and the crown stiffness. Centrifugal forces acting on the band or the crown would stiffen the component and, therefore, higher frequencies were observed.

3.2.5 Effect of Damping on Natural Frequencies

Due to implementation difficulties with added mass effect on turbine (as discuss in section 2.3), the modal analysis with added mass effect was not performed. We will, however, rely on experimental data to estimate the damping effect on the turbine.

Assuming the 1st rotational mode (590 Hz) to be the target mode shape. Reference [9] stated that damping effect reduced natural frequencies by 16.4% to 25.2% giving a final value of 494 Hz to 947 Hz. Therefore the reduction percentage would be about 18.3% by interpolation. This estimate is subject to two errors: (1) mode dependency of frequency reduction, and (2) applicability of interpolation for frequency reduction. On the other hand, BC Hydro results found that higher frequency modes would have higher reduction. Referring to spectral diagram, Figure 6, very small shift was recorded on the low frequency mode. Dry turbine model at 460 Hz showed 8.5% reduction in frequency. Therefore we estimated the natural frequency reduction for low frequency mode to range from 8.5 to 18.3%. Note that BC Hydro results were significantly lower than those of reference [9].

Comparing experimental natural frequency results with FE modal analysis results, it may be concluded that the FE model underestimated the turbine natural frequencies by a maximum of 11%. Therefore, natural frequency of the submerged turbine would change by +2.5% to -7.3% of the results from the modal analysis.

Since the damping effect is mode dependent and it cannot be accurately estimated, the following analyses were performed without damping. The overall effect of damping is discussed after each analysis.

3.3 Harmonic Response Analysis

3.3.1 Harmonic Response Analysis Results

Comparing the natural frequencies found from FE model to the excitation frequencies calculated in Table 6, 60 Hz and 170 Hz were closest to natural frequencies of mode 5 and mode 19. Therefore, it was believed that these excitations would cause the

most critical response. Harmonic response analysis was performed on each of the above excitation frequencies as well as another arbitrarily chosen 5 frequencies.

The FE model was fully fixed at the inner rim of the extended crown. Gravity and spinning effect were included. Water pressure from the CFD analysis was applied to the blades, crown and band. Since the FE model and CFD computation used different grids, a small computer program was used to interpolate the pressure data. Pressure distribution contour of the blade is shown in Figure 33. The figure shows a gradual reduction of pressure from the inlet to the outlet of the blade.

Seven (7) harmonic response analysis were performed using a total of 7 excitation frequencies. The von Mises stress results for these analyses are shown in Figure 34 to Figure 40. The results confirmed that the 60 Hz and the 170 Hz give the most critical response. Other excitation frequencies gave relatively low deformation and stresses.

Critical stress values and its location are tabulated in Table 12. At 60 Hz and 170 Hz, stresses were about 2170 MPa (315 ksi) and 7100 MPa (1030 ksi), respectively. For other excitation, stresses range from 93 MPa (13 ksi) to 730 MPa (105 ksi). Comparing with result of static analysis, the maximum stress was 200 MPa (29 ksi) located at [C]. Refer to Figure 46 for details. The comparison shows that if the excitation frequency does not coincide with a modal frequency, the resulting stresses will be comparable to static analysis results.

Comparing stresses at 60 Hz and 170 Hz, high stress concentration area (in the 60 Hz excitation) is located at the suction side, at [A] and [C]. On the contrary, stress concentration for the 170 Hz excitation is located on the pressure side, surrounding [A]. See Figure 42 and Figure 43 for details. Recalling the criteria set forth on determining 'correct' excitation frequency, the 60 Hz is chosen to be the 'correct' frequency.

On the other hand, the 60 Hz is the product of wicket gate number and rotational speed. This means that the excitation was originated from pressure variation as each blade passes by the wicket gates. The 170 Hz excitation is the 4th multiple of the product of blade numbers and rotational speed. This excitation, if existed, would be an indirect excitation.

Since maximum stress result in the harmonic response analysis of 60 Hz was much higher than the yield strength, nonlinear static analysis was performed to determine the effect of yielding. Bilinear material properties were used a yield stress value of 220 MPa (32 ksi).

The von Mises stress results of nonlinear static analysis are shown in Figure 42. It is interesting to note that large area on the blade is stressed up to yield point and, therefore, strain hardening is believed to occur [37]. Based on 60 Hz excitation frequency, the turbine experiences more than 10^9 cycles per year and a fair portion of the blade would strain harden and may be subjected to Bauschinger effect [37]. This may explain the high residual stress measured on the base metal by BC Hydro.

It should be also pointed out that the FE analysis predicted that the natural frequency of rotational mode would to change from –2.5% to 7.5% due to damping effect. The estimate is based on experimental results from BC Hydro and reference [9]. Water damping may increase the difference between rotational frequency and excitation frequency and, therefore, harmonic response of the turbine may be lower.

However, since the obtained results from 60 Hz excitation corresponded exactly to the observed cracking locations and matched the preset criteria, it may be concluded that the rotational mode natural frequency is close to 60 Hz in the actual turbine and that the

damping effect is not significant. Since accurate quantitative estimate was not possible, the damping effect would not be included in following analysis.

In considering the harmonic response for 60 Hz excitation, only a few percent of the total water pressure is assumed to contribute to the harmonic excitation. The rest of the pressure would be acting as static pressure.

Therefore the procedure of displacement superposition of harmonic response and static results was employed. The sum of displacements was fed into a nonlinear static analysis using bilinear material properties. The analysis result showed a more realistic stress contour of the blade under excitation of 2.5% and 5% of the total static pressure. Figure 44 and Figure 45 show the stress contour results of the blade at 2.5% and 5% excitation, respectively. The highest stresses at [A] at maximum loading were 214.4 MPa (31.1 ksi) and 229.6 MPa (33.3 ksi) at 2.5% and 5%, respectively. Minimum loading case is obtained and the results are later be used in the SIF range computation.

3.3.2 Explanation of Cracking Locations

The above analysis indicates that the fatigue cracks are stimulated by tangential excitation at 60 Hz. However, the runner is oscillating in a rotational mode and outer diameter should experience higher deformation and therefore high strain. This means that high stress areas should be expected at [B] and [C]. (Referring to Figure 2, the four corners of the blade were labeled clockwise using alphabets [A] to [D] starting from the crown-trailing-edge corner.) It is important to note, however, that by examining the deformation diagram of a blade at mode 5, it is found that high strain did occur at [A] and [C] because the nearby areas were unable to relieve stress by deformation. Referring to Figure 41, two important phenomena may be observed. First is that, only very small

41

deformation was observed at [A] compared to the deformation at [D]. However the curvature of the blade above [D] allowed room for deformation to relieve strain at this area whereas the crown at the inner edge was very stiff to allow such stress relief for point [A] and, therefore, it caused high stress at [A]. Secondly, similar phenomenon occurred at [C] where the leading edge of the blade is straight and allowed no room for deformation due to band movement. In contrary, strain at [B] was relieved by deformation of outer diameter of the crown. These two observations suggested that Francis type turbine is subjected to high stress at [A] and [C] when the turbine is excited at rotational mode.

3.3.3 Problem of Manufacturer's Model Test

Mitsubishi Heavy Industry Company had performed operational stress measurement on the turbine model. However, the measured results were very low. The stress level at [A] and [C] were 9.8 MPa (1.4 ksi) and 66.9 MPa (9.1 ksi), respectively.

Based on the FE model results, 60 Hz excitation may cause the turbine to resonate. That is, the pressure variation as the blade passes the wicket gate excites the turbine. Recall that the manufacturer used 1062 RPM on the turbine model, which is 7.08 times of the rotational speed of the actual turbine whereas the natural frequency ratio of the model to actual turbine is 10.1 times. The pressure variation experienced by the model would, therefore, be 424.8 Hz[6]. Noting that the rotational mode frequency of the model is 587.8 Hz, the excitation source would not match the rotational mode frequency in the model test. I believe that this is the reason why the manufacturer failed to predict resonance and produced a low operational stress measurement.

---

[6] Excitation frequency = number of wicket gate × rotational speed = 24 × (1062/60) = 424.8 Hz

Operational stress test on a small size model should be handled with care with predicting resonance behavior. Even if the ratio of rotational speeds and the ratio of natural frequencies are equal, the model may still experience lower response. It is because the difference between the excitation frequency and natural frequency would be increased by the same scaling factor in the model test. Since resonance response is inversely proportional to difference of the square of the natural and excitation frequencies[7], the response is expected to be lower and more difficult to detect in model test.

3.4 Fatigue Life Prediction

Fatigue Life of a component consisted of crack initiation life and crack propagation life. As discussed in the theory section 2.7, the initiation life would be determined using strain life equation, Equation (31); whereas the propagation life would be determined using Paris Law, Equation (34).

The 3D solid submodel was used for this computation. Due to cyclic symmetry of the turbine response at 60 Hz excitation, one seventeenth of the turbine is sufficient to represent the full structure. To produce an accurate estimate of the SIF range, a finer 3D mesh was used. The model was composed from shell and solid element as shown in Figure 18. The purpose of the shell element was to transfer the displacement boundary condition to the solid submodel. All displacement boundary conditions were applied to the shell elements. No displacement constraint was applied to the solid model. Strain range and SIF range was calculated using the difference of the results from maximum and minimum displacement conditions.

---

[7] System response $\propto 1/(\omega^2 - \omega_n^2)$ where ω = excitation frequency; ω_n = natural frequency

43

3.4.1 Initiation Life Prediction

A nonlinear static analysis for a no-crack solid submodel was used to produce total strain result. The strain difference between maximum and minimum loading conditions was considered as the total strain range. The analyses were performed on both 2.5%HR loading and 5%HR loading case. The total strain range results and the predicted initiation life of the two loading cases were tabulated in Table 13. Life computation was done using MathCAD, (details are shown in Appendix E). The total strain range for 2.5%HR and 5% HR loading was 6.5E-4 and 1.2E-3, respectively. The strain ranges were small, and therefore the predicted were found to be 2.06E+9 cycles and 2.36E+7 cycles for 2.5%HR and 5%HR, respectively. These cycles are only equivalent to 397.7 and 4.6 days, respectively.[8].

3.4.2 Propagation Life Prediction

A series of cracked solid submodels were used to produce SIFs for propagation analysis. A through-thickness edge crack was modeled on the blade and was extended from 2.5 mm (0.098 in) to 154.7 mm (6.09 in) using 25 models or steps. A total of 25 SIF ranges were computed using the difference between maximum and minimum stresses. To include the 2.5%HR and 5%HR loading cases, a total of 100 linear static analysis were performed.

In ANSYS, SIF computation is based on plain strain or plain stress conditions. Results from both approaches are calculated and presented in Table 14. The predicted propagation life from plain stress formula is 35% higher than that of plain strain. Based on the plain strain formulation, for 2.5%HR loading case, the SIF ranged from 11

---

[8] Assumes full power operation for one year. Annual cycles = 60×3600×24×365.25 = 1.90E+9 cycles

MPa√m to a peak of 25.6 MPa√m and then dropped to about 18 MPa√m. For the 5%HR loading case, the SIF ranged from 21 MPa√m to a peak of 54.3 MPa√m and then dropped to 36 MPa√m. The SIF values were expected to drop linearly as the crack tip moved away from high stress concentration point as shown in Figure 47 and Figure 48. Using plain stress conditions, the SIF range (ΔK) results are about 10% lower. Plain strain results were used in the following analysis to obtain conservative predictions.

Utilizing Equation (42), the crack growth rate was determined and the propagation life was then obtained using trapezoidal rule. The propagation life results are listed in Table 15. It was found that the propagation lives were quite low compared to the initiation life. Based on plain strain formulation, propagation only contributed to 1.16E+6 cycles and 1.26E+5 cycles for 2.5%HR and 5%HR loading, respectively. The propagation lives were 0.05% and 0.5% of the total life for 2.5%HR and 5%HR loading, respectively. Therefore, the total fatigue lives were about 398 days for 2.5%HR loading, and about 4.6 days for 5%HR loading.

3.4.3 Implications and Error Discussion from the Fatigue Life

The above fatigue life prediction results indicate several important aspects of the turbine cracking problem. These are summarized and discussed below.

(1) From the above results, it is shown that the percentage of the head pressure used in the harmonic analysis significantly affects the response and the life of the turbine. The 2.5% and 5% are more or less, arbitrary chosen values. It is therefore, concluded that some analysis, experimental testing and/or more study leading to more accurate prediction of this percentage is crucial in calculating the blade fatigue life.

(2) The FE model prediction under the assumed loading condition is conservative. BC Hydro has found a crack of 560 mm (22 in) after 3 years of operations. On the other hand, FE model predicted 154.7 mm (6.09 in) crack in 1.09 years. It seems that the actual crack growth rate in the propagation stage is lower than the FE predicted rate. Therefore, the turbine runner may have experienced a similar or lower magnitude of resonance at the 2.5%HR loading case.

(3) Sensitivity to pressure variation may indicate that the turbine was running in an unstable conditions. This, also, may have been the cause of inconsistent cracking behavior. Pressure variation is also sensitive to individual blade contour and clearance between blade and wicket gates. This may also explain why some blades always crack, whereas some blades never crack.

(4) In addition to pressure variation, underestimation of fatigue life could be related to the following reasons: (i) rotational mode natural frequency being too close to the excitation frequency, (ii) lack of damping effect in the FE model, and (iii) empirical errors in life prediction equations.

(5) Residual stress was not considered in the above prediction. This may affect crack propagation prediction. However, such computation was not possible because of the lack of accuracy of material constants and quantitative values for residual stresses.

3.5 Turbine Design Modifications

Owing to the fact that head pressure, rotational speed and wicket gate numbers were preset, modifications of the turbine were focused on altering natural frequency of the rotational mode shape. Altering inertial mass and/or stiffness of the system may offset

natural frequencies of the turbine to a more desirable range. Structural inertia of the turbine at rotational mode is mainly affected by moment of inertia of the band whereas structural stiffness is affected by both crown and blade thickness.

To alter natural frequency at rotational mode, two approaches were used: (1) installation of blade stiffeners, and (2) modifications of thickness of turbine blade. Modifications were targeted at changing the natural frequency by 15% or higher. It was believed that this percentage change could introduce a sufficiently large difference between natural and excitation frequencies, so that resonance could be significantly reduced.

3.5.1 Installation of Blade Stiffeners

3.5.1.1 40-70 Blade Stiffeners

The first blade stiffener design was suggested by BC Hydro. The blade stiffeners are steel rods of 2.22 cm (7/8 inch) in diameter and 20.3 cm (8 inches) in length. Each stiffener is connected at one side to the trailing edge of a blade, located at 70% of the edge length measuring from the crown, and connected on the other side to the surface of suction side of a blade. The other blade stiffener was connected in a similar manner but located at 40% of the vertical distance from the crown.

The stiffener arrangement is shown in Figure 49. This arrangement would be referred to as 40-70 blade stiffeners. These stiffeners were easy to install and it minimized blockage of the water passage between blades.

In Table 16, the modal analysis results are compared with the experimental results obtained by BC Hydro. FE model reproduced very agreeable results compared to experimental findings. Based on FE model results, the 40-70 blade stiffeners were not

effective in increasing natural frequency of the rotational mode shape. Only 0.5% increase was obtained for the rotational mode. This result was expected because the arrangement of 40-70 stiffeners did not increase the structural stiffness of the turbine to prevent rotation of the band relative to the crown. Instead, it prevents relative motion of blades.

Another concern with this stiffener arrangement is that mode 9 and 10 frequency was changed from 115.59 to 121.44 Hz. Also mode 19 frequency was changed from 170.72 to 178.77 Hz. Therefore the 60 Hz excitation could stimulate these two super-harmonics and create a more severe cracking situation.

3.5.1.2 Crossbar Stiffeners

The most direct way to increase the rotational stiffness is to install cross bars from crown-blade intersection of one blade to band-blade intersection of another blade. Crossbars were simulated using beam or bar element and placed inside the water passage to produce maximum effect on structural stiffness. Several different arrangements were considered, including multiple bars. FE results from modal analysis show that such arrangement could increase the rotational natural frequency by 15% or more. However, there were several problems with this arrangement.

(1) Increasing rotational natural frequency by 10% or higher would require two or more 1" diameter solid bar installed in the water passage between blades. This arrangement would block water flow and decrease efficiency of the turbine.

(2) Crossbars had low natural frequencies. Their frequencies ranging from 70 to 90 Hz depending on total length and diameter of the bar. There is a concern,

therefore, that vortex shedding may stimulate these natural frequency and produce more serious damage to the turbine.

(3) Installation of crossbars was intended to stiffen the structure of the turbine, share harmonic loading and experience very high tensile or compressive stress. Results from FE models confirmed this concern. Therefore shear or buckling failure is possible.

(4) Installation of crossbar required welding. Therefore more areas of the turbine might be affected by high residual stress.

Crossbar stiffener was, therefore, not considered to be a feasible solution to alter rotational natural frequency.

3.5.2 Thickness Modifications

Thickness modification is another method of altering natural frequency of the turbine. Reducing band thickness, and increasing crown and blade thickness would raise the natural frequency and vice versa.

If modifications are done from the top of the crown and the outer surface of the band, the water passage may be kept unaffected making this method to be a desirable one. The area of modifications included the middle section of the band, and the entire crown excluding the extended crown. Refer to Figure 50 for details. The effects of the modifications were analyzed using modal analysis and the results are tabulated in Table 17.

Results showed that reducing the band thickness by 55.7% could increase rotational mode natural frequency by 5.3%. On the other hand, increasing the crown thickness by 60% could increase the natural frequency by 9.8%. Therefore, the modifications were

combined. By reducing the band thickness by 60% and increasing the crown thickness by 60%, the total natural frequency increase was 15.5%. However, such large modifications to the turbine could cause structural weakness and therefore, it was not considered as a feasible solution.

4 Conclusion

The turbine-cracking problem of GMS power generating station started in 1972. Previous research did not determine the causes of such fatigue cracks. Finite element analysis provided insightful results and suggested the cause and the mechanism of cracking of the turbine runners.

Modal analysis of the turbine runner indicated that mode shape at 58.42 Hz produces high stress concentrations at the cracking areas, suction side of location [A] and [C]. Spinning and gravity were considered in the analysis but they were found to be insignificant. Harmonic response analysis confirmed that excitation frequency at 60 Hz causes high strain at the cracking locations. Therefore, it was concluded that the fatigue cracks were induced by the excitation originated from pressure variation as the turbine blades pass by the wicket gates.

On the other hand, modal analysis on the FE model of the manufacturer turbine model suggested that manufacturer model test may not predict resonance. This was due to the different scaling factors that were used in power conversion and size conversion. In addition, nonlinear static analysis suggested that strain hardening could induce high residual stress on the turbine blade and this explains the existence of high residual stress measured outside the stainless steel overlay on non-cracking blades.

By examining the deformation plot of a turbine blade at 58.42 Hz, it was found that the high strain located at [A] and [C] may be attributed to the fact that their surrounding areas are too stiff to deform. Fatigue crack prediction using strain life equation and Paris Law indicated very short fatigue life of the turbine. The results also suggested that the fatigue life is very sensitive to the amplitude of pressure variation used in harmonic

response analysis. This might explain the inconsistent cracking behavior between different turbine runners.

Finally, modifications of the turbine were suggested and analyzed using modal analysis. However, results of the FE analysis suggested that all proposed modifications might not be considered as feasible solutions. For instance, installation of 40-70 blade stiffeners could not provide sufficient change to rotational mode natural frequency whereas crossbar stiffeners would block water passage and reduce efficiency of turbine. On the other hand, thickness modifications required very high thickness change to obtain 15% natural frequency change. It is believed that this may cause structural weakness to the turbine.

5 Reference

1. "Portage Mountain Project Design Report", BC Hydro and Power Authority: Hydroelectric Engineering Division Report # 1756, 12/1/634, October 1988.

2. Franklin, D. E., Moysa, N., "Investigation into Francis Turbine Runner Blade Cracking", BC Hydro and Power Authority Report, File # GMS 1135-01-10-G1-v3.

3. Streat, N., "Cracking of Large Hydraulic Turbine Runners", BC Hydro and Power Authority Report, Project 2137-77-M4, 16th Conference of Metallurgists, August 21-25, 1977.

4. Beaney, E. M., Procter, E., "A Critical Evaluation of the Center Hole Technique for the Measurement of Residual Stress", Berkeley Nuclear Laboratories, Research Department, Central Electricity Generating Board, RD/B/N2492, Nov. 1972.

5. Beaney, E. M., "Accurate Measurement of Residual Stress on Any Steel using the Center Hole Method, Berkeley Nuclear Laboratories", Research Department, Central Electricity Generating Board, RD/B/N3568, Dec. 1975.

6. Streat, N., "Residual Stress Measurements on Turbine Runners at G. M. Shrum Generating Station", BC Hydro and Power Authority Report, Project #: 550-76-Gld, June 1976

7. Ando, J., Watanabe, T., Namata, H., Tamura, S., "Preliminary Test Results of Runner Vane Stress under similar Operation to Prototype Water Turbine: 266,000 kW for Portage Mountain P/S, BC Hydro, in Canada", Mitsubishi Heavy Industries Ltd. Report, Hydrodynamic Research Laboratory, Mitsubishi Heavy Industries Ltd., Japan, July 23, 1973

8. Franklin, D. E., "Prototype Testing of Unit 4 at Gordon M. Shrum Generating Station for Turbine Blade Stress Levels", BC Hydro and Power Authority Report, 1974

9. Hazell, C. R., "Experimental Investigation of the Dynamic Behavior of a Model Turbine Runner for BC Hydro and Power Authority", Department of Mechanical Engineering, the University of British Columbia, November 10, 1975

10. Coutu A., "GMS Unit 1-5 Model Runner Measurements", GE Hydro (Canada) Inc., Report, May 1997

11. Bathe, K. J., *Finite Element Procedure*, Prentice Hall, New Jersey, 1996

12. Grimes, R. G., Lewis, J. G., Simon, H. D., "A Shifted Block Lanczos Algorithm for Solving Sparse Symmetric Generalized Eigenproblems", *SIAM Journal Matrix Analysis Applications*, v.15, (1), 1994, pp.228-272.

13. Dimarogonas, A., *Vibration for Engineers*, 2nd Edition, The Prentice Hall, New Jersey, 1996.

14. Carnegie, W., "Vibration of Rotating Cantilever Blading", *Journal of Mechanical Engineering Science*, v.1, n.3, 1959

15. Cook, R. D., *Concepts and Applications of Finite Element Analysis*, 2nd Edition, John Wiley and Sons, New York, 1981

16. Vernon T. A., Bara, B., Hally, D., "A Surface Panel Method for the Calculation of Added Mass Matrices for Finite Element Models", Technical Memorandum 88/203, Defense Research Establishment Atlantic, National Defense, Canada, February 1988

17. Hess A. M. O., Smith J. L., "Calculation of Non-lifting Potential Flow About Arbitrary Three-Dimensional Bodies", Report E. S. 40622, Douglas Aircraft Co., 1962

18. Vorus W. S., Hylarides S., "Hydrodynamic Added Mass Matrix of Vibrating Ship Based on a Distribution of Hull Surface Sources", *Trans. SNAME*, v. 39, 1981, pp.397-416

19. Hylarides, S., Vorus, W. S., "The Added Mass Matrix in Ship Vibration Using a Source Distribution Related to the Finite Element Grid of Ship Structure", *Int. Shipbuilding Progress*, v.29, n.330, 1982

20. Rajasankar, J., Iyer N. R., Appa Rao, T. V. S. R., "A New 3-D Finite Element Model to Evaluate Added Mass For Analysis of Fluid-Structure Interaction Problems", *International Journal for Numerical Methods in Engineering*, v.36, 1993, pp.997-1012

21. Ramsey, J. K., Kaza, K. R. V., "Concentrated Mass Effects on the Flutter of a Composite Advanced Turboprop Model", *NASA Technical Memorandum*, # 88854, Oct. 1986

22. Zhang, S. M., "Added Mass of Underwater Plates and Beam Stiffened Plates in Vibration", *Journal of Hydrodynamics*, Ser. B, n.2, 1991, pp.13-20

23. Howe, M. S., "Elastic Blade Vortex Interaction Noise", *Journal of Sound and Vibration*, v.177, n.3, 1994, pp.325-336

24. Heskestad G., Olerts, D. R., "Influence of Trailing Edge Geometry on Hydraulic Turbine Blade Vibration Resulting from Vortex Excitation", *Journal of Engineering for Power*, April 1960, pp.103-110

25. Netto R., "Hidroelastic Vibration of Stay Vanes of Hydraulic Turbines", Work Group on the Behavior of Hydraulic Machinery under Steady Oscillatory Conditions, International Association for Hydraulic Research, Sept. 9-11, 1987, Lille France, pp.1-18

26. Hunt, J. C. R., "Vorticity and Vortex Dynamics in Complex Turbulent Flows", *Transaction of CSME*, v.11, n1, 1987, pp.21-35

27. Xu, R., Evans, R. L., "Numerical Simulation of Three-Dimensional Flow in a Francis Turbine at the BC Hydro G. M. Shrum Station", Department of Mechanical Engineering, The University of British Columbia, Canada, 1997.

28. Sih, G. C., *Mechanics of Fracture Initiation Propagation: surface and volume energy density applied as failure criterion*, Kluwer Academic Publishers, Dordrecht, The Netherlands, 1991.

29. Gdoutos, E. E., *Problems of Mixed Mode Crack Propagation*, Martinus Nojhoff Publishers, The Hague, Netherlands, 1984

30. Nuismer, R. J., "An Energy Release Rate Criterion for Mixed Mode Fracture", *Int. J. of Fracture*, Vol. 11, 1975, pp. 245-250

31. Erdoggan, F. and Sih, G.C., "On the Crack Extension of Plates Under Plane Loading and Transverse Shear", *J. Basic Eng.*, Vol. 85, 1963, pp. 519-527

32. Wang, J, "Arbitrary Lagrangian-Eulerian Method and its Application in Solid Mechanics", Ph.D. Thesis, Department of Mechanical Engineering, The University of British Columbia, Canada, 1998

33. Paris P. C., Sih, G. C., "Stress Analysis of Cracks, Fracture Toughness and Testing and its Applications", *American Society for Testing and Materials*, Philadelphia, STP 381, pp.30-83 (1965)

34. Fok, S. C. M., "New Design for Pressure Washer Drums" M.A.Sc. Thesis, Department of Mechanical Engineering, The University of British Columbia, Canada, 1997

35. Lukas, Petr, Fatigue Crack Nucleation and Microstructure, Fatigue and Fracture of Metals, *ASM handbook.*

36. Kocanda, S., *Fatigue Failure of Metals*, Sijihoff & Noordhoff International Publishers, Warsaw, Poland, 1978

37. Hertzberg, R. W., *Deformation and Fracture Mechanics of Engineering Materials*, 4th Edition, John Wiley & Son Inc., 1996, pp.294-295

38. Shih, T., Araki, T., *Trans. Iron Steel Inst.*, Japan, v.13, 1973, pp.11-19

39. Miller, K. J., "Initiation and Growth Rates of Short Fatigue Cracks", *Fundamentals of Deformation and Fracture*, Eshelby Memorial Symposium, England, 1984, pp.477-500

40. Kitagawa, H., Takahashi, S., *Int. Conf. Mech. Behavior of Materials*, ASM, 1976, pp.627-631

41. Kujawski, D., Ellyin, F., "Crack Initiation and Total Fatigue Life of a Carbon Steel in Vacuum and Air", *Journal of Testing and Evaluation*, v.20, Nov. 1992, pp.391-395

42. Kujawski, D., Ellyin, F., "A Cumulative Damage Theory for Fatigue Crack Initiation and Propagation", *International Journal of Fatigue*, v.6, n.2, 1984, pp.169-192

43. Socie, D. F., Artwohl, P. J., "Effect of Spectrum Editing on Fatigue Crack Initiation and Propagation in a Notched Member", *ASTM STP 714*, 1979, pp.3-23

44. Landgraf, R. W., "High Fatigue Resistance in Metals and Alloys", *ASTM STP 467*, Philadelphia, 1970

45. Kaynak, C., Ankara, A., Baker, T. J., "Initiation and Early Growth of Short Fatigue Cracks at Inclusion", *Material Science and Technology*, v.12, May 1996, pp.421-426

46. Paris, P. C., Bucci, R. J., Wessel, E. T., Clark, W. G., Mager, T. R., "Extensive Study of Low Fatigue Crack Growth Rate in A533 and A508 Steels", *ASTM STP 513*, 1972, pp.141-176

47. Verreman Y., Espinosa, G., "Mechanically Short Crack Growth from Notches in a Mild Steel", *Fatigue Fracture of Engineering Material Structures*, v.20, n.2, 1997, pp.129-142

48. Elber, W., "Fatigue Crack Propagation", Ph.D. Thesis, University of New South Wales, Australia, 1968

49. Elber, W., *Engineering Fracture Mechanics*, v.II, n.1, Pergamon Press, July 1970

50. Forman, R. G., Kearney, V. E., Engle, R. M., "Numerical Analysis of Crack Propagation in Cycle Loaded Structures", *Journal of Basic Engineering*, Transaction of the ASME, v.89, n.3, 1967, pp.459-464

51. Willenborg, J., Engle, R. M., Wood, H. A., "A Crack Growth Retardation Model using an Effective Stress Concept", *AFFDL-TM-71-1-FBR*, 1971

52. Broek, D., *Elementary Engineering Fracture Mechanics*, Martinus Nijhoff Publisher, The Hague, 1982

53. Harrison J. D., "The Effect of Residual Stress on Fatigue Behavior, Residual Stresses and Their Effect", *The Welding Institute*, Cambridge, 1981, pp.9-16

54. Maddox, S. J., "Influence of Tensile Residual Stresses on the Fatigue Behavior of Welded Joints in Steel", *Residual Stress Effects in Fatigue, ASTM STP 776*, 1981, pp.63-96

55. Itoh, Y. Z., Suruga, S., Kashiwaya, H., "Prediction of Fatigue Crack Growth Rate in Welding Residual Stress Field", *Engineering Fracture Mechanics*, v.33, n.3, 1989, pp.397-407

56. Gurney, T. R., "The Effect of Residual Stress, Fatigue of Welded Structures, 2nd Edition", *The Welding Institute*, Cambridge, 1979, pp.226-243

57. Parker, A. P., "Stress Intensity Factors, Crack Profiles, and Fatigue Crack Growth Rates in Residual Stress Fields", *Residual Stress Effects in Fatigue, ASTM STP 776*, 1981, pp.13-31

58. Nelson, D. V., "Effects of Residual Stress on Fatigue Crack Propagation", *Residual Stress Effects in Fatigue, ASTM STP 776*, 1981, pp.172-194
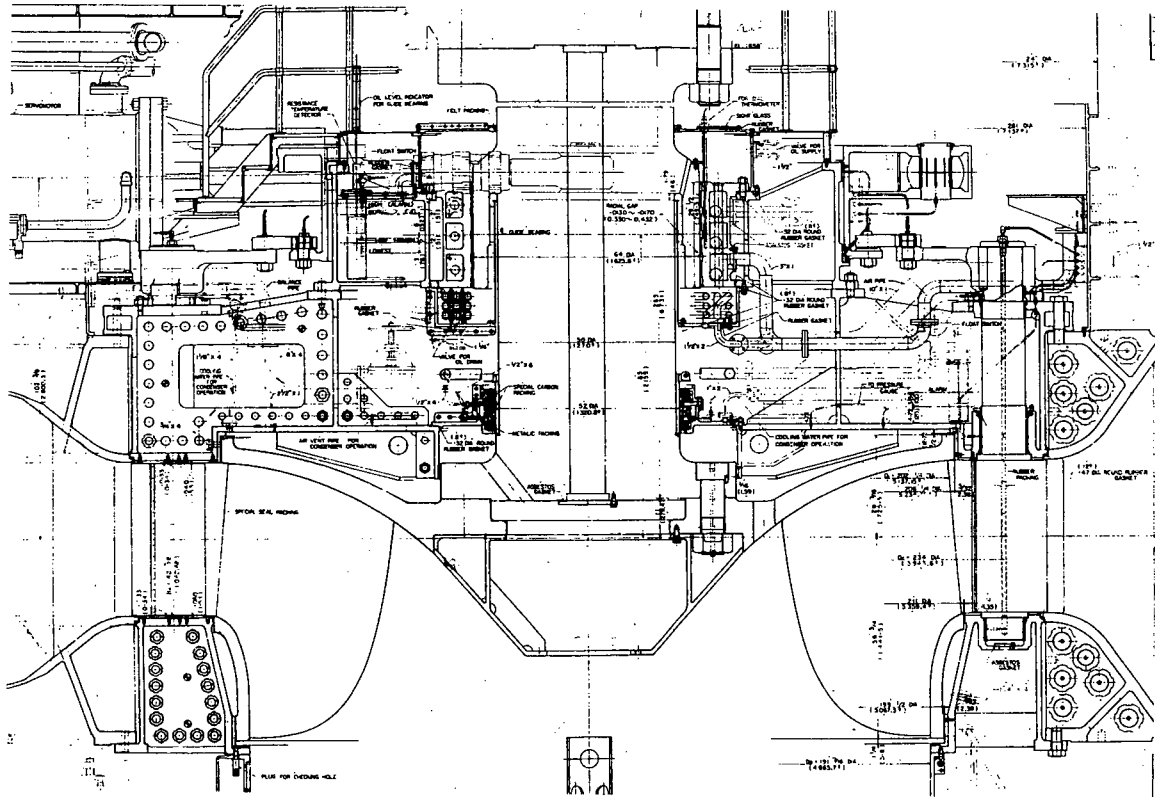
Figure 1: Cross Sectional View of the Turbine Runner Compartment
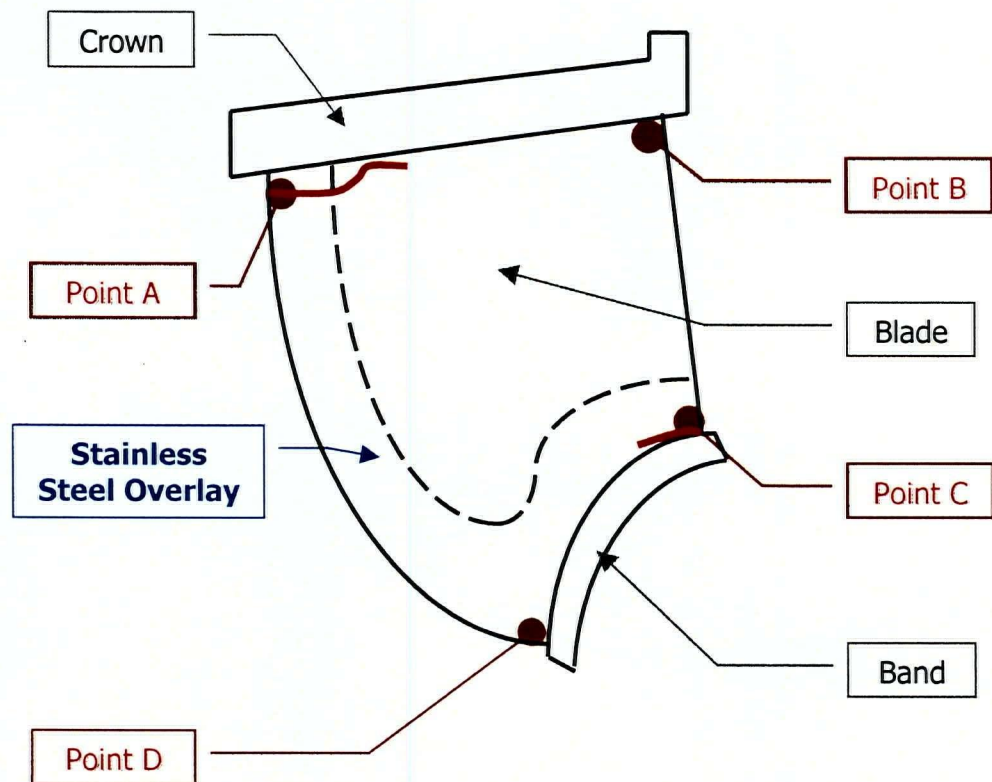
Figure 2: Schematic Diagram of the Cracking Locations and the Stainless Steel Overlay
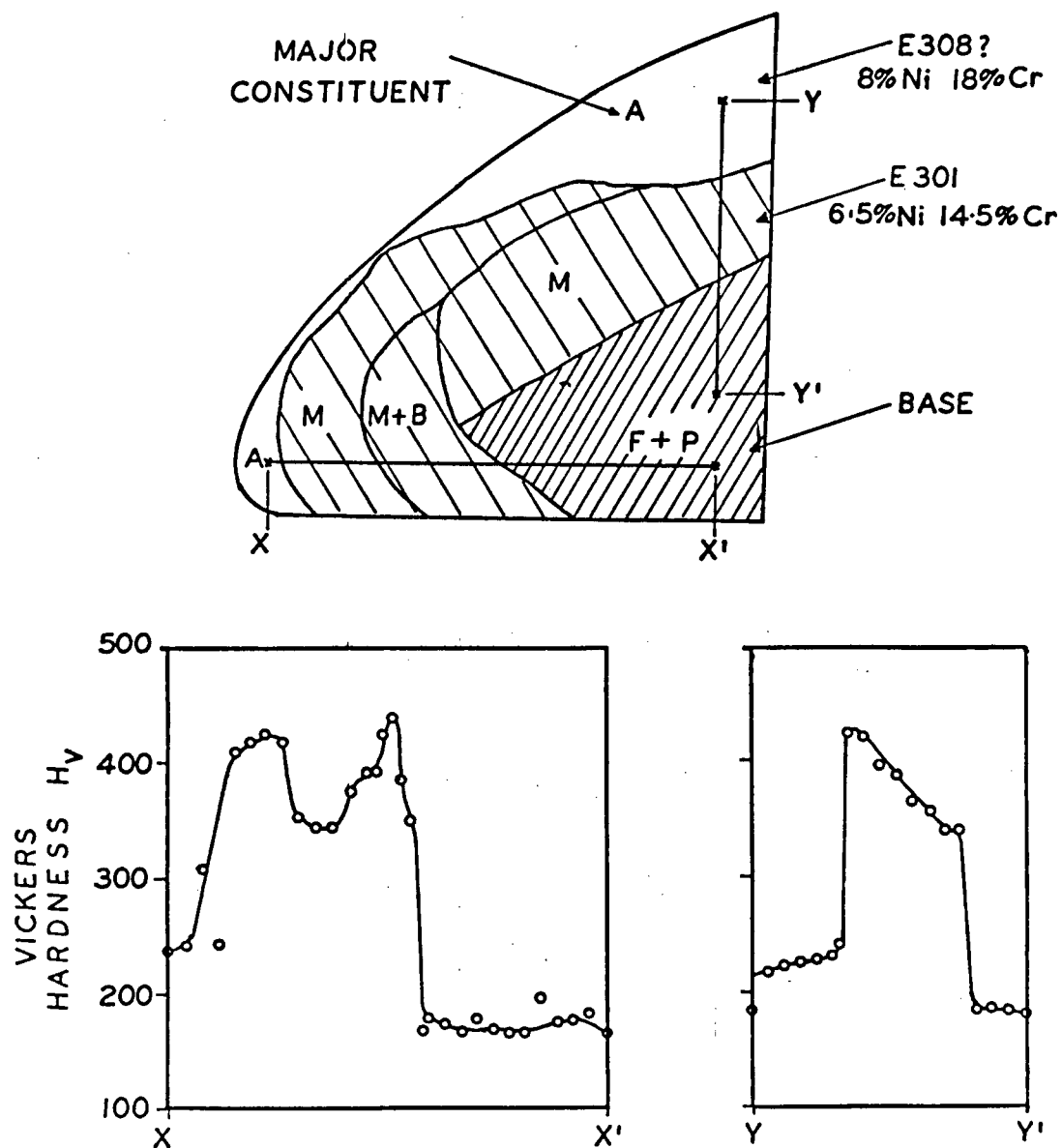
Figure 3: Schematic Representation of the Various Structural Regions in Etched Macrograph of the Blade Tip Region.

A = Austenite
B = Bainite
F = Ferrite
M = Martensite
P = Pearlite
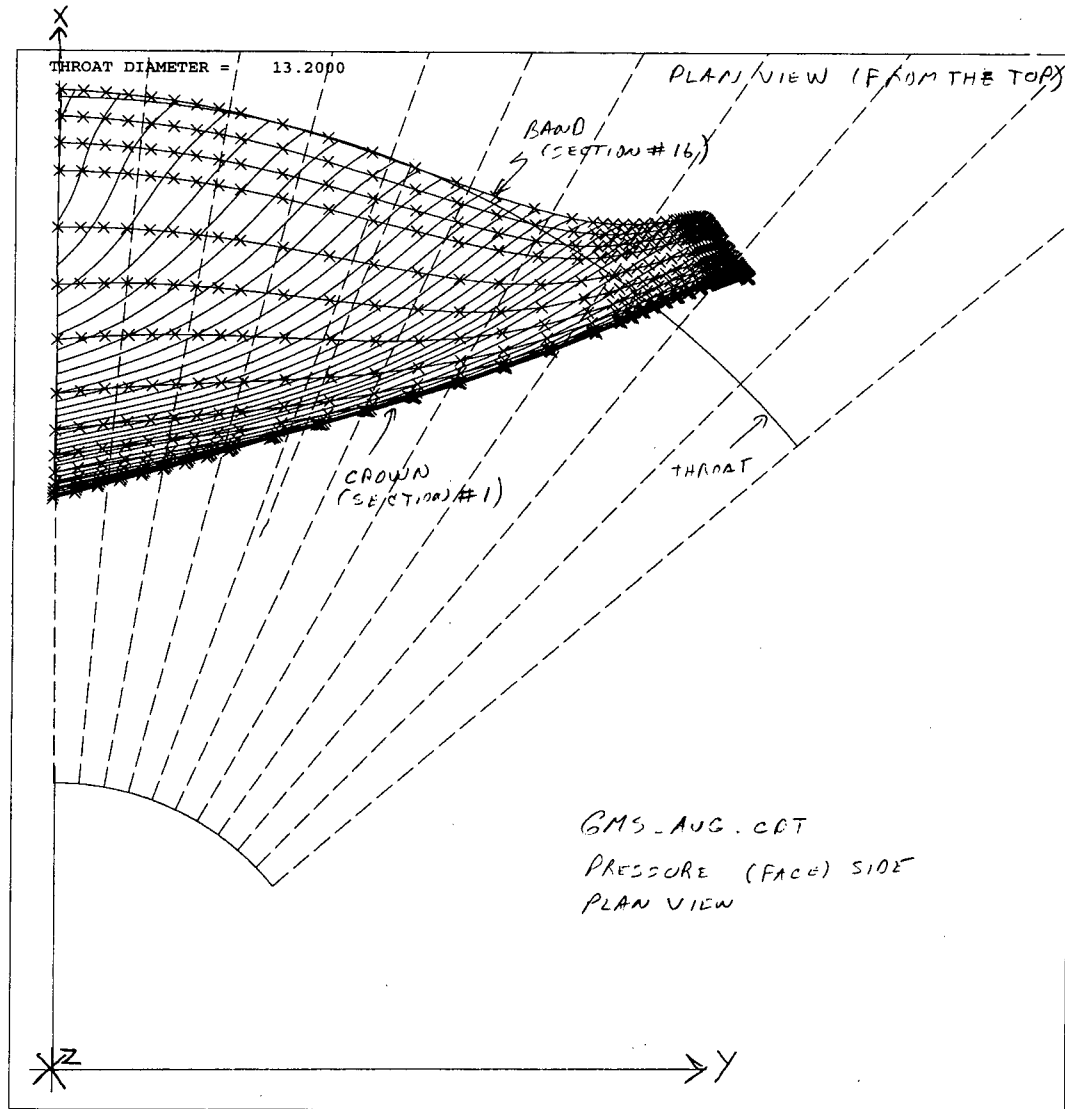
Figure 4: Contour Measurement Data Point Arrangement
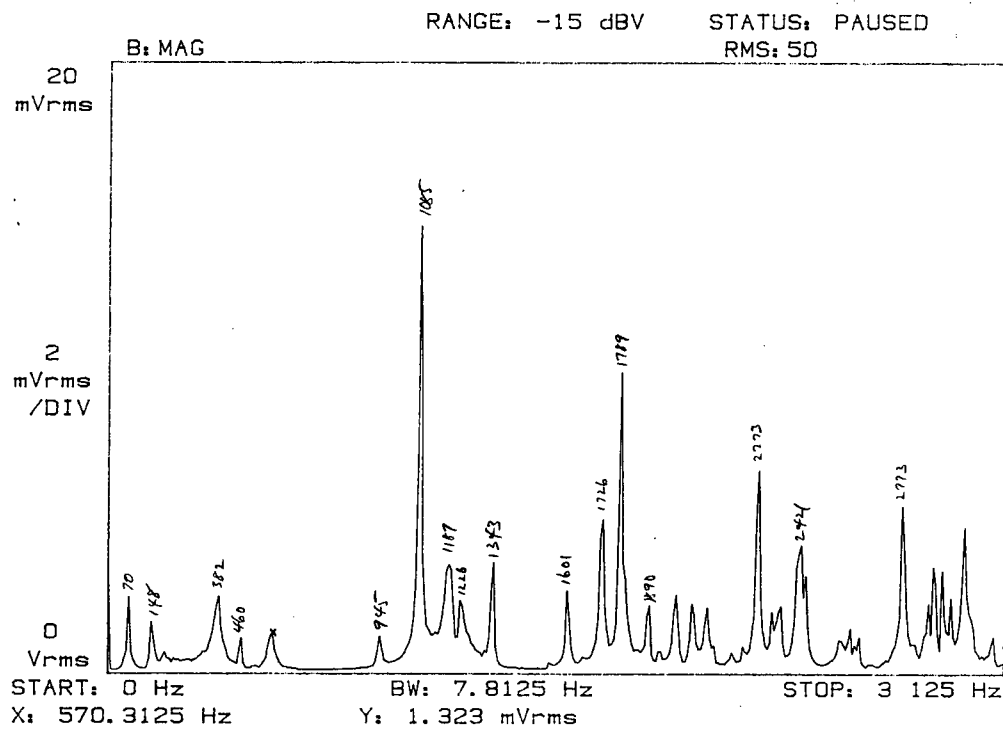
Figure 5: Spectrum Diagram of Turbine Model

(The turbine model was shaken tangentially at the band, and response was measured at blade 15 where it intersects the band.)
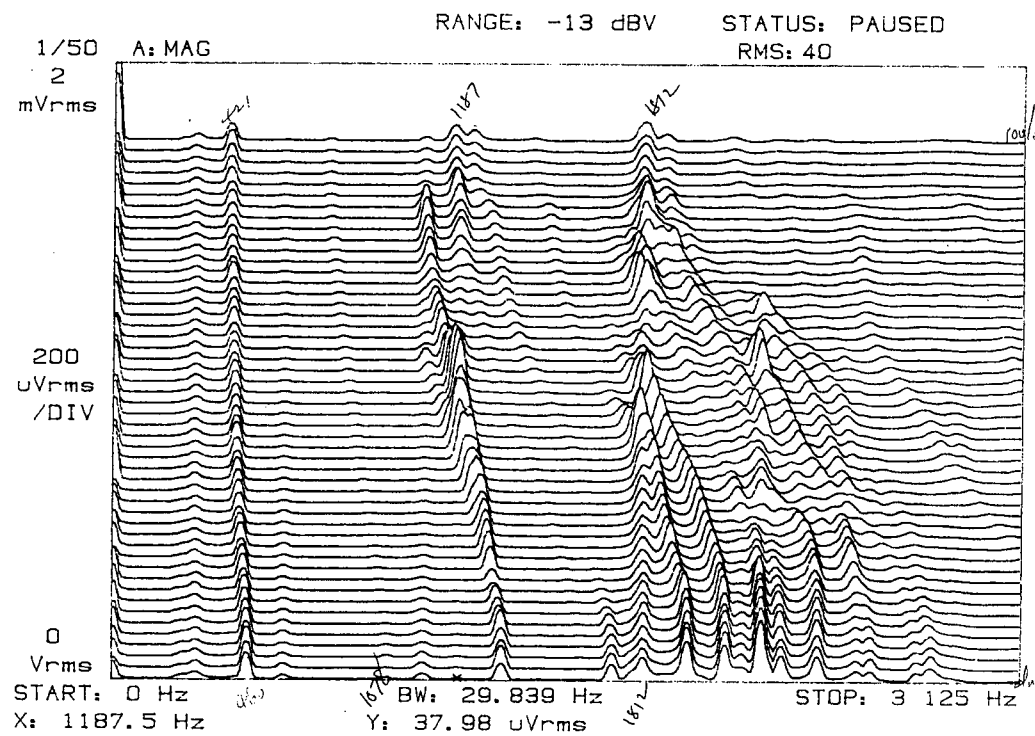
Figure 6: Spectral Map of the Turbine Model

(The turbine model was shaken vertically by random excitation, response was measured at blade 14 where it intersects the band.)
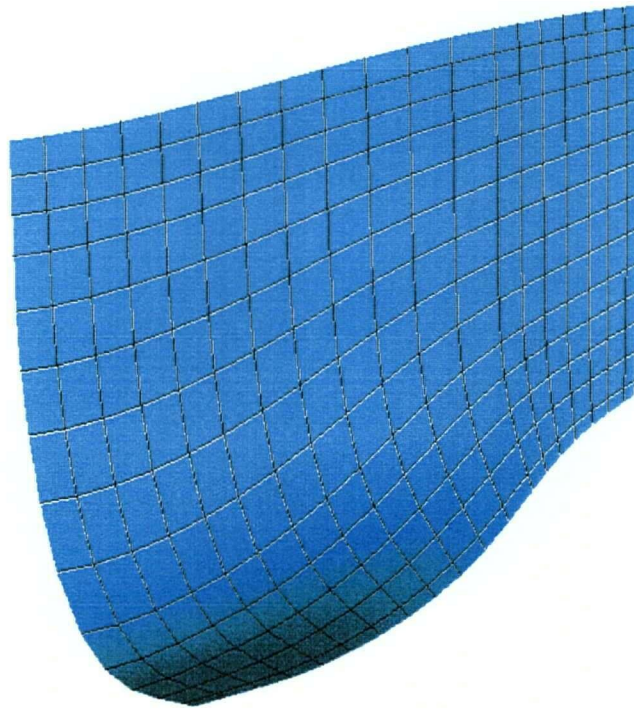
Figure 7: Blade FE Model
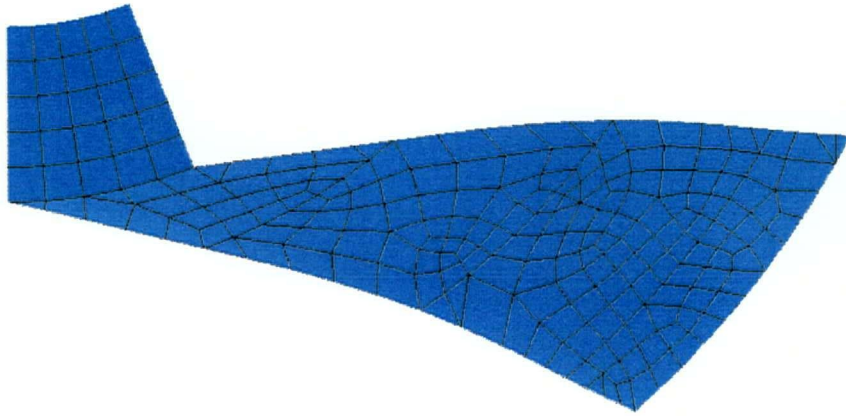
Figure 8: Crown FE Model
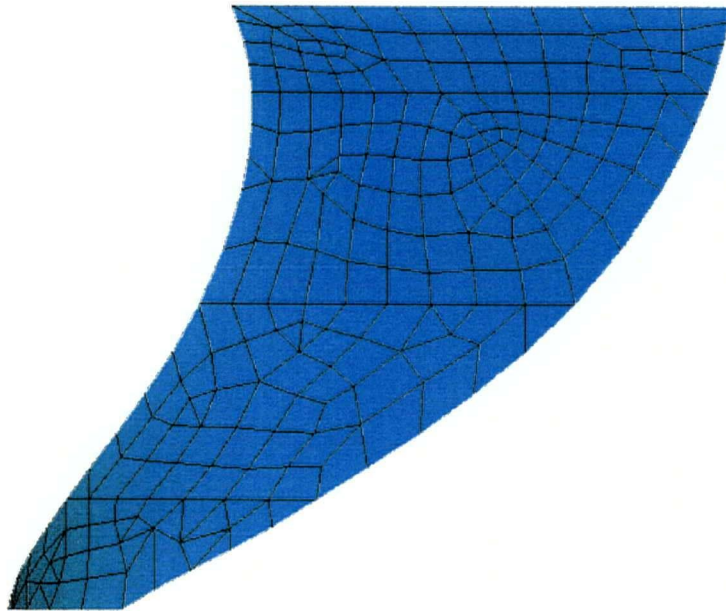
Figure 9: Band FE Model

65
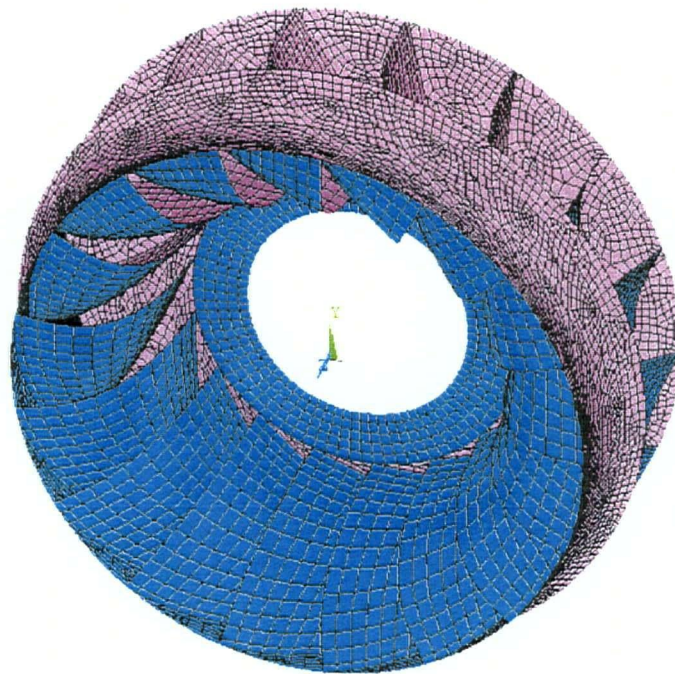
Figure 10: Full Turbine Model
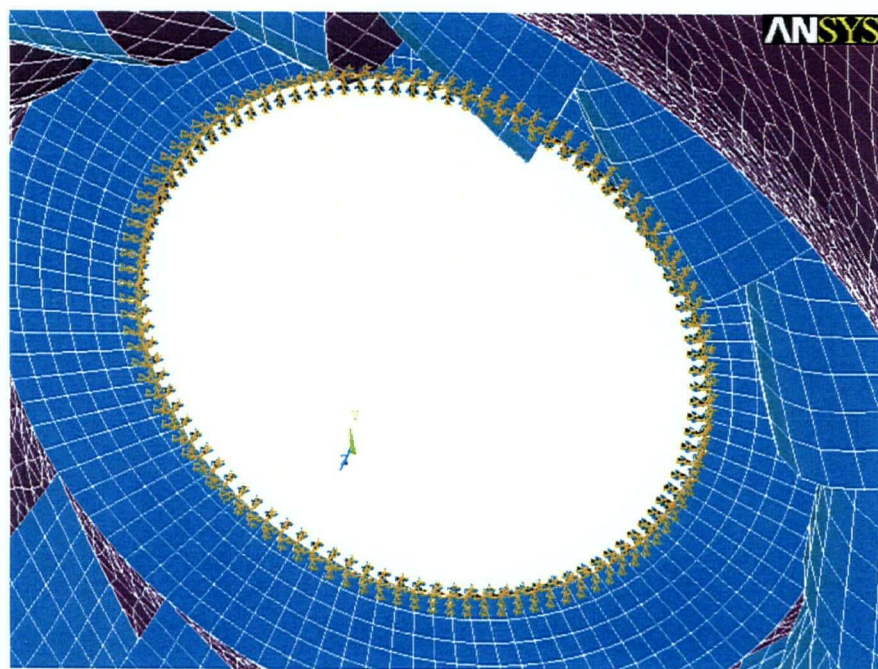
Figure 11: Applied Displacement Boundary Condition
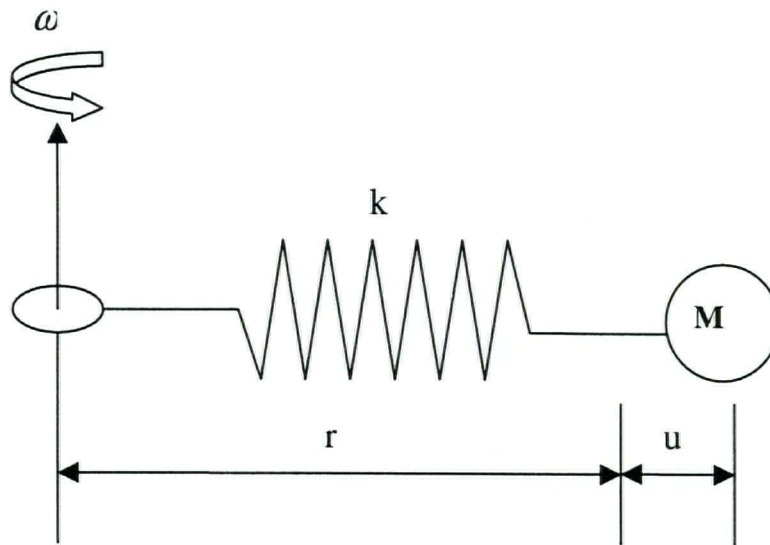
Figure 12: Spinning Spring Mass System
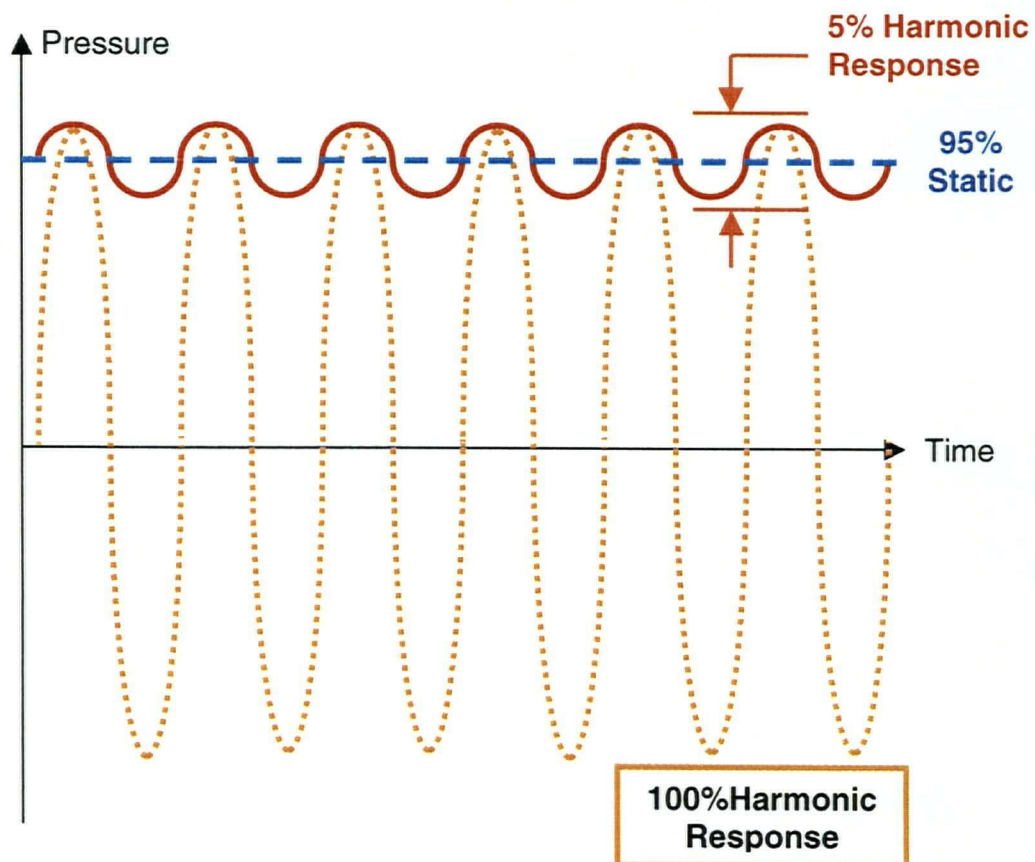
Figure 13: Schematic Explanation for Superposition of Harmonic Response Analysis Result and Static Analysis Result.
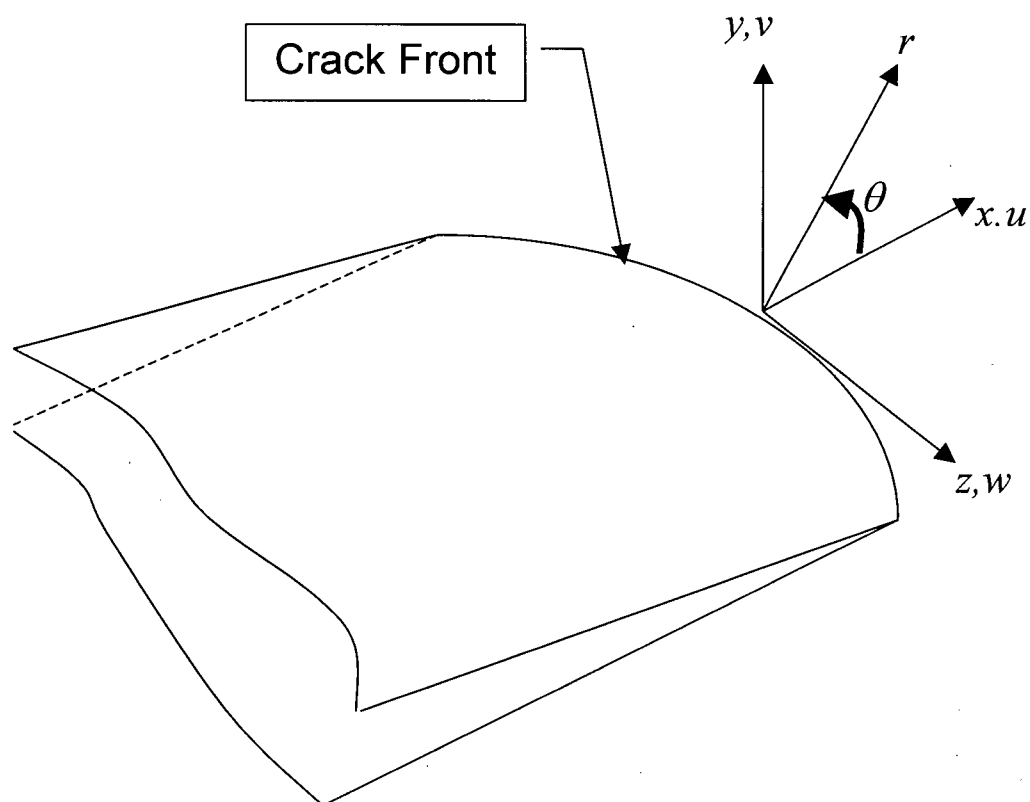
Figure 14: Local Coordinates Measured from a 3D Crack Front
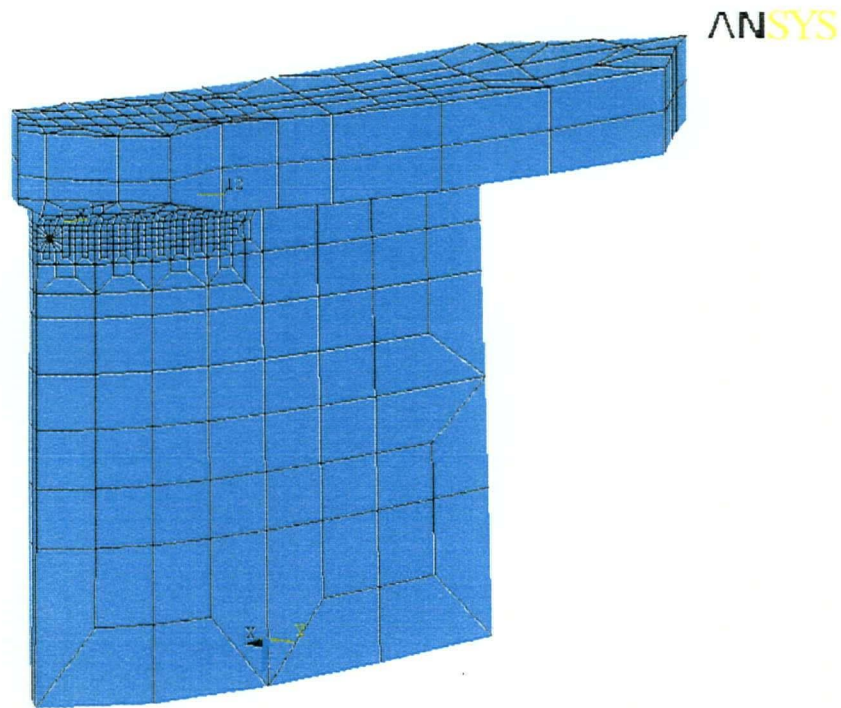
Figure 15: Solid FE Model
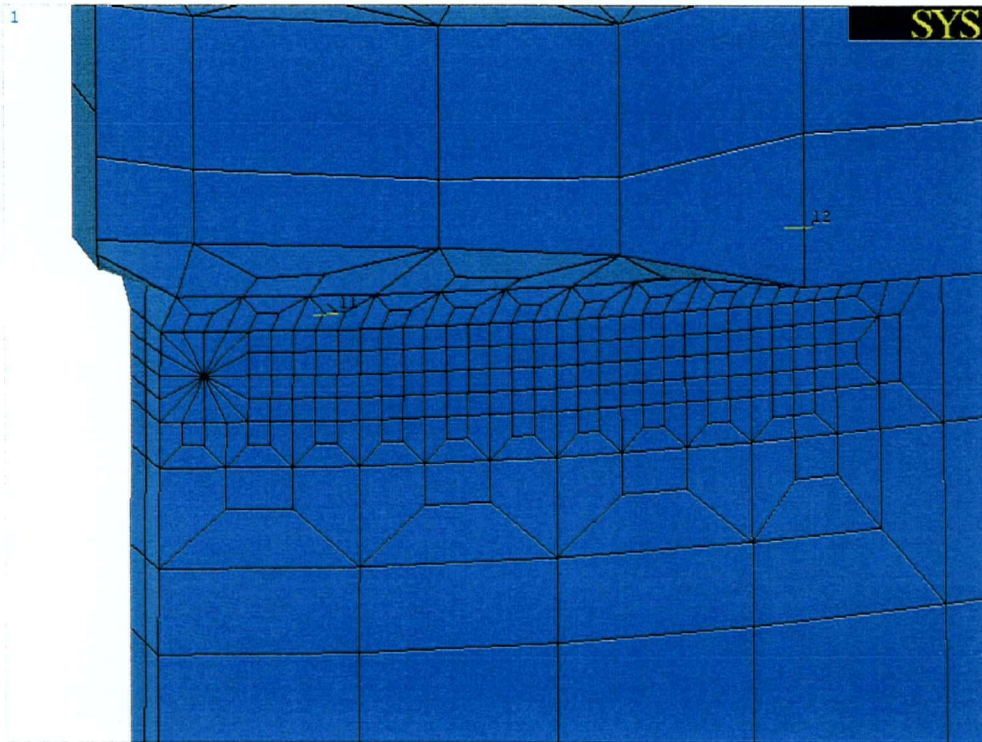
Figure 16: Fine Meshed Solid Band for Crack Extension
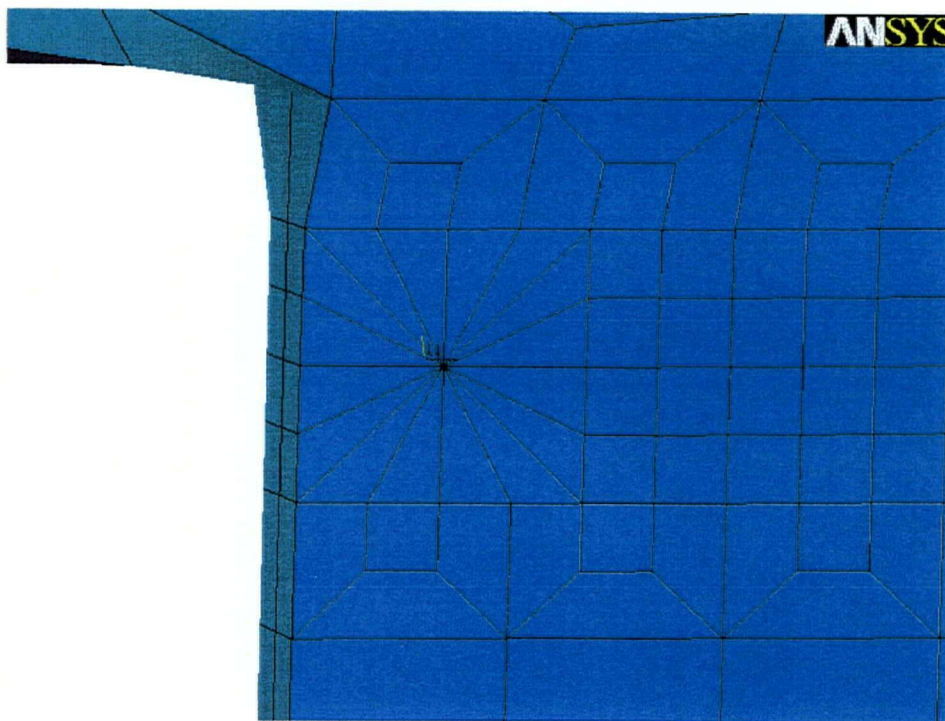
Figure 17 Crack Tip Wedge Element
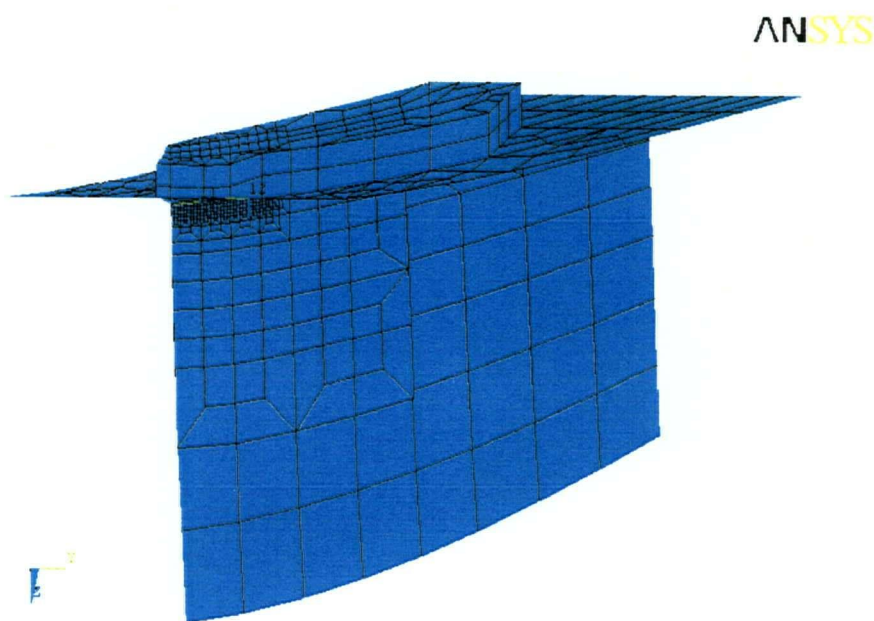
Figure 18: Full Solid-Shell Model
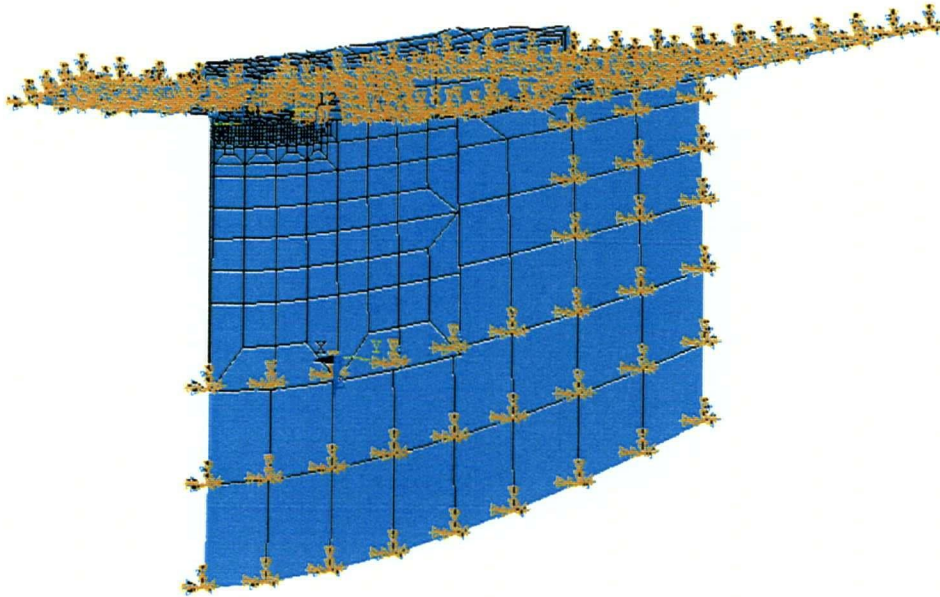
Figure 19: Full Solid Shell Model with Boundary Conditions Applied
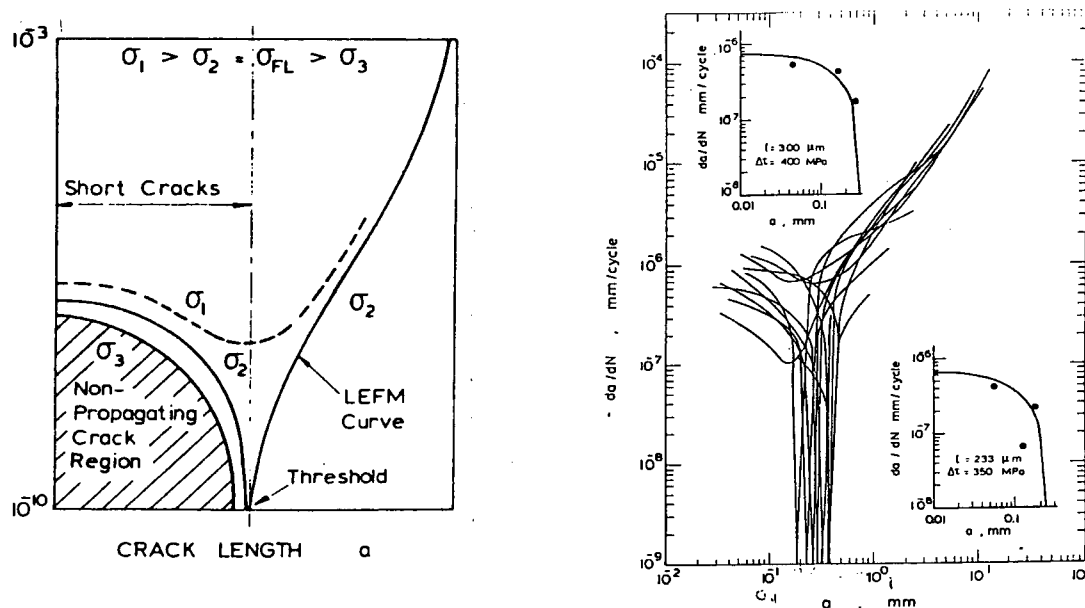
Figure 20: Experimental and Theoretical Fatigue Crack Growth Rates for Both Short and Long Cracks
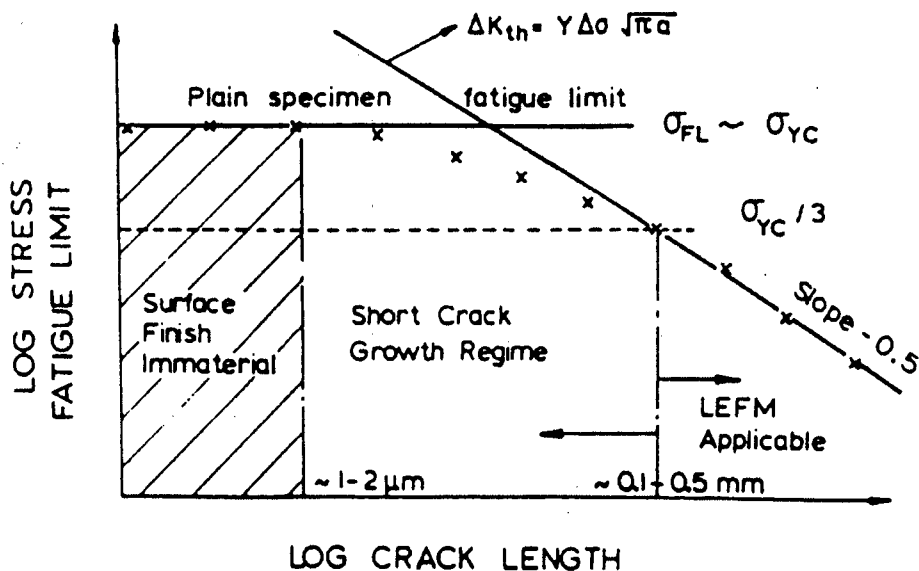
Figure 21: Bounding Conditions for Fatigue Limits of Materials Containing Short and Long Cracks
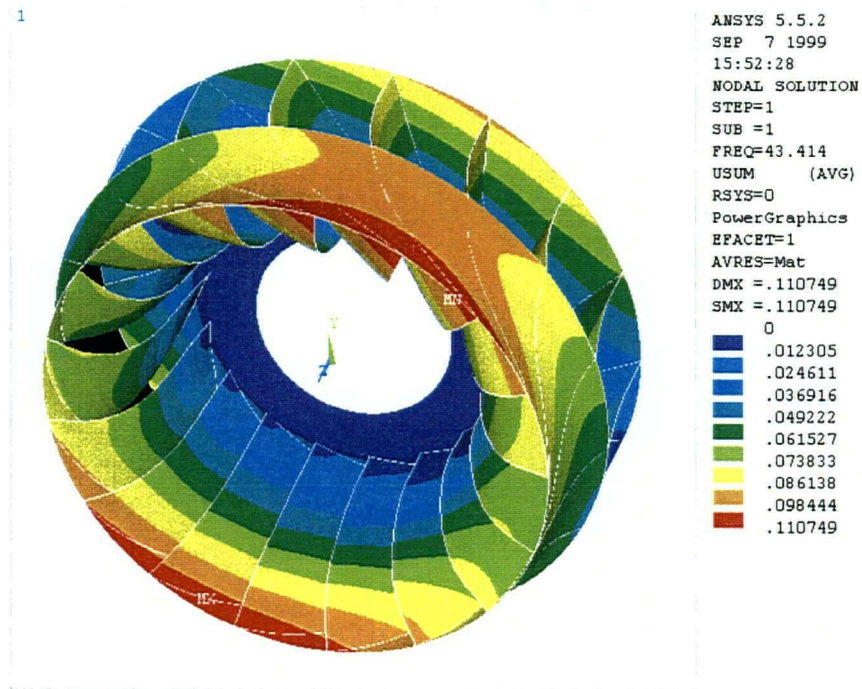
Figure 22: Modal Analysis Deformation Contour Plot: Mode-1 (Swing)
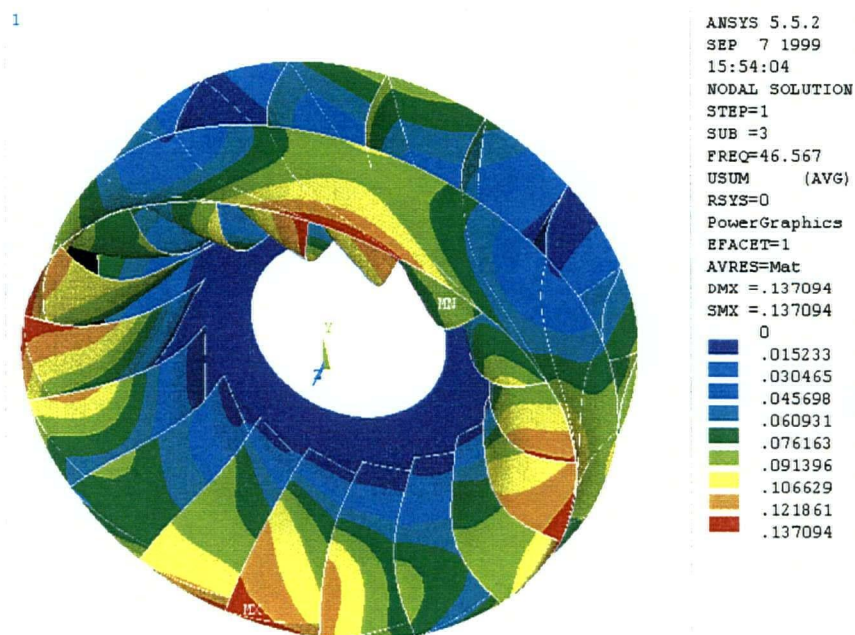
Figure 23: Modal Analysis Deformation Contour Plot: Mode-3 (2N Elliptical)

73

ANSYS 5.5.2
SEP 7 1999
15:55:18
NODAL SOLUTION
STEP=1
SUB =5
FREQ=58.47
USUM   (AVG)
RSYS=0
PowerGraphics
EFACET=1
AVRES=Mat
DMX =.092558
SMX =.092558

```
    0
    .010284
    .020568
    .030853
    .041137
    .051421
    .061705
    .07199
    .082274
    .092558
```
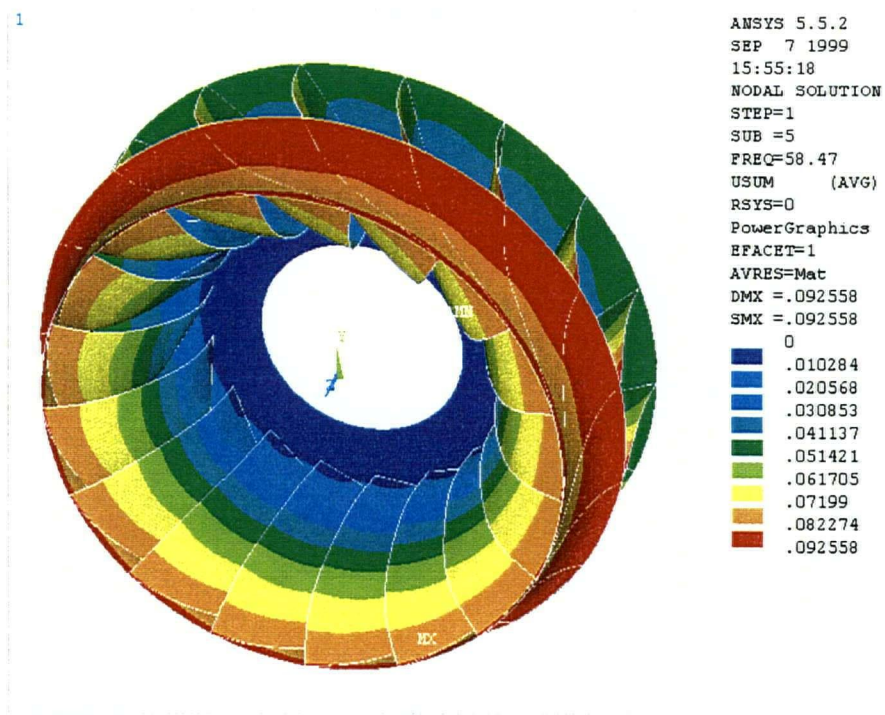
Figure 24: Modal Analysis Deformation Contour Plot: Mode-5 (1st Rotational)

ANSYS 5.5.2
SEP 7 1999
15:57:08
NODAL SOLUTION
STEP=1
SUB =6
FREQ=87.955
USUM   (AVG)
RSYS=0
PowerGraphics
EFACET=1
AVRES=Mat
DMX =.173673
SMX =.173673

```
    0
    .019297
    .038594
    .057891
    .077188
    .096485
    .115782
    .135079
    .154376
    .173673
```
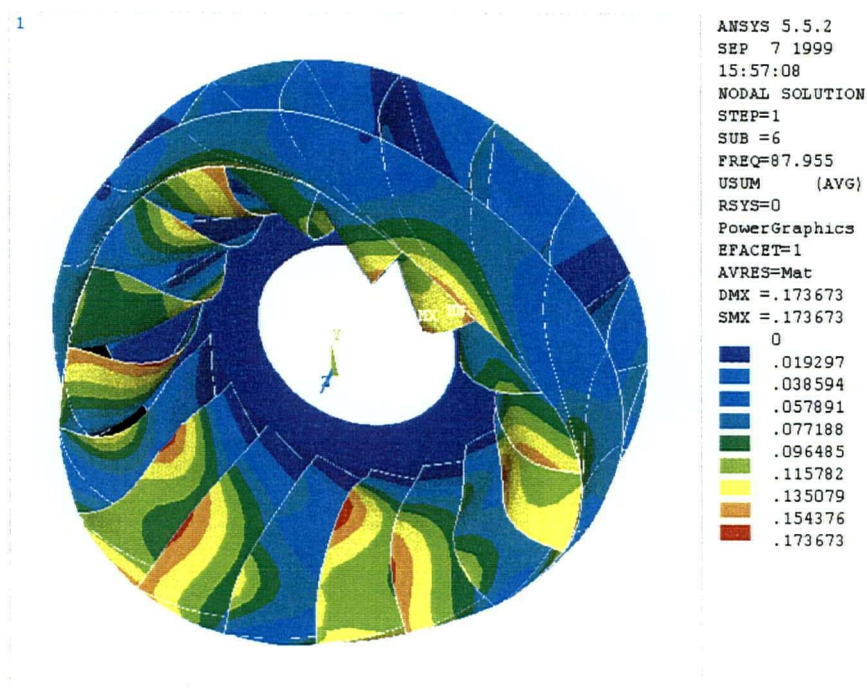
Figure 25: Modal Analysis Deformation Contour Plot: Mode-6 (3N Triangular)

ANSYS 5.5.2
SEP 7 1999
15:58:17
NODAL SOLUTION
STEP=1
SUB =8
FREQ=100.119
USUM   (AVG)
RSYS=0
PowerGraphics
EFACET=1
AVRES=Mat
DMX =.107333
SMX =.107333
      0
      .011926
      .023852
      .035778
      .047704
      .05963
      .071556
      .083482
      .095407
      .107333
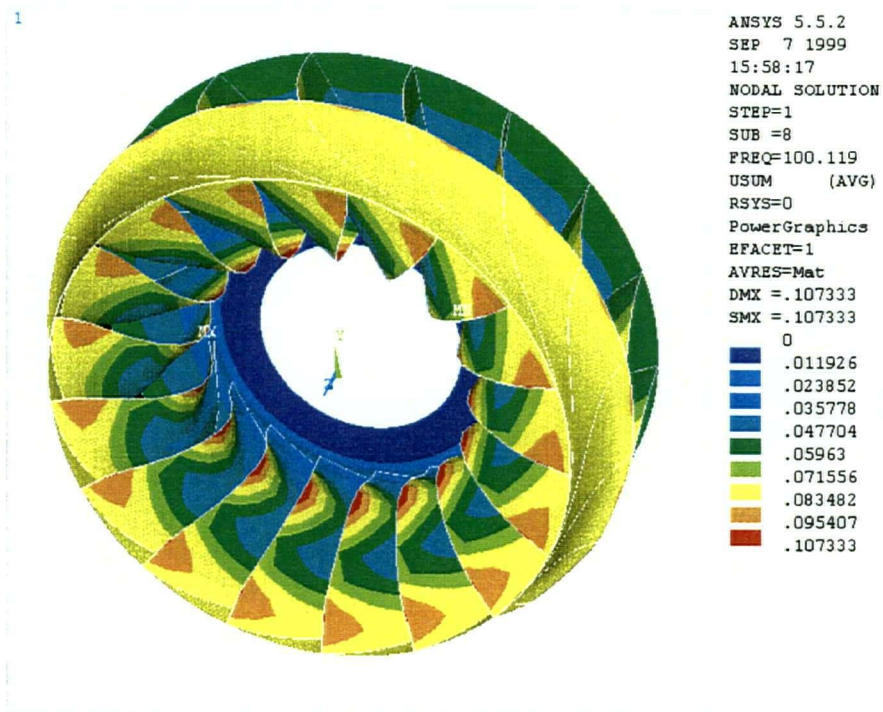
Figure 26: Modal Analysis Deformation Contour Plot: Mode-8 (2ⁿᵈ Rotational)

ANSYS 5.5.2
SEP 7 1999
15:59:34
NODAL SOLUTION
STEP=1
SUB =9
FREQ=115.58
USUM   (AVG)
RSYS=0
PowerGraphics
EFACET=1
AVRES=Mat
DMX =.235199
SMX =.235199
      0
      .026133
      .052266
      .0784
      .104533
      .130666
      .156799
      .182933
      .209066
      .235199
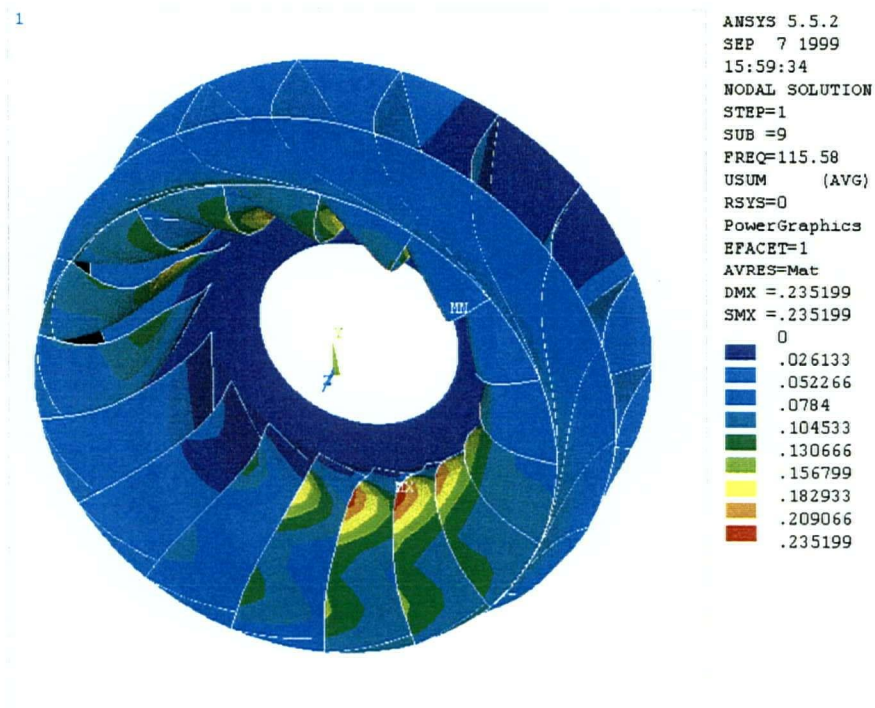
Figure 27: Modal Analysis Deformation Contour Plot: Mode-9 (Translational)

75

ANSYS 5.5.2
SEP 7 1999
16:00:42
NODAL SOLUTION
STEP=1
SUB =11
FREQ=124.093
USUM   (AVG)
RSYS=0
PowerGraphics
EFACET=1
AVRES=Mat
DMX =.258526
SMX =.258526
       0
       .028725
       .05745
       .086175
       .1149
       .143625
       .172351
       .201076
       .229801
       .258526
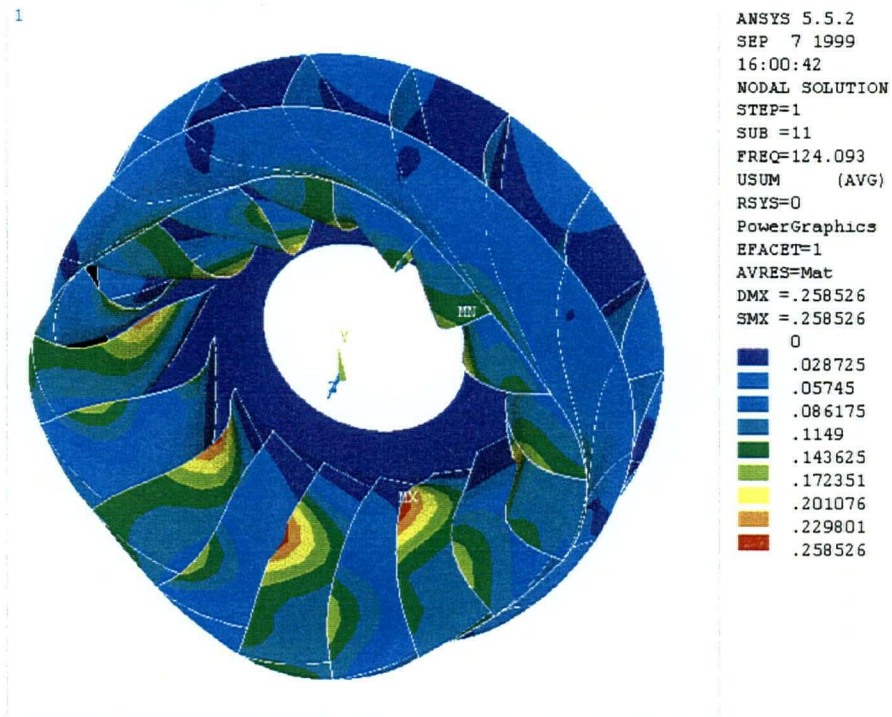
Figure 28: Modal Analysis Deformation Contour Plot: Mode-11 (4N Square)

ANSYS 5.5.2
SEP 7 1999
16:01:42
NODAL SOLUTION
STEP=1
SUB =13
FREQ=140.31
USUM   (AVG)
RSYS=0
PowerGraphics
EFACET=1
AVRES=Mat
DMX =.28641
SMX =.28641
       0
       .031823
       .063647
       .09547
       .127293
       .159117
       .19094
       .222764
       .254587
       .28641
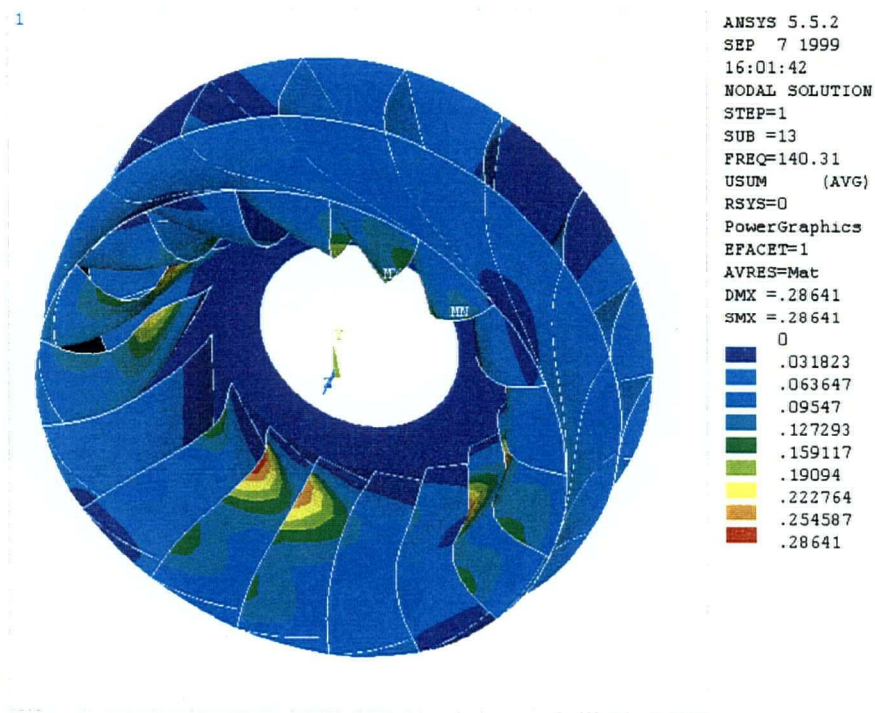
Figure 29: Modal Analysis Deformation Contour Plot: Mode 13 (Crown Bending)

76
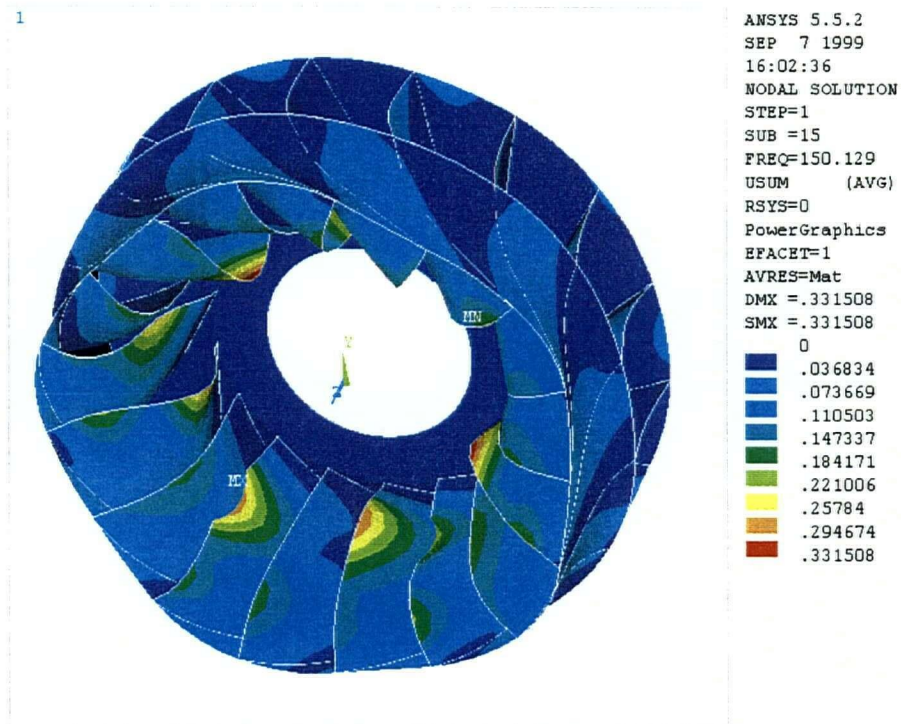
Figure 30: Modal Analysis Deformation Contour Plot: Mode-15 (5N Pentagonal)
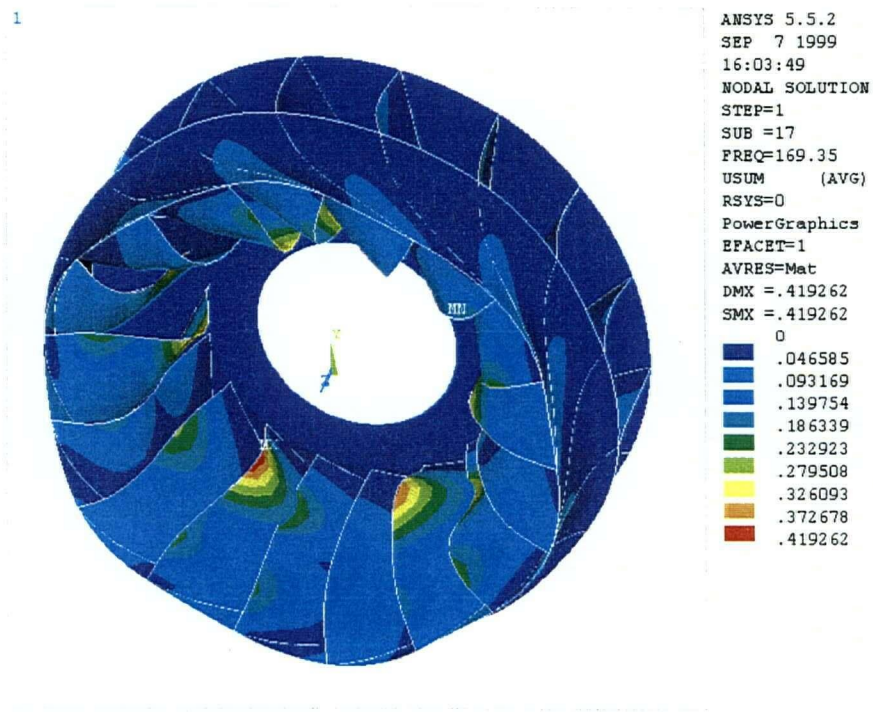
Figure 31: Modal Analysis Deformation Contour Plot: Mode-17 (6N Hexagonal)

ANSYS 5.5.2
SEP 7 1999
16:14:24
NODAL SOLUTION
STEP=1
SUB =5
FREQ=58.47
SEQV   (AVG)
PowerGraphics
EFACET=1
AVRES=Mat
DMX =.092558
SMN =336.722
SMX =28254
336.722
3439
6541
9643
12745
15847
18948
22050
25152
28254
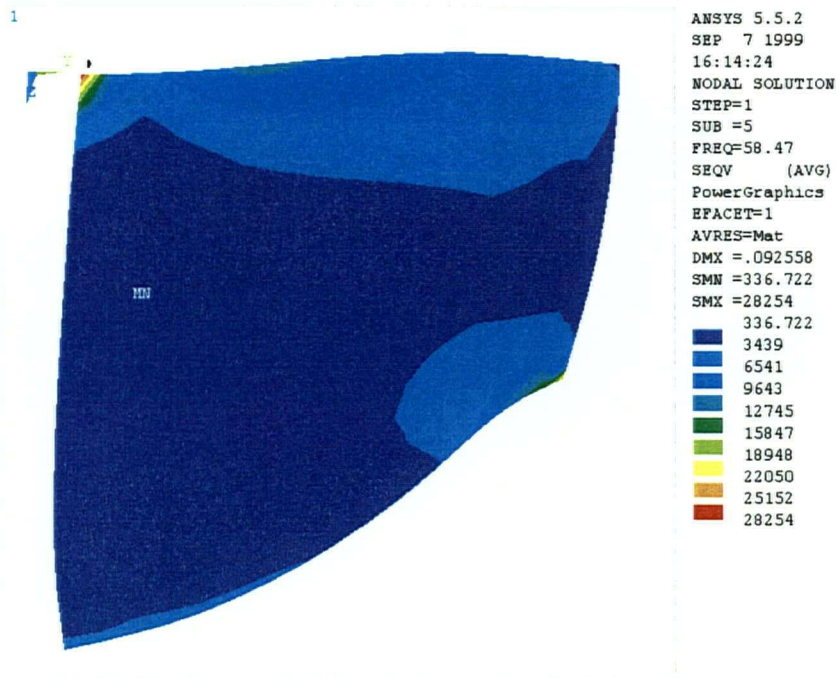
Figure 32: Relative Stress Contour of Blade in Mode 5[9]

ANSYS 5.5.2
SEP 8 1999
01:07:06
ELEMENTS
PowerGraphics
EFACET=1

XV =.82855
YV =-.110402
ZV =-.548923
DIST=42.073
XF =77.326
YF =33.09
ZF =-2.863
A-ZS=93.037
Z-BUFFER
PRES
-21.066
1.745
24.556
47.368
70.179
92.99
115.801
138.613
161.424
184.235
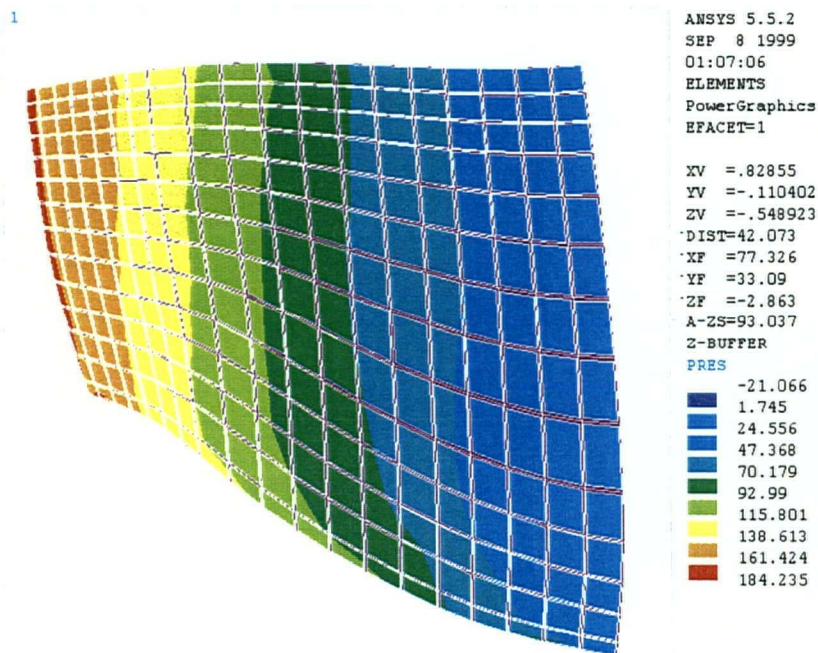
Figure 33: Pressure Distribution Contour of Blade

[9] All Stress Contour Plot's units are in psi.

ANSYS 5.5.2
SEP 7 1999
17:15:28
NODAL SOLUTION
STEP=1
SUB =1
FREQ=42.5
SEQV   (AVG)
PowerGraphics
EFACET=1
AVRES=Mat
DMX =.120989
SMN =844.791
SMX =46483
        844.791
        5916
        10987
        16057
        21128
        26199
        31270
        36341
        41412
        46483
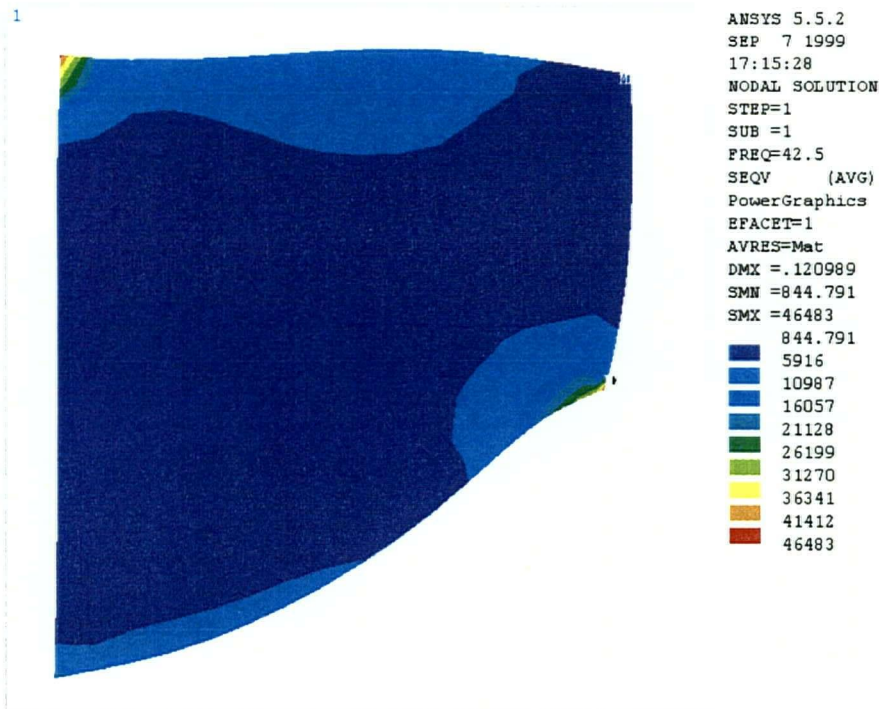
Figure 34: von Mises Stress Result of HR Analysis @ 42.5 Hz

ANSYS 5.5.2
SEP 7 1999
17:18:49
NODAL SOLUTION
STEP=1
SUB =1
FREQ=60
SEQV   (AVG)
PowerGraphics
EFACET=1
AVRES=Mat
DMX =1.055
SMN =3028
SMX =314857
        3028
        37676
        72324
        106971
        141619
        176267
        210914
        245562
        280209
        314857
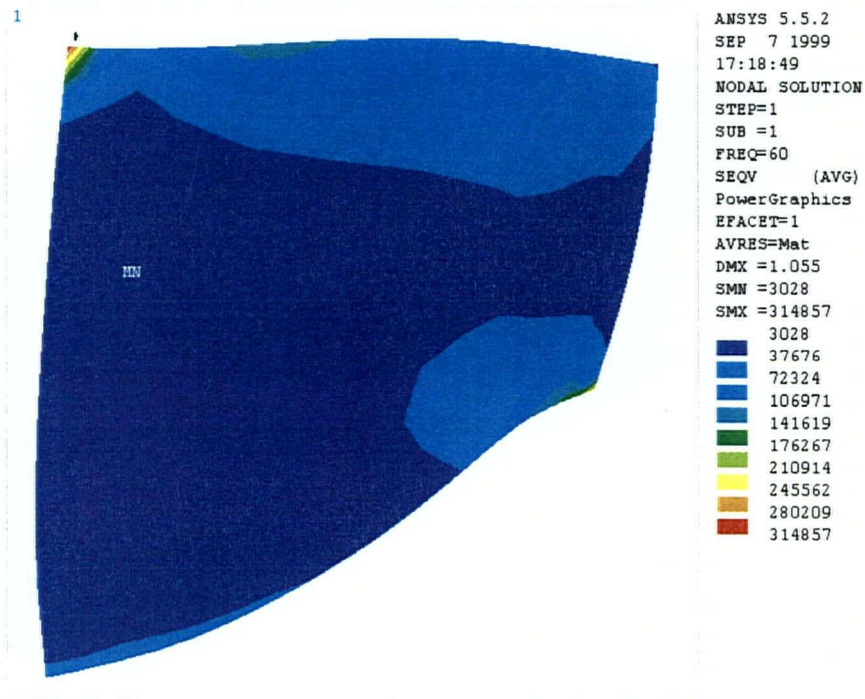
Figure 35: von Mises Stress Result of HR Analysis @ 60 Hz

79

ANSYS 5.5.2
SEP 7 1999
17:20:13
NODAL SOLUTION
STEP=1
SUB =1
FREQ=85
SEQV   (AVG)
PowerGraphics
EFACET=1
AVRES=Mat
DMX =.061942
SMN =314.704
SMX =13541
       314.704
       1784
       3254
       4724
       6193
       7663
       9132
       10602
       12072
       13541
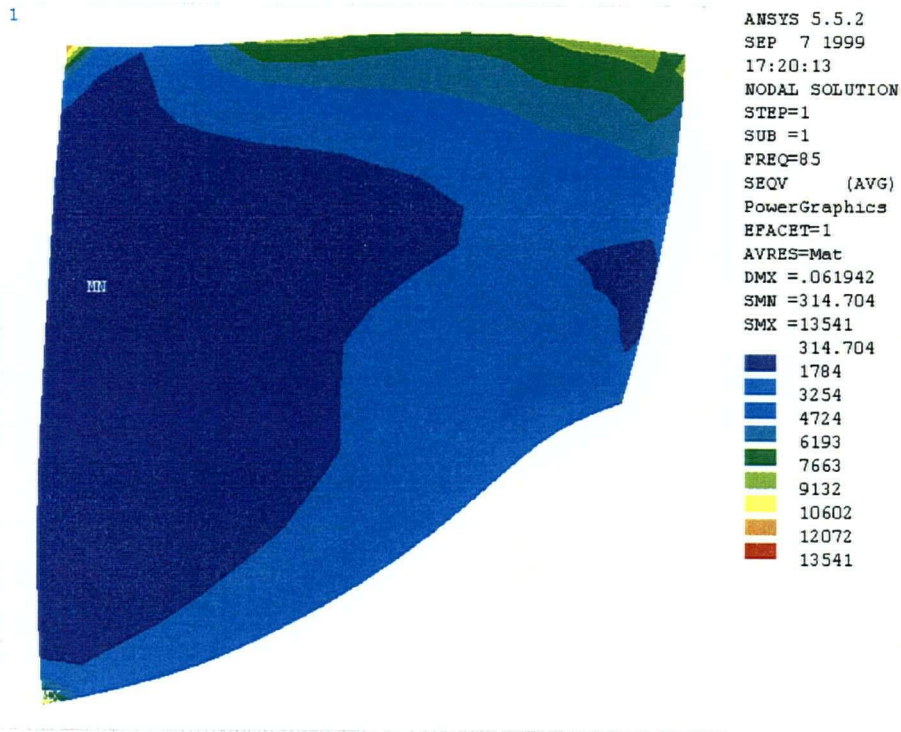
Figure 36: von Mises Stress Result of HR Analysis @ 85 Hz

ANSYS 5.5.2
SEP 7 1999
17:24:39
NODAL SOLUTION
STEP=1
SUB =1
FREQ=120
SEQV   (AVG)
PowerGraphics
EFACET=1
AVRES=Mat
DMX =.059863
SMN =173.668
SMX =24424
       173.668
       2868
       5563
       8257
       10952
       13646
       16341
       19035
       21730
       24424
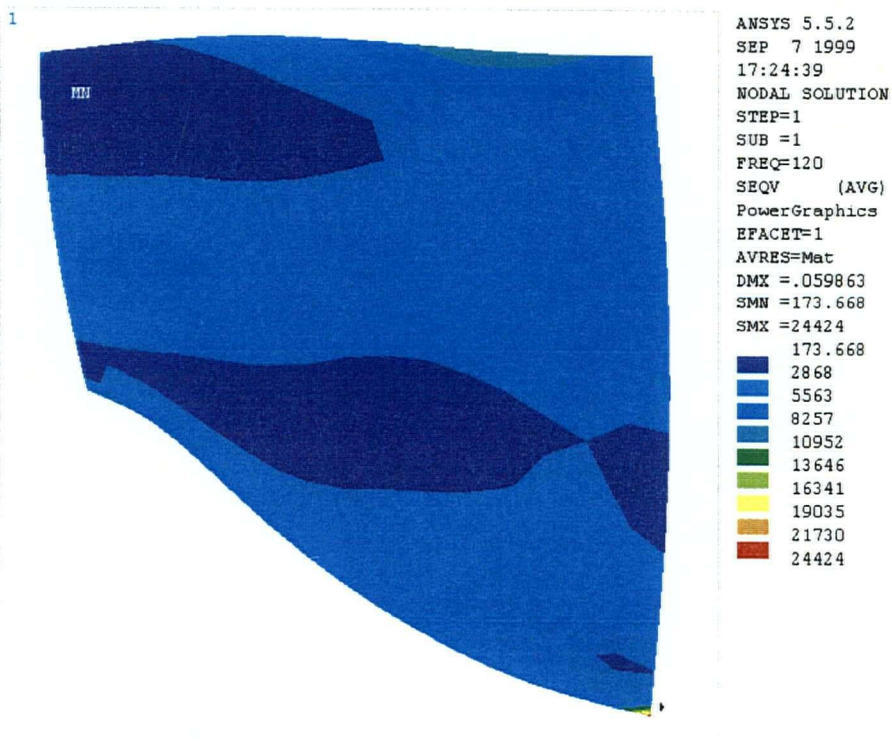
Figure 37: von Mises Stress Result of HR Analysis @ 120 Hz

80

ANSYS 5.5.2
SEP 7 1999
17:25:40
NODAL SOLUTION
STEP=1
SUB =1
FREQ=127.5
SEQV   (AVG)
PowerGraphics
EFACET=1
AVRES=Mat
DMX =.064062
SMN =203.657
SMX =27253
203.657
3209
6215
9220
12226
15231
18237
21242
24248
27253
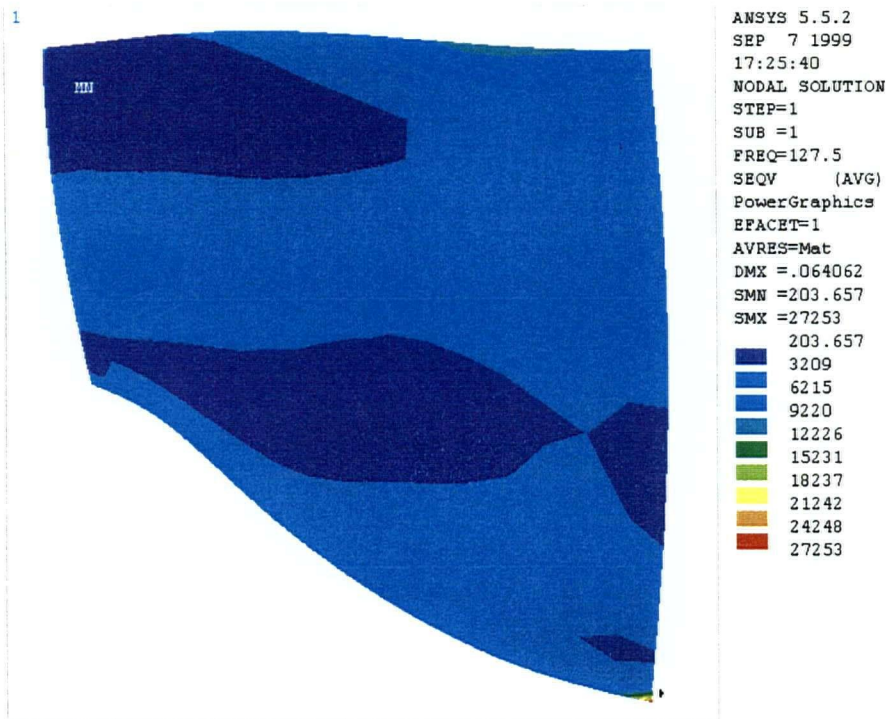
Figure 38: von Mises Stress Result of HR Analysis @ 127.5 Hz

ANSYS 5.5.2
SEP 7 1999
17:26:55
NODAL SOLUTION
STEP=1
SUB =1
FREQ=170
SEQV   (AVG)
PowerGraphics
EFACET=1
AVRES=Mat
DMX =3.932
SMN =4911
SMX =.103E+07
4911
119146
233380
347615
461849
576084
690318
804553
918787
.103E+07
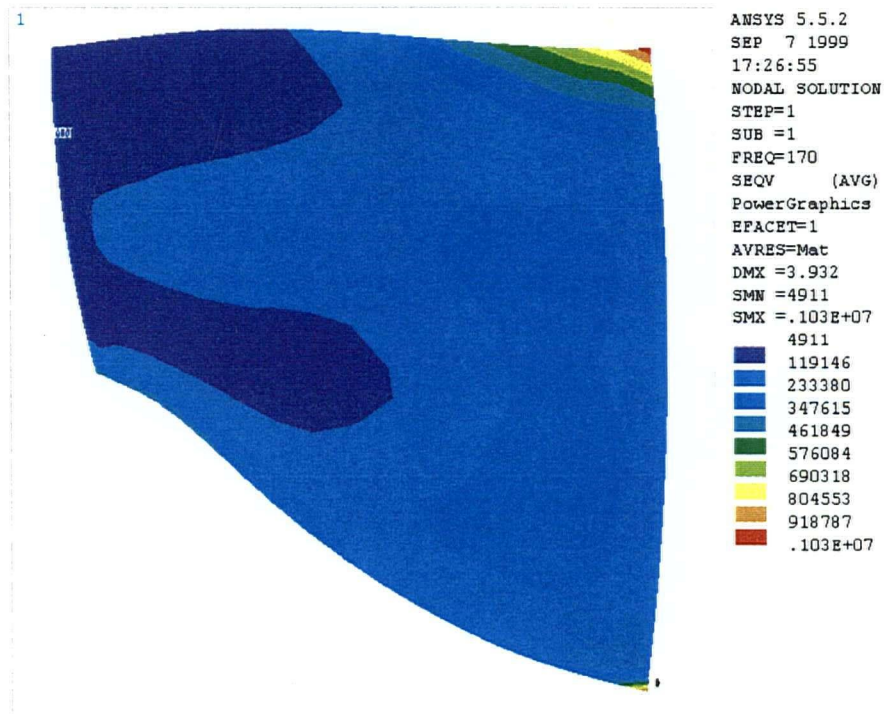
Figure 39: von Mises Stress Result of HR Analysis @ 170 Hz

81

ANSYS 5.5.2
SEP 7 1999
17:27:58
NODAL SOLUTION
STEP=1
SUB =1
FREQ=180
SEQV   (AVG)
PowerGraphics
EFACET=1
AVRES=Mat
DMX =.33761
SMN =433.899
SMX =106542
    433.899
    12224
    24013
    35803
    47593
    59383
    71173
    82962
    94752
    106542
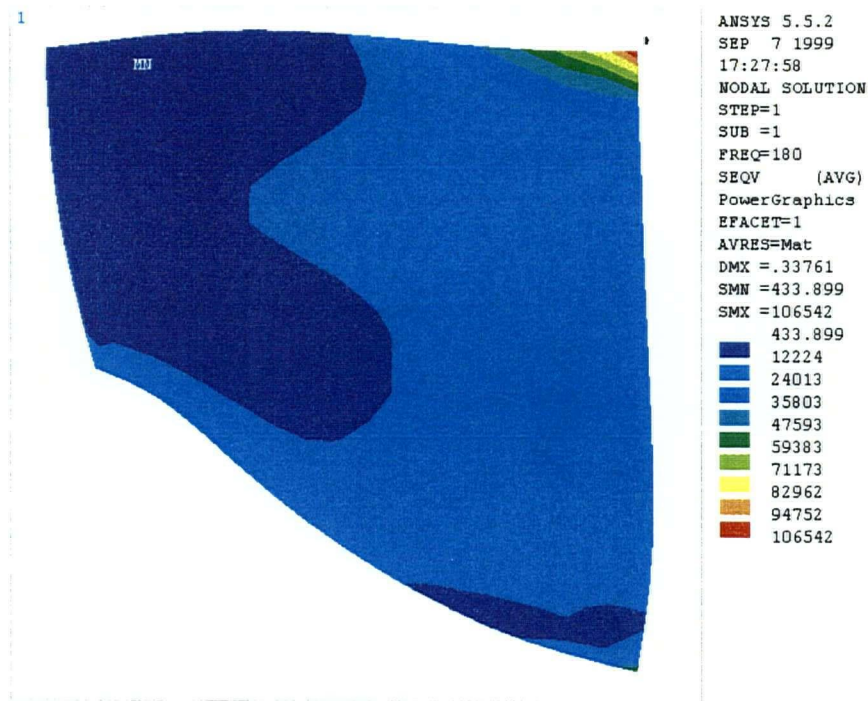
Figure 40: von Mises Stress Result of HR Analysis @ 180 Hz

ANSYS 5.5.2
SEP 7 1999
16:23:47
NODAL SOLUTION
STEP=1
SUB =5
FREQ=58.47
USUM   (AVG)
RSYS=0
PowerGraphics
EFACET=1
AVRES=Mat
DMX =.092558
SMN =.005498
SMX =.092558
    .005498
    .015171
    .024845
    .034518
    .044191
    .053865
    .063538
    .073211
    .082885
    .092558
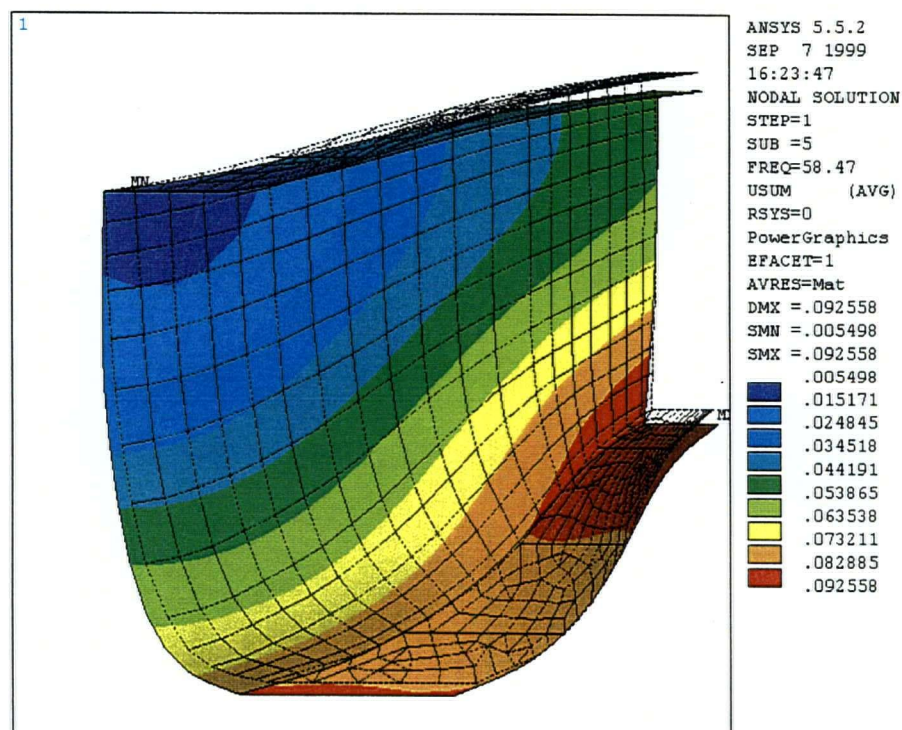
Figure 41: Deformation of Turbine Blade at Mode 5 (58.5 Hz)
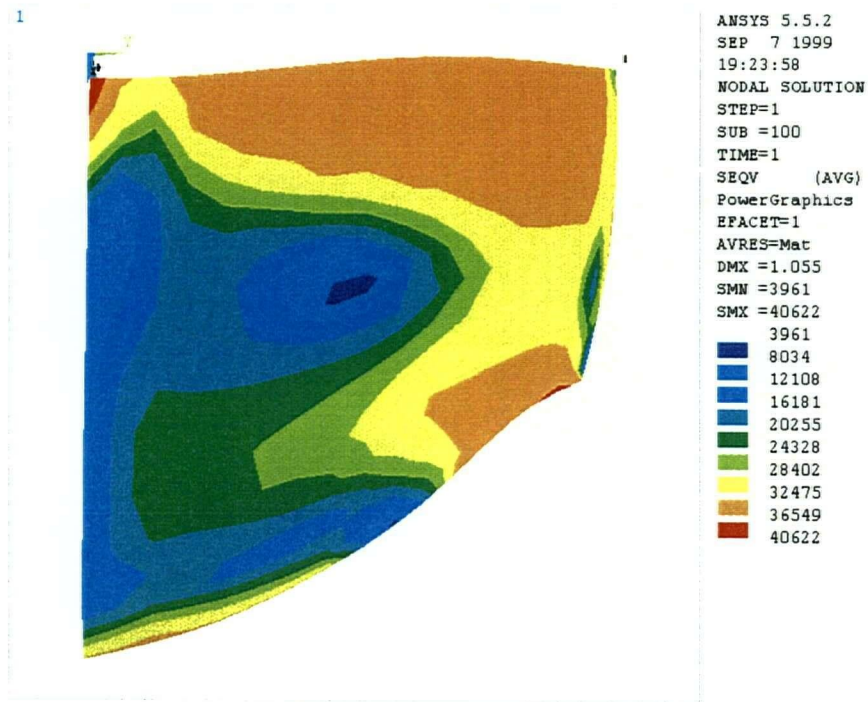
Figure 42: Nonlinear Static Analysis using HR Displacement Result @ 60 Hz
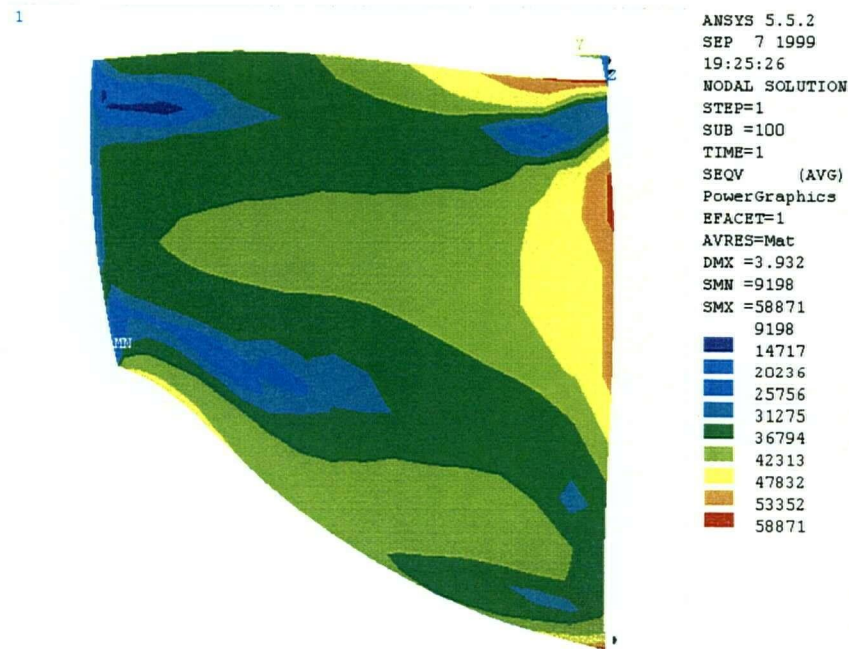
Figure 43: Nonlinear Static Analysis using HR Displacement Result @ 180 Hz

ANSYS 5.5.2
SEP 8 1999
13:38:44
NODAL SOLUTION
STEP=1
SUB =1
TIME=1
SEQV   (AVG)
PowerGraphics
EFACET=1
AVRES=Mat
DMX =.089439
SMN =648.907
SMX =31118
    648.907
    4034
    7420
    10805
    14191
    17576
    20962
    24347
    27733
    31118
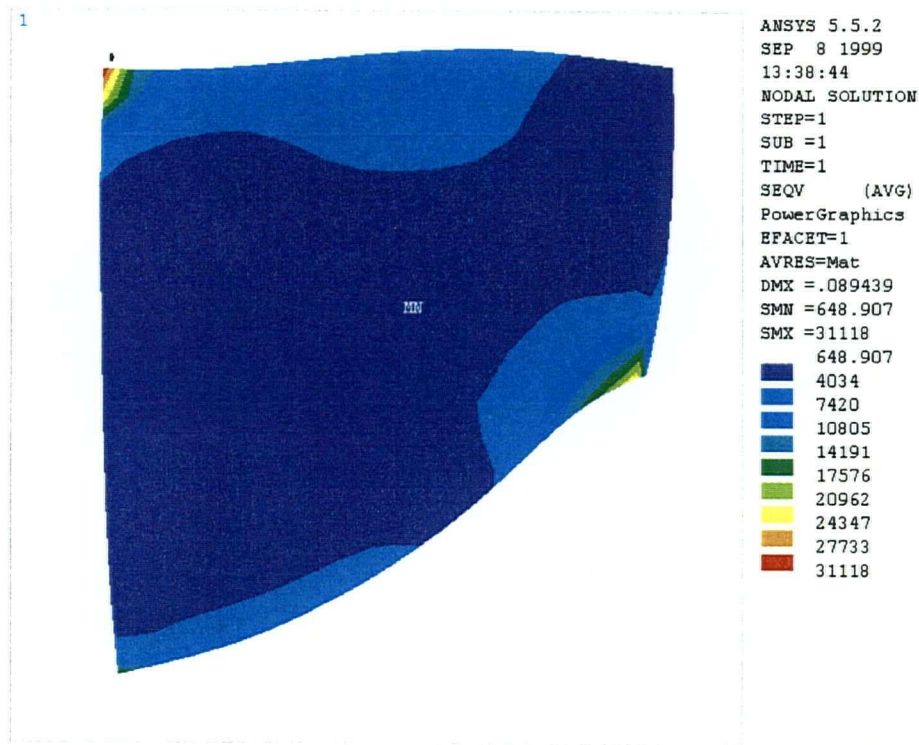
Figure 44: Stress Contour Result using Displacement Superposition @ 2.5% HR

ANSYS 5.5.2
SEP 8 1999
13:41:15
NODAL SOLUTION
STEP=1
SUB =1
TIME=1
SEQV   (AVG)
PowerGraphics
EFACET=1
AVRES=Mat
DMX =.122374
SMN =887.784
SMX =33340
    887.784
    4494
    8099
    11705
    15311
    18917
    22522
    26128
    29734
    33340
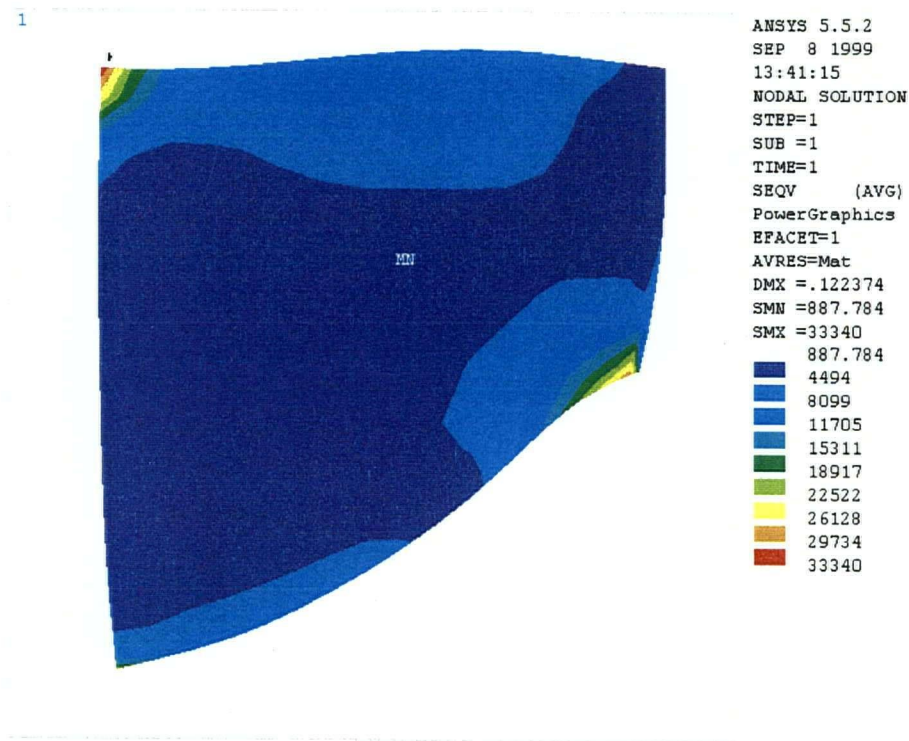
Figure 45: Stress Contour Result using Displacement Superposition @ 5% HR

84
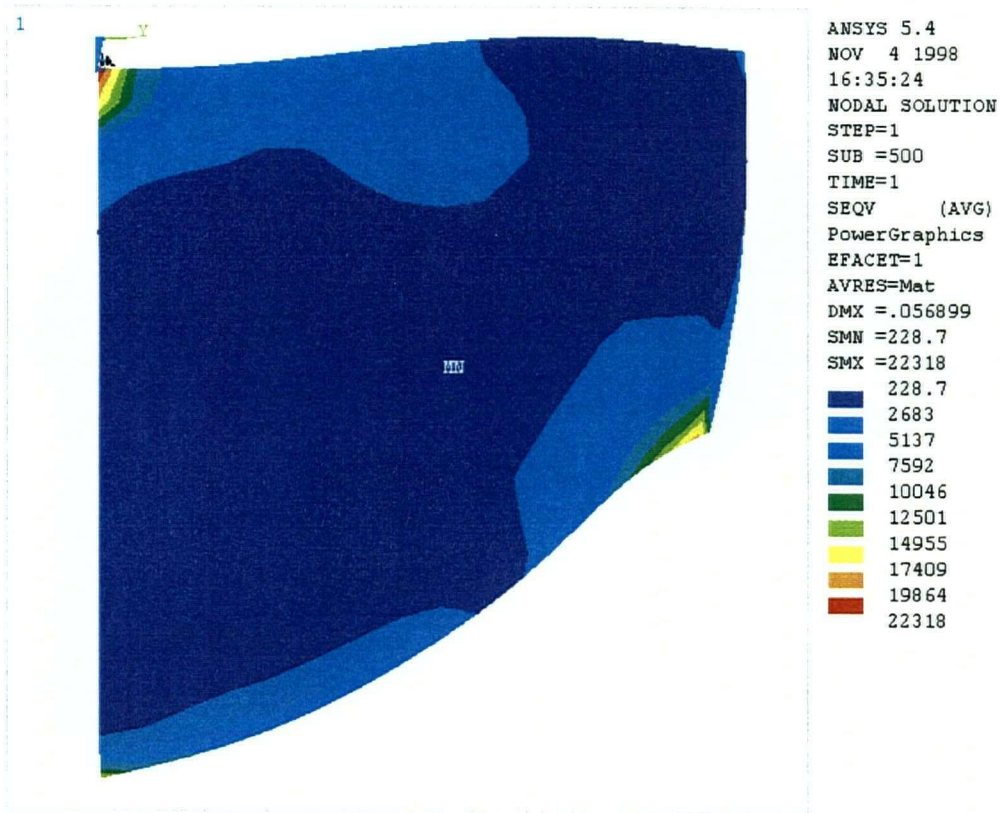
Figure 46: Static Analysis Result using 100% CFD pressure on Blade

ΔK vs a @ HR 0.025 + Static 0.975
(Range of Stress Intensity Factor vs Crack Length)
[Plain Strain]
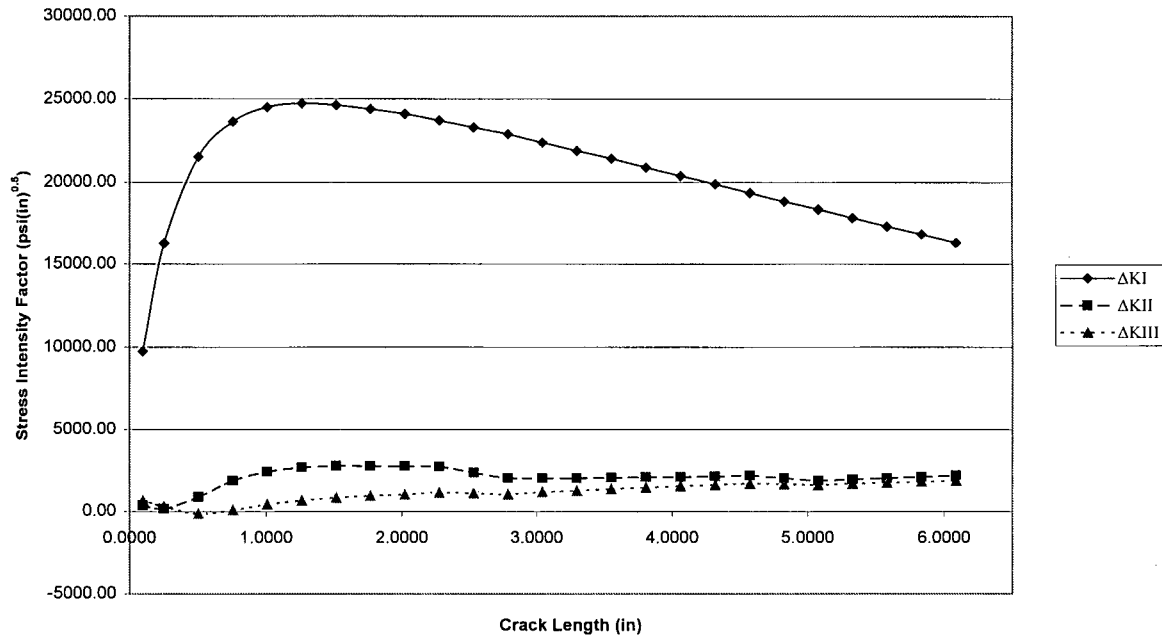
Figure 47: SIF Range versus Crack Length @ 2.5%HR Loading Case (Plain strain)

ΔK vs a @HR 0.05 + Static 0.95
(Range of Stress Intensity Factor vs Crack Length)
[Plain Strain]
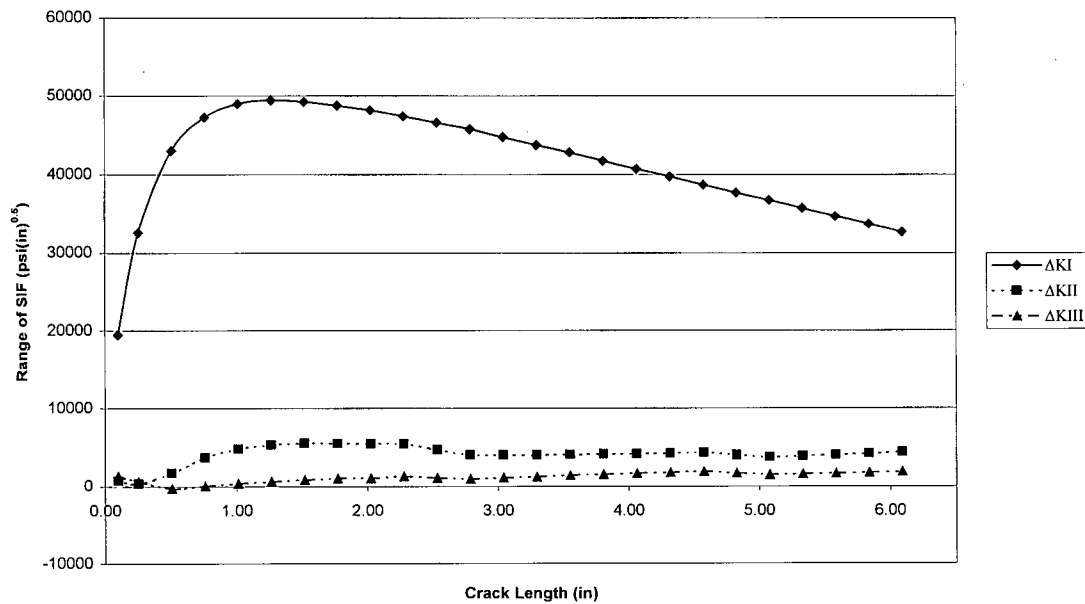
Figure 48: SIF Range versus Crack Length @ 5%HR Loading Case (Plain strain)
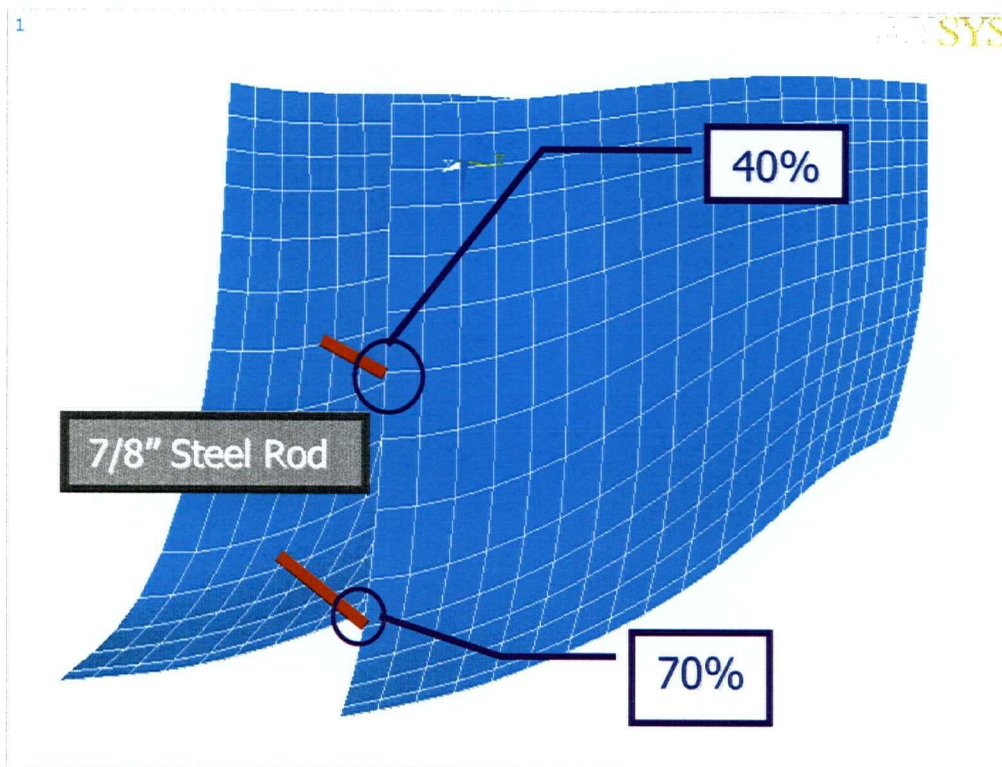
Figure 49: Configuration of Stress Stiffener on Turbine
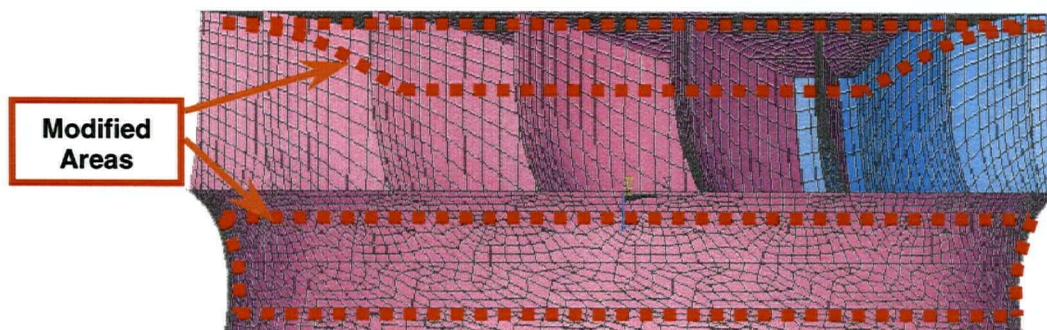
Figure 50: Areas of Thickness Modifications (Side View of Turbine)

Table 1: Results of Residual Stress Measurements at GMS

Test	Unit	Blade	Edge	Side	σ_{max} (MPa)	σ_{min} (MPa)	Comments
1	2	7	T	S	151.7	41.4	
2	2	7	T	S	124.1	62.1	Repeat Test 1
3	2	11	T	S	48.3	-34.5	No cracks, No repair
4	2	Band Between 11 & 12			-206.8	-110.3	Through SS overlay
5	3	13	T	S	Y+	Y+	
6	3	4	T	S	234.4	144.8	No cracks, No repair
7	3	16	L	P	Y+	206.8	
8	3	16	L	S	Y+	220.6	

Key:
T = Trailing Edge   P = Pressure Side
L = Leading Edge   Y+ = Stress Exceeds the Yield Point
S = Suction Side

Table 2: Technical Details and Results on Mitsubishi Model Tests

	Actual Turbine Runner	MHI Model Runner
Diameter of Runner (mm)	5137	357.8
Pressure Head (m)	165	40
Rotational Speed (RPM)	150	1062

Note: For Converting Model Test Data to Prototype Data refer to Appendix A

Table 3: Comparison of MHI Model Runner Test and BC Hydro Full Size Turbine Test

(MPa)	BC Hydro Turbine Test* (1975)	MHI Model Runner Test ** (1973)
Recorded Stress	31.7 – 91.6	9.8 - 66.9 a
Fluctuating Stress	2.8 – 10.3	10.3

*   Stress value was obtained from strain gage measurement while the runner was slowly accelerated to the maximum loading. Range of mean stress was recorded.
** Stress values for the MHI Model Runner Test were scaled to compare with actual stress measured on turbine stress.

Table 4: Holographic Test Results (Reference [9]) on Turbine Model, UBC, 1975

Table 4(a): First Six Resonant Frequencies

	1	2	3	4	5	6
Freq. (Hz)	493-496	946-950	1346-1348	1612-1619	1730-1734	1786-1797
Mode Shape	2-N	3-N	4-N	-	-	-

N = Nodal Diameter

Table 4(b): Natural Frequency Shift of Fully Submerged Turbine Model

Resonant Frequencies (Hz)		Percent Reduction Compared to Dry Data
Dry	Wet	
494	413	16.4
947	708	25.2
1347	860	36.2

Table 5: Comparison of Modal Data before and after stiffener installation on Unit 4 runner.

Mode No.	Blade Mode* Before Blade Stiffeners (Hz)	Blade Modes After Blade Stiffeners (Hz)	Band Modes* Before Blade Stiffeners (Hz)	Band Modes After Blade Stiffeners (Hz)
1	44.22	47.06	43.58	48.88
2	90.83	100.39	90.69	104.55
3	127.32	144.53	127.60	149.78
4	135.18	148.85	152.93	180.56
5	153.8	-	170.77	-
6	171.8	-	185.51	-
7	182.5	179.02	211.3	-
8	218.3	222.46	-	-
9	234.5	-	-	-

*Experimental resonant frequencies of the same mode shape are different when measured on blade and measured on band. Therefore, two sets of data were collected. Since the Band Mode provides more definite mode shapes and repeatability, it would be used for comparison purpose.

Table 6: Rotational Speed Related Frequencies of Excitation (up to 180 Hz)

Multiple of	Speed (2.5 Hz) × Wicket Gates (24)	Speed (2.5 Hz) × Blades (17)	Excitation Frequency (Hz)
×1	60.0	42.5	42.5
			60.0
×2	120.0	85.0	85.0
			120.0
×3	180.0	127.5	127.5
			170.0
×4	-	170.0	180.0

Table 7: Modal Analysis Results (25 Modes)

Mode	Frequency (Hz)	Mode Shape Description
1	43.37	Swinging:
2	43.37	The whole turbine swing about center of crown
3	46.40	2N (Nodal Diameter = 2: Elliptical)
4	46.40	Band exhibits elliptical shape
5	58.42	1st Rotational: Band Rotates wrt Crown (Half Sine Wave)
6	87.79	3N (Nodal Diameter = 3: Triangular)
7	87.79	Band exhibits triangular shape
8	100.12	2nd Rotational: Band Rotates wrt Crown (One Sine Wave)
9	115.59	Translational:
10	115.59	Band moves sideways wrt Crown
11	123.95	4N (Nodal Diameter = 4: Square)
12	123.95	Band exhibits square shape
13	140.30	Crown Bending:
14	140.30	Sides of crown bend downwards
15	150.02	5N (Nodal Diameter = 5: Pentagonal)
16	150.02	Band exhibits pentagonal shape
17	169.29	6N (Nodal Diameter = 6: Hexagonal)
18	169.29	Band exhibits hexagonal shape
19	170.73	Not clear (Possibly 3rd Rotational)
20	177.06	Group blade movement
21	177.06	(No specific pattern can be identified)
22	182.20	7N (Nodal Diameter = 7: Heptagonal)
23	182.20	Band exhibits heptagonal shape
24	188.48	Alternating blade moves
25	188.48	(No specific pattern can be identified)

Table 8: Natural Frequency Comparison: FE – Experimental results

(Frequency Measured from GMS turbine Unit #4)

Mode Shape	FE Frequency (Hz)	Frequency Measured from Blade (Hz)	% Error	Frequency Measured from Band (Hz)	% Error
2N Elliptical	46.40	44.22	+4.9	43.58	+6.5
3N Triangular	87.79	90.83	-3.3	90.69	-3.2
4N Square	123.95	127.32	-2.6	127.60	-2.9
5N Pentagonal	150.02	135.18	+11.0	152.93	-1.9

Table 9: High Stress Locations of Each Mode

Mode	Frequency (Hz)	Description	Side of Blade	High Stress Location* (using labeling of Figure 2)
1	43.37	Swing	S	A
2	43.37			
3	46.40	2N Elliptical	S	A+D
4	46.40			
5	58.42	1st Rotational	S	A+C
6	87.79	3N Triangular	S	D+A
7	87.79			
8	100.12	2nd Rotational	S	A
9	115.59	Translational	S	A
10	115.59			
11	123.95	4N Square	S	D
12	123.95			
13	140.30	Crown Bending	S	A
14	140.30			
15	150.02	5N Pentagonal	S	D
16	150.02			
17	169.29	6N Hexagonal	S	A
18	169.29			
19	170.73	-	P	A+D
20	177.06	Group Blade Movement	P	D
21	177.06			

S = suction side
P = pressure side
* Note: In the high stress location column, the first letter indicates the highest stress location, the second letter indicates the 2nd highest stress location.

Table 10: Ratio of Natural Frequencies of Full FE Model to 1:14 FE Model and Comparison to Reference [9]

Mode	Frequency (Hz)		Ratio (2) divided by (1)	Reference [9]* on 1:14 Turbine Model Freq. (Hz)	Error of FE Model According to Ref. [9] Results (%)
	Full FE Turbine Model (1)	FE Model of 1:14 Turbine Model (2)			
1	43.37	438.04	10.1	-	-
2					
3	46.40	468.64	10.1	493 - 496	-4.9 to −5.5
4					
5	58.42	590.04	10.1	-	-
6	87.79	886.68	10.1	946 - 950	-6.3 to −6.7
7					
8	100.12	1011.21	10.1	-	-
9	115.59	1167.46	10.1	-	-
10					
11	123.95	1251.90	10.1	1346 - 1348	-7.0 to −7.1
12					
13	140.30	1417.03	10.1	-	-
14					
15	150.02	1515.20	10.1	-	-
16					
17	169.29	1709.83	10.1	-	-
18					
19	170.73	1724.37	10.1	-	-
20	177.06	1788.31	10.1	-	-
21					
22	182.20	1840.22	10.1	-	-
23					
24	188.48	1903.65	10.1	-	-
25					

* Note: Reference [9] results were stated in ranges and therefore ranges of errors were computed. On the other hand, mode shapes of frequency higher than 1348 Hz were not identifiable, thus comparison was not made.

Table 11: Effect of Spin Softening and Stress Stiffening on Natural Frequencies

Mode	No Effect Frequency (Hz)	Spinning plus Gravity		Spinning plus Gravity and Pressure	
		Freq (Hz)	Changes (%)	Freq (Hz)	Changes (%)
1	43.37	43.38	+0.02	43.41	+0.09
2					
3	46.40	46.53	+0.03	46.57	+0.37
4					
5	58.42	58.43	+0.02	58.47	+0.08
6	87.79	87.93	+0.16	87.96	+0.19
7					
8	100.12	100.11	-0.01	100.12	+0.00
9	115.59	115.56	-0.03	115.58	-0.01
10					
11	123.95	124.07	+0.01	124.09	+0.11
12					
13	140.30	140.30	+0.00	140.31	+0.01
14					
15	150.02	150.11	+0.06	150.13	+0.07
16					
17	169.29	169.33	+0.02	169.35	+0.04
18					
19	170.73	170.66	-0.04	170.68	-0.03
20	177.06	177.08	+0.01	177.08	+0.01
21					

Table 12: Highest Stress and Its Location for Harmonic Response Analysis

No.	Excitation Frequency (Hz)	Max. Stress (MPa)	Max. Stress Location	2nd Max. Location
1	42.5	321	C (S)	A (S)
2	60.0	2172	A (S)	C (S)
3	85.0	93	D (P)	A (S)
4	120.0	168	D (P)	C (S)
5	127.5	188	D (P)	C (S)
6	170.0	7102	D (P)	A (P)
7	180.0	734	A (P)	D (P)

(S) = Suction Side   (P) = Pressure Side
Location based on labeling in Figure 2   Stress = Von Mises Stress

93

Table 13: Total Strain Range and Predicted Initiation Life

Loading Case	Max. Total Strain	Min. Total Strain	Total Strain Range	Predicted Initiation Life (cycles)	Predicted Initiation Life (Days)*
2.5% HR	0.11338E-2	0.48242E-3	6.5138E-4	2.062E+9	397.7
5% HR	0.13244E-2	0.12224E-3	1.2022E-3	2.362E+7	4.556

* Note that the number of days calculation based on 60 Hz oscillation assumption and the turbine is operating 24 hours a day, 365.25 days a year.

Table 14: Stress Intensity Factor Range of 2.5%HR and 5%HR loadings

Crack Length (m)	ΔK_I at 2.5%HR (MPa√m)		ΔK_I at 5%HR (MPa√m)	
	Plain Strain	Plain Stress	Plain Strain	Plain Stress
0.00250	10.71	9.74	21.42	19.49
0.00641	17.90	16.29	35.79	32.57
0.01282	23.64	21.52	47.29	43.03
0.01924	25.96	23.63	51.93	47.26
0.02566	26.92	24.49	53.84	48.99
0.03209	27.17	24.73	54.35	49.46
0.03852	27.06	24.62	54.12	49.25
0.04496	26.79	24.38	53.59	48.76
0.05141	26.48	24.10	52.96	48.20
0.05786	26.06	23.71	52.11	47.42
0.06431	25.60	23.30	51.20	46.59
0.07078	25.15	22.89	50.30	45.77
0.07724	24.60	22.38	49.19	44.76
0.08372	24.05	21.89	48.10	43.77
0.09020	23.54	21.42	47.08	42.84
0.09669	22.96	20.89	45.91	41.78
0.10319	22.38	20.37	44.77	40.74
0.10969	21.85	19.88	43.70	39.76
0.11620	21.26	19.35	42.53	38.70
0.12260	20.71	18.84	41.41	37.69
0.12901	20.19	18.37	40.38	36.75
0.13542	19.61	17.85	39.23	35.70
0.14184	19.05	17.34	38.10	34.67
0.14827	18.52	16.85	37.04	33.71
0.15470	17.94	16.32	35.87	32.64

Table 15: Total Fatigue Life Prediction Results

	2.5%HR Loading		5%HR Loading	
	Plain Strain	Plain Stress	Plain Strain	Plain Stress
Initiation Life (cycles)	2.06E+09	2.06E+09	2.36E+07	2.36E+07
Propagation Life (cycles)	1.16E+06	1.56E+06	1.26E+05	1.70E+05
Total Life (cycles)	2.06E+09	2.06E+09	2.37E+07	2.38E+07
Total Life (Days)	397.99	398.06	4.58	4.59

Table 16: Effect of Installation of 40-70 Blade Stiffeners

Mode Number	Frequency (Hz)					
	FE Model No Stiffeners	FE Model with Stiffeners	% change	Experimental Result	Experimental with Stiffeners	% change
1	43.37	43.74	+0.9	-	-	-
2						
3	46.40	49.01	+5.6	43.58	48.88	+12.2
4						
5	58.42	58.72	+0.52	-	-	-
6	87.79	98.56	+12.3	90.69	104.55	+15.4
7						
8	100.12	104.42	+4.3	-	-	-
9	115.59	121.44	+5.1	-	-	-
10						
11	123.95	144.47	+16.6	127.60	149.78	+17.4
12						
13	140.30	149.49	+6.6	-	-	-
14						
15	150.02	177.51	+18.3	152.93	180.56	+18.1
16						

Table 17: Effect of Thickness Modifications

Percentage change of Band Thickness* (%)	Percentage Change of Crown Thickness (%)	Percentage Change of Rotational Natural Frequency (%)
+40	-	-3.6
+20	-	-1.8
-26.3	-	+2.4
-55.7	-	+5.3
-	+40	+7.42
	+60	+9.80
-20	+20	+5.9
-40	+40	+11.2
-60	+60	+15.5

* Percentage Change of Band thickness refers to areas indicated in Figure 50.

Appendix A: Conversion Method from Model Test Data to Prototype Data

D = Diameter of runner   (m) ω = Angular Velocity   (rad/s)
N = Model Ratio = D_p/D_m f = frequency   (Hz)
                                        F = Centrifugal Force   (N)

H = Head Pressure   (m)   W = Weight   (N)
n = Rotational Speed   (RPM) σ = Stress   (MPa)
U = Peripheral Speed   (m/s) ρ = Specific weight   (kg/m^3)

Suffix   p: prototype   m: model

Dimensional Analysis:
(1) Peripheral speed of runner

$$\frac{U_p}{U_m} = \frac{\sqrt{H_p}}{\sqrt{H_m}} \tag{A1}$$

(2) Revolution

$$\frac{n_p}{n_m} = \frac{U_p \cdot D_m}{U_m \cdot D_p} = \frac{1}{N} \cdot \sqrt{\frac{H_p}{H_m}} \tag{A2}$$

(3) Centrifugal Force
Centrifugal Force due to runner's weight

$$\frac{F_p}{F_m} = \frac{W_p \cdot D_p}{W_m \cdot D_m} \cdot \left(\frac{\omega_p}{\omega_m}\right)^2 = \frac{\gamma_p}{\gamma_m} \cdot \left(\frac{D_p}{D_m}\right)^4 \cdot \left(\frac{n_p}{n_m}\right)^2 = N^2 \cdot \frac{\gamma_p \cdot H_p}{\gamma_m \cdot H_m} \tag{A3}$$

Centrifugal Force of Water

$$\frac{F_p}{F_m} = \frac{W_p \cdot D_p}{W_m \cdot D_m} \cdot \left(\frac{\omega_p}{\omega_m}\right)^2 = \left(\frac{D_p}{D_m}\right)^4 \cdot \left(\frac{n_p}{n_m}\right)^2 = N^2 \cdot \frac{H_p}{H_m} \tag{A4}$$

(4) Stress
Stress due to centrifugal force of runner

$$\frac{\sigma_p}{\sigma_m} = \frac{F_p \cdot D_m^2}{F_m \cdot D_p^2} = \frac{\gamma_p \cdot H_p}{\gamma_m \cdot H_m} \tag{A5}$$

Stress due to centrifugal force of water

$$\frac{\sigma_p}{\sigma_m} = \frac{H_p}{H_m} \tag{A6}$$

(5) Frequency of Oscillating Stress

$$\frac{f_p}{f_m} = \frac{n_p}{n_m} = \frac{1}{N}\sqrt{\frac{H_p}{H_m}} \tag{A7}$$

97

Appendix B: Theory of Modal Analysis

Assuming free vibration and non-damped structure, the force equation may be expressed as:

$$[M]\{\ddot{u}\} + [K]\{u\} = \{0\} \tag{B1}$$

where $[M]$ = *mass matrix*

$\quad\quad [K]$ = *stiffness matrix*

$\quad\quad \{\ddot{u}\}$ = *acceleration vector*

$\quad\quad \{u\}$ = *displacement vector*

For a linear system, free vibrations will be harmonic in nature. Thus, the displacement vector can be written as:

$$\{u\} = \{\Phi\}_i \cos(\omega_i \cdot t) \tag{B2}$$

where $\{\Phi\}_i$ = *eigenvector representing the mode shape of the ith natural frequency*

$\quad\quad \omega_i$ = *the ith natural frequency (radian per unit time)*

$\quad\quad t$ = *time*

Substituting into equation (B1), we get

$$\left(-\omega_i^2 [M] + [K]\right)\{\Phi\}_i = \{0\} \tag{B3}$$

For non-trivial solution, the determinant of $([K] - \omega^2 [M])$ is zero. Thus,

$$\left| [K] - \omega^2 [M] \right| = 0 \tag{B4}$$

This is a typical eigenvalue problem with n values of ω^2 and n eigenvectors $\{\Phi\}$ that can satisfy equation (B4) where n is the total number of DOF for the structure. ANSYS provides a number of eigenvalue extraction methods. Details are discussed in the following.

Eigenvalue and Eigenvector Extraction Method

ANSYS provides two different types of procedures: (1) full extraction from reduced matrix, and (2) partial extraction from full matrix. Since no presumption can be made on the vibration behavior of the runner, it is not easy to reduce the matrix before performing the analysis. Focus is placed, therefore, on the second type of procedure.

There are 4 types of extraction methods available: (1) subspace iteration, (2) block Lanczos, (3) unsymmetric eigensolver, and (4) damped eigensolver. Since the turbine runner does not have unsymmetric matrix, the unsymmetric eigensolver would be omitted. On the other hand, damping of the turbine runner would be mainly cause by water acted as added mass on the turbine. Thus, damped eigensolver is not appropriate for eigenvalue extraction. Damping using added mass effect would be discussed in a separate section 2.3.

Subspace Iteration Method

The subspace iteration method is an effective method widely used for eigenvalue extraction and is described in detail by Bathe [11, pp.954-978]. Some reasons of its popularity are that the theory is relatively easy to understand and the method is easy to

program. The procedure is particularly suited for the calculation of a few eigenvalues and eigenvectors of a large finite element system.

The solution procedure[10] was named the subspace iteration method because the iteration is equivalent to iterating with a q-dimensional subspace. A total of 6 hours CPU time was required for extracting 25 modes from the turbine FE model using the described PC system.

Block Lanczos Eigenvalue Extraction Method

The block Lanczos eigenvalue extraction method is available for large symmetric eigenvalue problems. The eigensolver used in ANSYS is based on theory found by Grimes et al [12]. This new variation of algorithm performs recursive operation using a block of vectors as opposed to the classical method that only uses one single vector. This solver has a higher convergence rate compared to the subspace iteration method. Extracting same number of modes from the same model using the block Lanczos method required only 1.5 hours (Compared to 6 hours for subspace iteration method). Since subspace and block Lanczos method extract exactly the same natural frequencies and mode shapes, block Lanczos method was used for the analysis of this work.

---

[10] The solution procedure consists of the following three steps:

1.   Establish q starting iteration vectors, q > p, where p is the number of eigenvalues and vectors to be calculated.
2.   Use simultaneous inverse iteration o the q vectors and Ritz analysis to extract the "best" eigenvalue and eigenvector approximations from the q iteration vectors.
3.   After iteration convergence, use the Sturm sequence check to verify that the required eigenvalues and corresponding eigenvectors have been calculated.

Appendix C: Derivation of Surface Panel Method for Added Mass Effect (Reference [16])

Notation

[A] = Diagonal matrix of panel areas	g = Acceleration due to gravity
[C] = Damping matrix	G = Green's function
{F_f} = Fluid force vector	n = Normal
{F_s} = Structural and body force vector	p = Pressure
[H] = Coefficient matrix relating source strength to velocity potential	t = time
[K] = Structural stiffness matrix	z = Height of free surface
[L] = Coefficient matrix relating source strength to normal velocity at panel control points	Γ = Structural surface boundary
[M] = Structural mass matrix	{u} = Nodal displacement Vector
[M_A] = Added fluid mass matrix	ρ = fluid density
[T] = Transformation matrix for normal to global direction	σ = Source strength (assumed constant on a panel)
{V_n} = Vector of control point normal velocities	ϕ = Velocity potential function

A structural dynamic response analysis by finite element method requires solution of the structural equilibrium equations in the form:

$$[M]\ddot{u} + [C]\dot{u} + [K]u = F_f(t) + F_s(t) \tag{C1}$$

To obtain the fluid forces on the structure, the relationship between the fluid pressure field and the interface accelerations must be defined. Using potential flow theory:

$$\phi \to 0 \quad \text{as} \quad x \to \infty \tag{C2}$$

$$\left.\frac{\partial \phi}{\partial n}\right|_\Gamma = \frac{du}{dt} \tag{C3}$$

where Γ is the fluid/structure interface and the substantive derivative is used on the right hand side of (C3). Linearized free surface boundary condition if a free surface present:

$$\frac{d^2\phi}{dt^2} + g\frac{\partial \phi}{\partial z} = 0 \tag{C4}$$

To solve the potential function using surface panel method, f is defined by a distribution of singularities of constant strength on panels on the interface surface. In case of using a simple source distribution, the field potential at x=(x,y,z) is written in the form:

$$\phi(x) = \int G(x,x')\sigma(x')d\Gamma(x') \tag{C5}$$

where x' represents the coordinate vector of a point on the panel surface and σ is the source strength. In discrete form (C5) becomes:

$$\phi(x) = \sum_{j=1}^{NP} \sigma_j \int_j G(x,x_j')d\Gamma(x_j') \tag{C6}$$

Where the constant panel source strength has been removed from the panel integral. The kernel function G in the current formulation is the free space Green's function for a source of strength of 4π.

$$G(x, x_j') = \frac{1}{r} = \frac{1}{|x - x_j'|} \tag{C7}$$

The gradient of the velocity potential function is then forced to satisfy the boundary condition of (C3) at a number of control points on the body. The gradient is given by

$$\frac{\partial \phi(x)}{\partial n} = \sum_{j=1}^{NP} \sigma(j) \int_j \frac{\partial G(x, x_j')}{\partial n} d\Gamma(x_j') \tag{C8}$$

The integrals in equation (C6) and (C8) can be evaluated exactly, and these analytical solution are used when the panel-to-control point separation is relatively small. For a particular set of control points, the evaluation of the integrals in equation (C6) and (C8) leads to the system

$$\{\phi\} = [H]\{\sigma\} \tag{C9}$$

$$\{V_n\} = [L]\{\sigma\} \tag{C10}$$

with [H] a coefficient matrix relating source strength to control point potential and [L] a coefficient matrix relating source strength to control point fluid normal velocities. Relation (C9) and (C10) define completely the fluid flow field given the distribution of source strengths σ.

The fluid velocities normal to the panels at the control points can be related via equation (C3) to the local nodal point velocities in the finite element model.

$$\{V_n\} = [T]\frac{d\{u\}}{dt} \tag{C11}$$

Rearranging (C10) and (C11), the panel source strength becomes

$$\{\sigma\} = [L]^{-1}[T]\frac{d\{u\}}{dt} \tag{C12}$$

Substituting equation (C12) into (C9), the velocity potential at a control point is

$$\{\phi\} = [H][L]^{-1}[T]\frac{d\{u\}}{dt} \tag{C13}$$

In case of using dipoles of constant strength on a panel, the integral equation is

$$\int G(x, x')\frac{\partial \phi(x')}{\partial n} d\Gamma(x') = \int \phi(x')\frac{\partial G(x, x')}{\partial n} d\Gamma(x') \tag{C14}$$

Similar to the derivation in source formulation:

$$[H]\{V_n\} = [L]\{\phi\} \tag{C15}$$

Solving for the control point potential and substituting for the surface velocity:

$$\{\phi\} = [L]^{-1}[H][T]\frac{d\{u\}}{dt} \tag{C16}$$

The pressure field in the fluid of density ρ can be determined from the velocity potential via the Bernoulli equation

$$p = -\rho\frac{d\phi}{dt} \tag{C17}$$

Using equation (C13), therefore:

$$\{p\} = -\rho[H][L]^{-1}[T]\frac{d^2\{u\}}{dt^2} \tag{C18}$$

By introducing the panel area matrix [A] and transform the local coordinates to the global coordinate via [T] and [T]^T, the fluid force vector can be expressed as

$$\{F_f\} = -\rho[T]^T[A][H][L]^{-1}[T]\frac{d^2\{u\}}{dt^2}$$

(C19)

By neglecting rigid body motion and surface displacement derivatives and nonlinear terms from time derivatives, equation (C19) reduces to

$$\{F_f\} = -[M_A]\{\ddot{u}\}$$

(C20)

Therefore added mass matrix by source formulation is

$$[M_A] = \rho[T]^T[A][H][L]^{-1}[T]$$
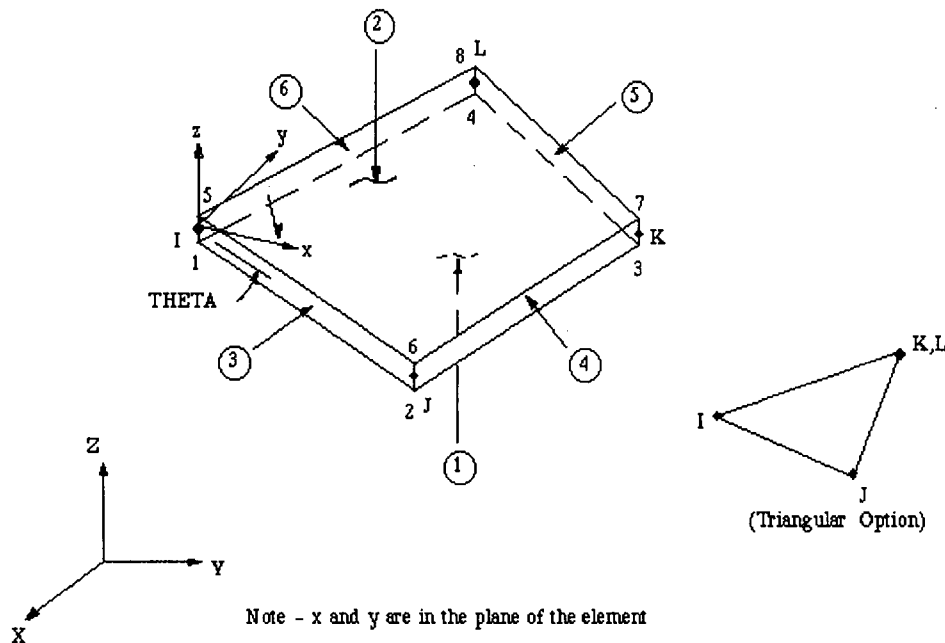
(C21)

Added mass matrix by dipole formulation is

$$[M_A] = -\rho[T]^T[A][L]^{-1}[H][T]$$

(C22)

The modified structural equilibrium equation is

$$[M + M_A]\{\ddot{u}\} + [C]\{\dot{u}\} + [K]\{u\} = \{F_s(t)\}$$

(C23)

Appendix D: Summary of Element Properties

Shell Element

Note - x and y are in the plane of the element

(Triangular Option)

Elastic Shell Element Assumptions and Restrictions

Zero area elements are not allowed. This occurs most often whenever the elements are not numbered properly. Zero thickness elements or elements tapering down to a zero thickness at any corner are not allowed. The applied transverse thermal gradient is assumed to vary linearly through the thickness and vary bilinearly over the shell surface.

An assemblage of flat shell elements can produce a good approximation to a curved shell surface provided that each flat element does not extend over more than a 15 degrees arc. If an elastic foundation stiffness is input, one-fourth of the total is applied at each node. Shear deflection is not included in this thin-shell element.

A triangular element may be formed by defining duplicate K and L node numbers. The extra shapes are automatically deleted for triangular elements so that the membrane stiffness reduces to a constant strain formulation. For large deflection analyses, the element must be triangular.

The four nodes defining the element should lie in an exact flat plane; however, a small out-of-plane tolerance is permitted so that the element may have a slighty warped shape. A moderately warped element will produce a warning message in the printout. If the warpage is too severe, a fatal message results and a triangular element should be used. If the lumped mass matrix formulation is specified, the effect of the implied offsets on the mass matrix is ignored for warped elements.

Plastic Shell Element Assumptions and Restrictions

Zero area elements are not allowed. This occurs most often whenever the elements are not numbered properly. Zero thickness elements or elements tapering down to a zero thickness at any corner are not allowed. Under bending loads and tapered elements produce inferior stress results and refined meshes may be required. Use of this element in triangular form produces results of inferior quality compared to the quadrilateral form. However, under thermal loads, when the element is doubly curved (warped), triangular elastic shell element produce more accurate stress result than do quadrilateral shaped element. Quadrilateral elastic shell elements may produce inaccurate stresses under thermal loads for doubly curved or warped domains. The applied transverse thermal gradient is assumed to vary linearly through the thickness. The out-of-plane (normal) stress for this element varies linearly through the thickness. The transverse shear stresses are assumed to be constant through the thickness.

Shear deflections are included. Elastic rectangular elements without membrane loads give constant curvature results, i.e., node stresses are the same as the centroidal stresses. For linearly varying results use elastic shell elements. Triangular elements are not geometrically invariant and the element produces a constant curvature solution. Only the lumped mass matrix is available.
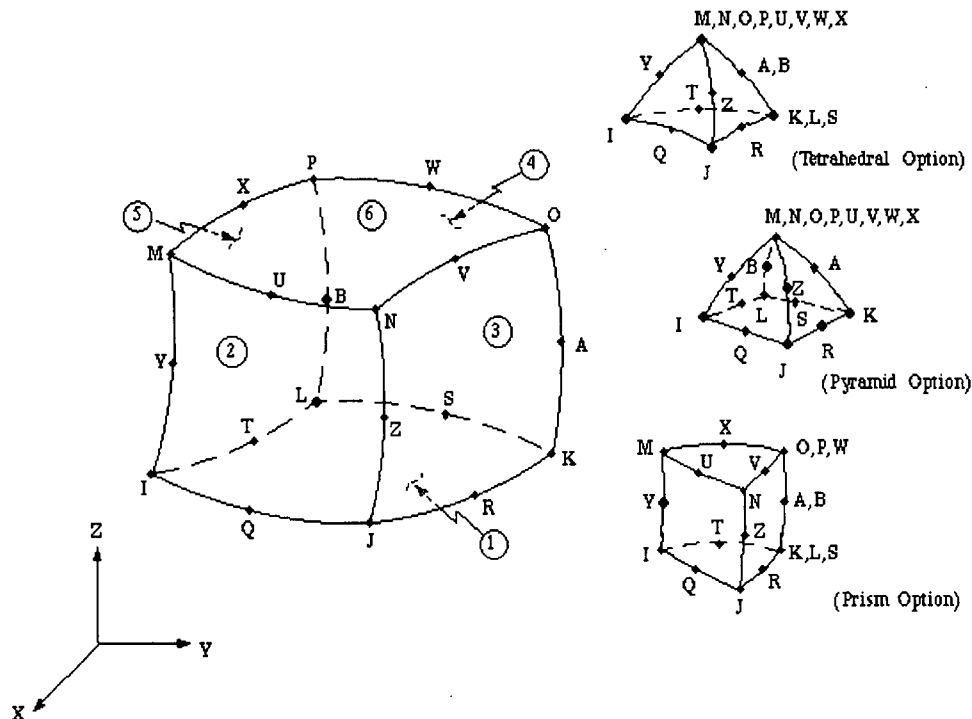
3D 20-Node Solid Element Assumptions and Restrictions

The element must not have a zero volume. Also, the element may not be twisted such that the element has two separate volumes. This occurs most frequently when the element is not numbered properly. An edge with removed midside node implies that the displacement varies linearly, rather than parabolically, along that edge.

Degeneration to the form of pyramid should be used with caution. The element sizes, when degenerated, should be small in order to minimize the stress gradients. Pyramid elements are best used as filler elements or in meshing transition zones.

104

Appendix E: Computation of Initiation Life in MathCAD.

BC Hydro and Power Authority
GMS Turbine Cracking Investigation
Fatigue Initiation Life Prediction
Strain Life Approach
Date: April 14, 1999
By Brian Sze Bun Chan
Assuming ASTM A27 similar to AISI 1020 properties

$ksi := 10^3 \cdot psi$

$E := 27000 \cdot ksi$

$\sigma_f := 123.2 \cdot ksi$

$b := -0.12$

$\varepsilon_f := 0.44$

$c := -0.51$

Loading Condition: 95% Static + 5% Harmonic Response Analysis

$\varepsilon_{max} := 0.13244 \cdot 10^{-2}$

$\varepsilon_{min} := 0.12224 \cdot 10^{-3}$

$\Delta\varepsilon := \varepsilon_{max} - \varepsilon_{min}$

$N_f := 10000$

Given

$$\frac{\Delta\varepsilon}{2} = \varepsilon_f \cdot \left(2 \cdot N_f\right)^c + \frac{\sigma_f}{E} \cdot \left(2 \cdot N_f\right)^b$$

$N_f := Find\left(N_f\right)$

$N_f = 2.362 \cdot 10^7$

$Days := \dfrac{N_f}{(60 \cdot 3600 \cdot 24)}$

$Days = 4.556$

$Years := \dfrac{Days}{365.25}$

$Years = 0.012$

Loading Condition: 97.5% Static + 2.5% Harmonic Response Analysis

$\varepsilon_{max} := 0.11338 \cdot 10^{-2}$

$\varepsilon_{min} := 0.48242 \cdot 10^{-3}$

$\Delta\varepsilon := \varepsilon_{max} - \varepsilon_{min}$

$N_f := 10000$

Given

$$\frac{\Delta\varepsilon}{2} = \varepsilon_f \left(2 \cdot N_f\right)^c + \frac{\sigma_f}{E} \cdot \left(2 \cdot N_f\right)^b$$

$N_f := Find\left(N_f\right)$

$N_f = 2.062 \cdot 10^9$

$$Days := \frac{N_f}{\left(60 \cdot 3600 \cdot 24\right)}$$

$Days = 397.681$

$$Years := \frac{Days}{365.25}$$

$Years = 1.089$